Politechnika Krakowska

Cracow University of Technology

NUMERICAL ANALYSIS OF STRAIN LOCALIZATION IN ONE- AND TWO-PHASE GEOMATERIALS

Anna Stankiewicz

Cracow, April 2007

I would like to express my thanks to my supervisor Prof. Jerzy Pamin for formulating the basis of my research, constant assistance and guidance.
I also acknowledge the constructive help and illuminating explanations of Prof. Andrzej Truty.
I am grateful to Prof. Maria Radwańska for useful suggestions during the edition of the thesis.
Finally, I wish to thank my colleagues for their support and kindness.

Contents

Chapter 1

Introduction

The material softening and the non-symmetry of the tangent stiffness operator are possible sources of material (e.g. soil) instability and strain localization. The numerical simulation of these phenomena in porous materials is the subject of this thesis.

The issue of material instabilities causing strain localization has been investigated for example in the review papers [15, 41, 81], in the extensive study of bifurcations in geomaterials [79] and in the proceedings of IUTAM symposium [16]. If a material instability [26, 37] is encountered in the deformation history of a body, the strains often localize in a number of narrow bands, while the remaining parts of the body unload. Within a classical continuum formulation and for static problems this phenomenon is associated with the loss of ellipticity of the governing partial differential equations. Therefore, discretization methods used to solve the equations may yield mesh-sensitive and hence questionable results. To overcome this problem, a form of rate-dependent or non-local enhancement of the constitutive model should be adopted [15, 65]. The non-locality may have the form of micropolarity (e.g. [40]), integral averaging (e.g. [4]) or spatial gradient-dependence (e.g. [77]). All these approaches imply the introduction of an internal length parameter in the continuum description. In certain cases, for instance for the simulation of discrete fissures in rocks, discontinuum modelling can also be an option.

This thesis is focused on instabilities in porous materials which are often modelled as two-phase media composed of solid and fluid. The solid-fluid interaction influences the critical load level for which an instability can occur as well as the direction and width of the localized deformation bands. In particular, the permeability coefficient and the pore fluid compressibility are found to affect localization cf. for instance [3, 31, 59]. However, it is unclear whether the onset of instability in a two-phase medium coincides with that in the underlying drained solid. In this thesis the influence of fluid phase on soil instabilities is investigated using the local and gradient-enhanced modified Cam-clay model [58].

In [3] an investigation of the plane-strain instability of saturated porous media is performed. It is concluded that the elastic-plastic models can exhibit two-phase instability despite the fact that the solid phase remains in the stable regime. The contractant hardening materials are found to be more inclined to two-phase instability than dilatant ones. In [31], the problem of strain localization in porous materials is thoroughly discussed. The author confirms that the localized solution is possible when the acoustic tensor associated with the underlying drained material becomes singular. It is concluded that soil under undrained conditions requires stronger softening than drained soil in order to reach a state in which localization is possible. In [59] the conditions for the onset of shear localization in the limiting cases of drained and undrained state for dilatant and contractant geomaterials are discussed. It is stated that for dilatant soil the condition for localization is met earlier for drained than undrained response. On the contrary, in case of the contractant soil the conditions for localization are fulfilled for undrained state before drained.

Moreover, in [62] it is claimed that the two-phase modelling of soil involves a certain regularization by introducing a gradient term via the Darcy's law, although the necessity of regularization of the constitutive model for a multiphase material is usually recognized. In [88] a gradient plasticity model is used to analyze dynamic instabilities in fully and partially saturated granular material. The influence of permeability on the width of localization zone in a one-dimensional test is also evaluated. In [42] a gradient-enhanced visco-plastic model is applied to localization analysis of clays. In [5] it is shown that the length scale introduced by incorporating the fluid flow depends on the integration time step and is thus insufficient for the regularization of unstable behaviour.

More recent developments concerning the problem of numerical simulations of localized deformation bands in multiphase (granular) media are covered for instance in [7, 11, 34, 44, 89]. In [7] the problem of deformation and strain localization in partially saturated porous medium is considered and a constitutive model (extension of the modified Cam-clay model) for such a three-phase medium is proposed. In [44] a general variational framework of Cam-clay theory is constructed within the finite deformation plasticity. In [89] the issue of internal length scale introduced by the fluid-solid interaction is considered in a dynamic context. The dynamic aspects of the analysis of the two-phase saturated soil under dynamic load can also be found in [84] and other works of these Authors.

In [89], using stability and dispersion analyses the limit wave numbers are evaluated, for which the internal length parameter vanishes and hence regularization is mandatory. These results are confirmed in [11]. On the other hand, in [34] arguments are given to support the opinion that, at least for saturated sand undergoing dilatation, the fluid phase stabilizes the soil and regularizes the solution.

1.1 Research objectives

The general objective of this thesis is the numerical analysis of instabilities and strain (and pore pressure) localization in one-phase and fluid-saturated porous materials.

The realization of the goal requires the reliable modelling of geomaterials considering their basic features as multiphase materials. The soil skeleton behaviour is described using the modified Cam-clay model originally proposed in [58] and commonly accepted as reliable for cohesive soils.

In order to preserve the well-posedness of the governing partial differential equations in the presence of material instabilities, the Cam-clay model is enhanced by introducing suitable higher-order deformation gradients in an enhanced continuum description. In particular, the degree of overconsolidation is made dependent on the Laplacian of a hardening/softening parameter, or, more precisely of the plastic multiplier. The enhancement introduces an internal length parameter and prevents the mesh-sensitivity of discretized numerical solutions. The effectiveness of this gradient regularization of the modified Cam-clay model is studied.

Particular attention is focused on the analysis of the influence of fluid phase represented by (excess) pore pressure on soil behaviour. The influence of soil permeability on the stabilizing role of fluid phase is investigated.

The implementation and consistent linearization of the local Cam-clay model follows [22] and the gradient-enhancement of the theory is based on concepts developed in [12, 13, 39]. The numerical material model and the algorithms were incorporated into the FEAP finite element package [70] in the following steps. At first the local version of Cam-clay model for one-phase medium was implemented. The classical one-field element with discretization of displacements was used at this stage. This formulation allows for the analysis of two extreme stages: drained state (excess pore pressure equal to zero) or undrained state (fluid motion prevented). The second step is a description of soil as a two-phase medium. A two-field finite element in which the displacements and the excess pore pressure are discretized is considered. In order to prevent the mesh-sensitivity of numerical results the gradient enhancement of Cam-clay model is incorporated. A two-field element with the discretization of displacements and plastic multiplier is programmed at this stage. The final step is an implementation of gradient-dependent Cam-clay model for the two-phase medium. This formulation requires a three-field element in which displacements, excess pore pressure and plastic multiplier are discretized.

The thesis of the dissertation is the statement that in the two-phase soil description based on the Cam-clay model, the presence of the second phase does not guarantee regularization. It is necessary to enhance the constitutive model, for example by introducing suitable higher-order (inelastic) deformation gradients in the continuum description.

1.2 Assumptions and limitations

Inertial effects and large deformations or strains are left out of the scope of the thesis, but both static deformation and consolidation problems are considered. The attention is thus limited to elliptic or elliptic-parabolic problems with linear kinematics. The equilibrium and kinematic equations have the form (Voigt's matrix-vector notation is used):

$$\boldsymbol{L}^{\mathrm{T}}\boldsymbol{\sigma}_t + \rho\boldsymbol{g} = \boldsymbol{0}, \tag{1.1}$$

$$\boldsymbol{\epsilon} = \boldsymbol{L}\boldsymbol{u}, \tag{1.2}$$

where $\boldsymbol{L}$ is a differential operator matrix, $\boldsymbol{\sigma}_t$ is the total stress tensor in a vector form, ρ is the density, $\boldsymbol{g}$ is the gravitation vector, $\boldsymbol{\epsilon}$ is the strain tensor in a vector form, $\boldsymbol{u}$ is the displacement vector and superscript T is the transpose symbol. The stresses and displacements satisfy the relevant natural and essential boundary conditions.

The derived formulations are three-dimensional, the implementation is limited to two-dimensional plane strain and axisymmetric configurations. The attention is focused on the physical and numerical aspects in the sense of aiming at mesh-insensitive results with a clear physical explanation. However, the aim is not to analyze the efficiency of different (in particular stabilized, cf. [73]) finite elements or develop adaptive remeshing techniques, undoubtedly advisable for the analyzed class of problems.

The Terzaghi's concept of effective stress is adopted in order to represent the dominant role of solid skeleton in load-carrying capacity of soil. The governing equations for partially saturated soil are derived in Sect. 5.1, but the implementation is limited to the case of fully saturated soil.

1.3 Contents

The thesis is organized as follows. The remaining part of chapter 1 includes the stress and strain notation. The volumetric-deviatoric decomposition of the mentioned tensors is presented. A list of matrices, vectors, scalars and functions used in this thesis is enclosed.

In chapter 2 the problem of numerical modelling of granular materials is discussed. Essential physical properties of soils are described including their multiphase nature. The Terzaghi's assumption of effective stresses is presented. The role of total and effective stress is explained. An overview of plasticity models used for the mechanical analysis of geomaterials is included.

Chapter 3 deals with the problem of material instability and localization phenomena in granular materials. Instability indicators for one-phase medium are discussed. However, the attention is focused on the influence of fluid phase on the material behaviour. The literature on the subject is reviewed.

The modified Cam-clay model in its local version is described in chapter 4. The nonlinear stress-strain relations are presented. The cases of associated and non-associated plasticity are considered. The finite element implementation of the material model is summarized. The one-element tests showing the typical soil behaviour and localization tests which exhibit mesh sensitivity are enclosed.

Chapter 5 presents the equations for two-phase modelling of fully and partially saturated soil and the special cases of undrained and drained state, in which one-phase modelling is possible. It also contains the description of the formulated and implemented finite element models, including their linearization and discretization. The results for one-element tests and benchmark results showing the strain and pore pressure localization for two-phase medium are also presented.

The gradient-enhancement of the Cam-clay model is reported on in chapter 6. The algorithm for the gradient-dependent Cam-clay plasticity and discretization-independent results of numerical simulations are included. The influence of imperfections on the numerical results is examined.

Chapter 7 contains the description of the formulated three-field finite element, including its linearization and discretization. The results of numerical simulations are also discussed.

Selected applications of the developed numerical models are included in chapter 8.

Final remarks are gathered in chapter 9.

1.4 Volumetric-deviatoric decomposition

Due to the granular and multiphase nature of soils we have to distinguish between the total and effective stress (cf. Sect. 2.2 for the explanation). The constitutive equations are written in terms of the effective stress tensor. Its matrix representation reads:

$$\boldsymbol{\sigma} = \begin{pmatrix} \sigma_{xx} & \sigma_{xy} & \sigma_{xz} \\ \sigma_{yx} & \sigma_{yy} & \sigma_{yz} \\ \sigma_{zx} & \sigma_{zy} & \sigma_{zz} \end{pmatrix} \tag{1.3}$$

or using Voigt's matrix-vector notation $\boldsymbol{\sigma} = [\sigma_{xx}, \sigma_{yy}, \sigma_{zz}, \sigma_{xy}, \sigma_{yz}, \sigma_{zx}]^{\mathrm{T}}$.
In a similar way we can write the matrix representation of strain tensor:

$$\boldsymbol{\epsilon} = \begin{pmatrix} \epsilon_{xx} & \epsilon_{xy} & \epsilon_{xz} \\ \epsilon_{xy} & \epsilon_{yy} & \epsilon_{yz} \\ \epsilon_{xz} & \epsilon_{yz} & \epsilon_{zz} \end{pmatrix} \tag{1.4}$$

which in a vector form using the engineering shear strain components is written as: $\boldsymbol{\epsilon} = [\epsilon_{xx}, \epsilon_{yy}, \epsilon_{zz}, 2\epsilon_{xy}, 2\epsilon_{yz}, 2\epsilon_{zx}]^{\mathrm{T}}$. This vector representation will be used in this thesis.

The usual solid mechanics sign convention is such that tension is assumed to be possitive (both stress and strain). On the other hand, in nearly all aspects of soil mechanics only compressive stresses are present thus it is very frequent to use the convention of compression being positive. Eventually, in this thesis, the adopted sign convention is that the compressive stresses and strains are negative, however, the compressive pressure is regarded as positive.

The formulation of many plasticity models requires the volumetric-deviatoric split of stress and strain tensors. The stress tensor $\boldsymbol{\sigma}$ in Voigt's notation can be decomposed into:

$$\boldsymbol{\sigma} = \boldsymbol{\xi} - \boldsymbol{\Pi}\, p = \boldsymbol{\xi} + \frac{1}{3}\boldsymbol{\Pi}\boldsymbol{\Pi}^{\mathrm{T}}\boldsymbol{\sigma}, \tag{1.5}$$

in which $\boldsymbol{\xi}$ is the deviatoric stress, $\boldsymbol{\Pi} = [1, 1, 1, 0, 0, 0]^{\mathrm{T}}$ and p is the pressure. The deviatoric stress vector $\boldsymbol{\xi}$ is defined as:

$$\boldsymbol{\xi} = \boldsymbol{Q}\boldsymbol{\sigma}, \tag{1.6}$$

matrix $\boldsymbol{Q}$ is given by:

$$\boldsymbol{Q} = \boldsymbol{I} - \frac{1}{3}\boldsymbol{\Pi}\boldsymbol{\Pi}^{\mathrm{T}} \tag{1.7}$$

$$\boldsymbol{Q} = \begin{bmatrix} \boldsymbol{Q}_n & \boldsymbol{0} \\ \boldsymbol{0} & \boldsymbol{Q}_t \end{bmatrix}, \quad \boldsymbol{Q}_n = \begin{bmatrix} \frac{2}{3} & \frac{-1}{3} & \frac{-1}{3} \\ \frac{-1}{3} & \frac{2}{3} & \frac{-1}{3} \\ \frac{-1}{3} & \frac{-1}{3} & \frac{2}{3} \end{bmatrix}, \quad \boldsymbol{Q}_t = \mathrm{diag}[1, 1, 1]. \tag{1.8}$$

Note that $\boldsymbol{I}$ is the identity matrix.
The hydrostatic pressure which is the invariant of the stress tensor is given by:

$$p = -\frac{1}{3}(\sigma_{xx} + \sigma_{yy} + \sigma_{zz}) = -\frac{1}{3}I_1^{\boldsymbol{\sigma}} = -\frac{1}{3}\boldsymbol{\Pi}^{\mathrm{T}}\boldsymbol{\sigma} = -\frac{1}{3}\mathrm{tr}(\boldsymbol{\sigma}) \tag{1.9}$$

The equivalent deviatoric stress is defined as:

$$q = \sqrt{3J_2} = \sqrt{\frac{3}{2}\boldsymbol{\xi}^T \boldsymbol{R}\boldsymbol{\xi}}. \tag{1.10}$$

In a similar way the strain tensor $\boldsymbol{\epsilon}$ in vector form can be decomposed into:

$$\boldsymbol{\epsilon} = \boldsymbol{\gamma} + \boldsymbol{\Pi}\,\theta \tag{1.11}$$

where the deviatoric strain vector $\boldsymbol{\gamma}$ is given by:

$$\boldsymbol{\gamma} = \frac{1}{3}\boldsymbol{Q}\boldsymbol{\epsilon}. \tag{1.12}$$

and the volumetric strain (the invariant of strain tensor) is called dilatation and computed as:

$$\theta = \epsilon_{xx} + \epsilon_{yy} + \epsilon_{zz}, \tag{1.13}$$

1.5 Notation

Here is the list of symbols and abbreviations most frequently used in the thesis:

Tensors, matrices, vectors:

$\boldsymbol{\gamma}$ deviatoric strain vector

$\boldsymbol{D}$ tangent stiffness tensor

$\boldsymbol{\epsilon}$ strain tensor in a vector form

$\boldsymbol{g}$ gravitation vector

$\boldsymbol{k}$ permeability matrix

$\boldsymbol{L}$ differential operator matrix

$\boldsymbol{m}$ vector normal to a plastic potential

$\boldsymbol{n}$ vector normal to the yield surface

$\boldsymbol{r}$ vector of residuals

$\boldsymbol{s}$ vector of primary unknowns

$\boldsymbol{\sigma}$ effective stress tensor in a vector form

$\boldsymbol{\sigma}_t$ total stress tensor in a vector form

$\boldsymbol{u}$ displacement vector

$\boldsymbol{v}_d$ Darcy's fluid flow velocity

$\boldsymbol{\xi}$ deviatoric stress vector

$\boldsymbol{Q}$ acoustic tensor

Scalars:

c cohesion

e void ratio

F yield function

g gradient scaling factor

G plastic potential

$\bar{G}$ secant shear modulus

h hardening/softening modulus

θ volumetric strain

θ^{e} elastic part of volumetric strain

θ^{p} plastic part of volumetric strain

K_t tangential bulk modulus

$\bar{K}$ secant bulk modulus

κ swelling index

λ compression index

Λ plastic multiplier

M, $\bar{M}$ material constants

n porosity

ν Poisson's ratio

p effective pressure acting on the soil skeleton

p_c preconsolidation pressure

p_f excess pore pressure

q equivalent deviatoric stress

ρ density

$\hat{\rho}$ saturated density of the soil-fluid mixture

ρ_s density of the solid phase

ρ_f density of the fluid phase

S saturation ratio

V material volume

V_p pore volume

V_s skeleton volume

φ friction angle

ψ dilatation angle

Chapter 2

Numerical modelling of granular materials

In Fig. 2.1 the multiphase, porous and granular nature of soil is depicted. In general, three phases can be distinguished i.e. solid skeleton with pores filled with fluid and gas phase. This complex microstructure determines the soil features and causes instabilities observed at macroscopic scale.

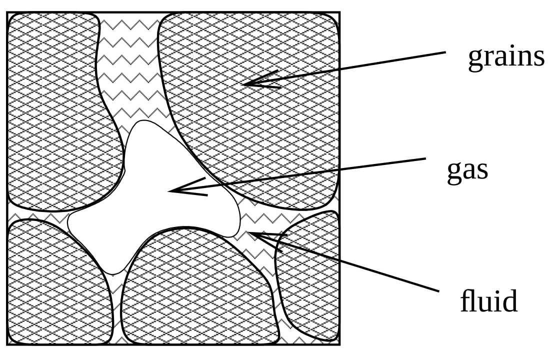

Figure 2.1: Soil as a multiphase, porous and granular medium

2.1 Soil features

One of the fundamental soil features is its sensitivity to density/volume changes, which can be caused either by a change in effective confining pressure p or by a rearrangment of grains in the structure due to shearing load. Typical for soil is the tendency to reach a critical state, in which only the deviatoric plastic strain increments are observed and the strength and volume are constant.

Let us consider the two soil idealizations presented in Fig. 2.2. If a shear load is applied, the solid particles slide and roll. In case of a loose soil sample the pore volume will decrease during shearing (contraction) involving material hardening. On the other hand, if a dense configuration is loaded in shear the pore volume increases (dilatation) and material softening is observed, cf. results in Sect. 4.6.3. Similar results, strongly dependent on the soil density, can be obtained for a triaxial test, cf. Sect. 4.6.2. A loose specimen exhibits contractation (hardening behaviour), while a dense one densifies at first and then dilates (material softening). The conclusion is that the density/volume changes determine the soil behaviour.

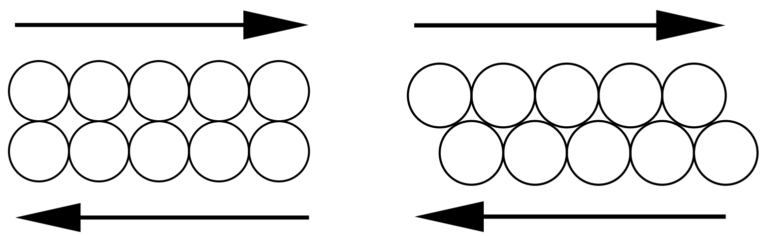

Figure 2.2: Soil grains in loose (left) and dense (right) configuration. Contractant and dilatant behaviour, after [25].

2.2 Effective and total stress

To represent the multiphase nature of soil in phenomenological modelling the concept of effective stress is introduced. All forces acting on the soil mass are balanced by the total stress tensor $\boldsymbol{\sigma}_t$. However, the total stress decomposes into the effective stress in solid skeleton and the pressures in fluid constituents. This decomposition is necessary to reproduce the dominant role of solid part in the load-carrying capacity of soil. It is known that the incorporation of pore fluid in the analysis considerably reduces the material strength. Particularly, all shear stresses are supported by the solid grains since pore water and/or air can carry no shear stress at all. For a fully saturated soil (solid grains and pores completely filled with water) this decomposition is ilustrated in Figs 2.3-2.4.

The effective pressure acting on the soil skeleton is defined by:

$$p = -\frac{1}{3}\mathrm{tr}(\boldsymbol{\sigma}_t) - p_f, \tag{2.1}$$

where p_f is the excess pore pressure. The effective stress tensor $\boldsymbol{\sigma}$ for the porous medium is related to the total stress tensor by:

$$\boldsymbol{\sigma} = \boldsymbol{\sigma_t} + \boldsymbol{\Pi} p_f, \tag{2.2}$$

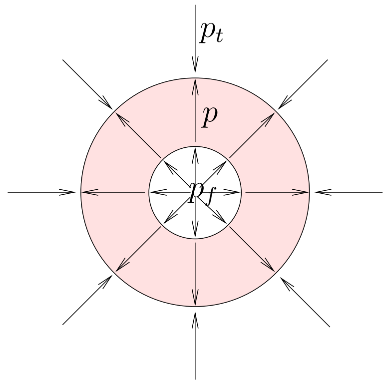

Figure 2.3: Effective stress

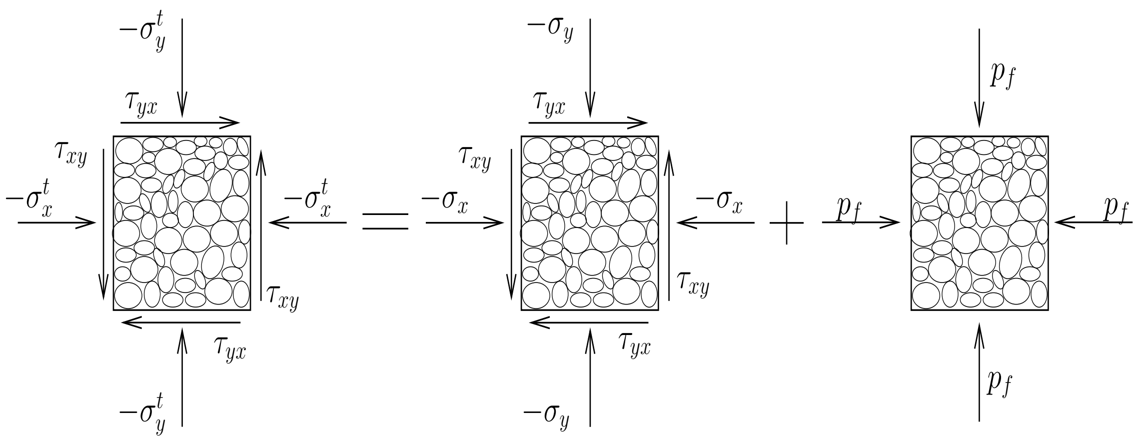

Figure 2.4: Effective stress, based on [72]

where $\mathbf{\Pi} = [1, 1, 1, 0, 0, 0]^T$. The above relations are known as the effective stress principle and were given by Terzaghi. In case of partially saturated soil (solid skeleton and voids partly occupied by water and partly by air) the extended Bishop's effective stress concept is used in the form:

$$\boldsymbol{\sigma} = \boldsymbol{\sigma_t} + \mathbf{\Pi} S p_f, \tag{2.3}$$

where S - saturation ratio.

To summarize, the effective stress is responsible for the deformation and limit states of saturated soil (it is used in constitutive equations). The balance of the medium is maintained by the total stress (it stands in momentum balance equations).

2.3 Plasticity models for geomaterials

The elastic or plastic behaviour of the material depends on the stress level. The yield condition for perfect plasticity is in general written as $F(\boldsymbol{\sigma}) = 0$. The set of stress states that satisfy this condition (plastic stress states) forms the yield surface bounding all possible stress states. The stresses within the yield surface corresponds to elastic stress states. Stresses outside the yield surface are not allowed (impossible).

Differently shaped yield surfaces have been proposed by different researchers for different materials. In ductile materials such as metals, the onset of yielding does not depend on the volumetric part of the stress. On the contrary, frictional materials such as sands, soil, rocks or concrete are called pressure-sensitive due to the essential effect of the first invariant $I_1^{\boldsymbol{\sigma}}$ on the yield condition and inelastic behaviour. Thus, according to experimental observations, constitutive relations for geomaterials are either dilatant or contractant.

An overview of plasticity models used for the mechanical analysis of geomaterials can be found for instance in [24,33,90]. The modern computational aspects of the plasticity models are covered among others in [9,25,73]. Next to the plasticity models described in this section also hypoplastic models are very popular (cf. [71]). Here, we first summarize the Mohr-Coulomb and Burzyński-Drucker-Prager (BDP) theory (cf. [91] for the explanation of the name), commonly used, but suitable for a rather simplified analysis of frictional materials. The idea of closed yield surface is briefly described (cf. [17,29]). Then we extensively cover the modified Cam-clay model which properly represents the physical properties of a large class of geomaterials.

2.3.1 Mohr-Coulomb plasticity

The Mohr-Coulomb yield criterion is represented by:

$$F(\boldsymbol{\sigma}) = \frac{1}{2}(\sigma_3 - \sigma_1) + \frac{1}{2}(\sigma_3 - \sigma_1)\sin\varphi - c\cos\varphi, \tag{2.4}$$

where σ_3 and σ_1 are the largest and smallest principal stresses, respectively ($\sigma_3 > \sigma_1$), φ is a friction angle and c is cohesion. The above equation is valid as long as $\sigma_1 < \sigma_2 < \sigma_3$. If this is not the case, we can obtain the other five yield conditions by cyclic permutation (cf. [10, 32]). The Mohr-Coulomb yield function is represented in the three-dimensional principal stress space as a hexagonal pyramid, shown in Fig. 2.5. The model representation in the Π-plane (perpendicular to $\sigma_1 = \sigma_2 = \sigma_3$ axis) is shown in Fig. 2.6. The model can be used to describe with reasonable accuracy the behaviour of sand, drained clays, rocks and concrete.

2.3.2 Burzyński-Drucker-Prager plasticity

The classical Burzyński-Drucker-Prager (BDP) yield function can be written as follows:

$$F(\boldsymbol{\sigma}) = q + \alpha p - \beta c\ , \tag{2.5}$$

where $q = \sqrt{3J_2}$ and J_2 is the second invariant of the deviatoric stress tensor, p is the hydrostatic pressure, the coefficients α and β are functions of the internal friction angle φ:

$$\alpha = \frac{6\sin\varphi}{3-\sin\varphi}\ , \quad \beta = \frac{6\cos\varphi}{3-\sin\varphi}\ , \tag{2.6}$$

c is a measure for the cohesion. For a non-associated flow rule, the plastic potential G is defined as:

$$G = q + \overline{\alpha} p\ , \tag{2.7}$$

where $\overline{\alpha}$ is a function of the dilatation angle ψ, similar to the definition of α in eq. (2.6):

$$\overline{\alpha} = \frac{6\sin\psi}{3-\sin\psi}\ . \tag{2.8}$$

When ploted in the three-dimensional principal stress space, the Drucker-Prager yield function when ploted in the three-dimensional is a cone, the axis of which coincides with the hydrostatic axis, cf. Fig. 2.5. The model representation in the Π-plane is shown in Fig. 2.6. For $\sin\varphi = \sin\psi = 0$ the special case of Huber-Mises-Hencky (HMH) yield function which is a cylinder with radius $\sigma_y = 2c$ is obtained. The yield function for the HMH plasticity reads:

$$F(\boldsymbol{\sigma}) = q - \sigma_y \tag{2.9}$$

For isotropic hardening, the eq. 2.5 has to be rewritten in the form:

$$F(\boldsymbol{\sigma}, \varepsilon^{\mathrm{p}}) = q + \alpha p - \beta c(\varepsilon^{\mathrm{p}})\ , \tag{2.10}$$

where ε^{p} is an invariant plastic strain measure (hardening parameter). For linear hardening/softening we have $c = c_{\mathrm{y}} + h_{\mathrm{c}}\varepsilon^{\mathrm{p}}$ with constant modulus h_{c}.

In the case of gradient-dependent Drucker-Prager plasticity [46, 66], the yield function is additionally dependent on the Laplacian of the plastic strain measure ε^{p}. Assuming that only the cohesion exhibits the gradient dependence, the yield function takes the form:

$$F(\boldsymbol{\sigma}, \varepsilon^{\mathrm{p}}, \nabla^2\varepsilon^{\mathrm{p}}) = q + \alpha p - \beta c(\kappa, \nabla^2\varepsilon^{\mathrm{p}})\ , \tag{2.11}$$

and the plastic potential function does not change.

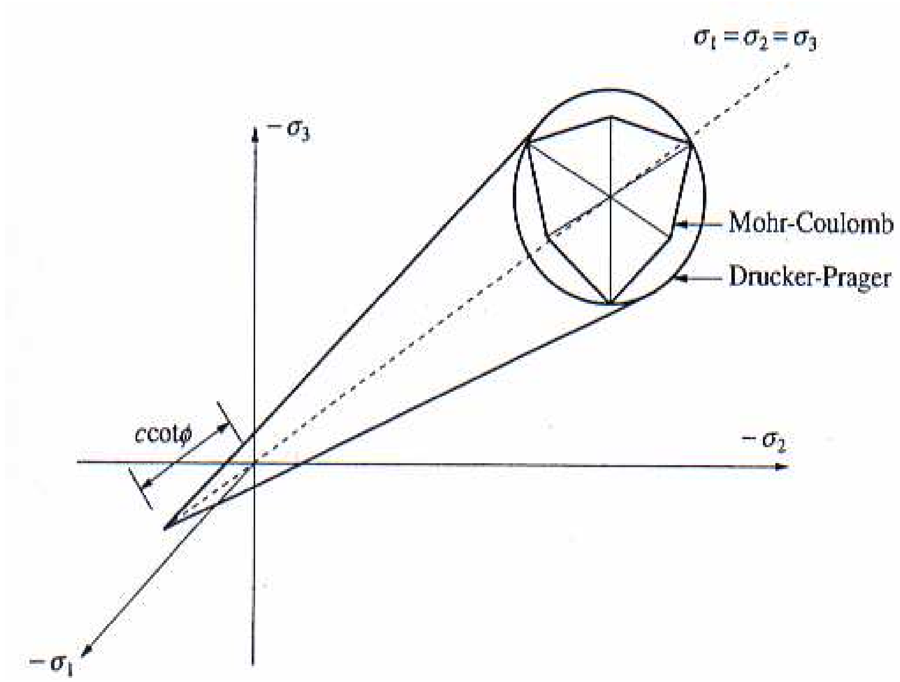

Figure 2.5: Representation of the Mohr-Coulomb and Drucker-Prager yield criteria in the three-dimensional principal stress space

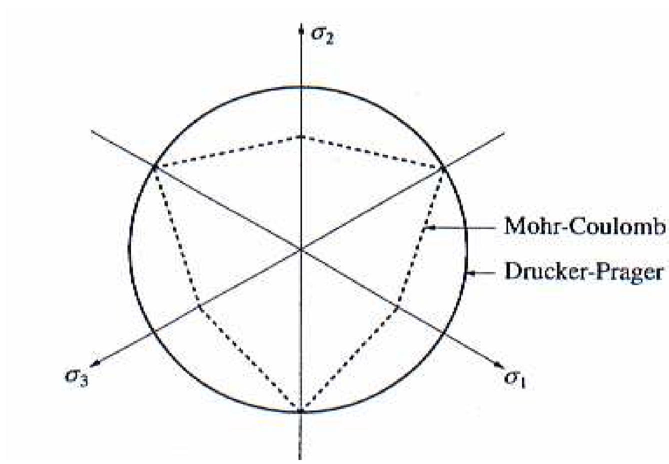

Figure 2.6: Representation of the Mohr-Coulomb and Drucker-Prager yield surfaces in the Π-plane

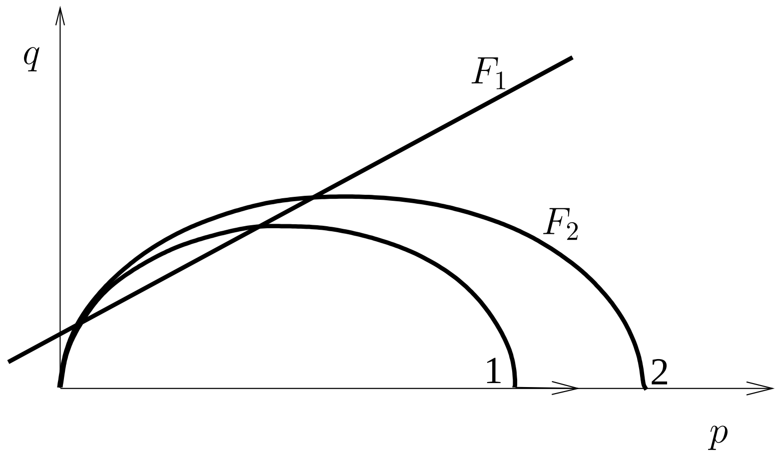

Figure 2.7: Open and closed yield surface, after [90]

2.3.3 Closed yield surfaces

The classical elastoplastic models for soils like Mohr-Coulomb or Burzyński-Drucker-Prager can only be used for a specific range of problems due to their severe limitations. When for example the Mohr-Coulomb or Burzyński-Drucker-Prager yield surface is used in the case of strong hydrostatic compression, no plastic deformation is produced since these yield criteria are open on the compressive side along the hydrostatic axis. In such a case, closed yield criteria must be used [90]. This fact is illustrated in Fig. 2.7. When the equivalent deviatoric stress $q = 0$, the stress path coincides with the hydrostatic axis and both states 1 and 2 are located inside the yield surface f_1, thus, no plastic strain is produced. To overcome the problem, the yield surface intersecting the hydrostatic axis and also expanding from point 1 to 2 (hardening due to densification) should be used.

Therefore, majority of modern plasticity models for soils are based on critical state soil mechanics framework, developed by the group of researchers from the University of Cambridge [58]. The ideas of volumetric hardening and closed yield surface are applied in this framework. The main assumptions of the critical state theory can be found for example in [20, 90].

Chapter 3

Instabilities and strain localization

The strain localization can turn up in various materials. It is observed when the whole deformation of the material sample concentrates in one or more narrow bands. The sources of localization phenomena lies at the meso- or micro-level of observation (e.g. heterogeneity or local material defects).

The problem of material instabilities inducing loss of ellipticity and strain localization will now be recapitulated following [66].

We now recapitulate the problem of material instabilities inducing loss of ellipticity and strain localization. A broader discussion of the issues is presented in [15, 41, 65, 81], in the study of bifurcations in geomaterials [79], and in the more general theoretical considerations gathered in [53, 54]. Then, we review some literature on the influence of the second phase on the phenomena will be reviewed, cf. [3, 31, 35, 62, 87].

3.1 Instability indicators for one-phase medium

According to the definition of material stability [37, 38, 82] a material is stable if its constitutive relationship satisfies the condition of positive second order work density:

$$\dot{\epsilon}_{ij}\dot{\sigma}_{ij} > 0\,, \tag{3.1}$$

where $\dot{\epsilon}_{ij}$ and $\dot{\sigma}_{ij}$ are the strain and stress rate tensors, respectively, and the summation convention is adopted. Our consideration is limited to incrementally linear constitutive equations:

$$\dot{\sigma}_{ij} = D_{ijkl}\dot{\epsilon}_{kl}\,. \tag{3.2}$$

A material instability is indicated by the loss of positive-definiteness of the tangent stiffness tensor D_{ijkl}, i.e. by the singularity of the symmetric part of D_{ijkl}:

$$\det(D_{ijkl} + D_{klij}) = 0\,. \tag{3.3}$$

It was shown in [82] that the smallest eigenvalue of D_{ijkl} is larger than or equal to the smallest eigenvalue of its symmetric part. Therefore, for a non-symmetric tangent stiffness tensor the loss of material stability may occur in the deformation history prior to the limit point and loss of uniqueness related to a diffuse bifurcation, cf. [15, 81], which are marked by the condition:

$$\det(D_{ijkl}) = 0\,. \tag{3.4}$$

Limiting interest to elasto-plasticity, the classical tangent stiffness operator can be obtained as:

$$D_{ijkl} = D^{\mathrm{e}}_{ijkl} - \frac{D^{\mathrm{e}}_{ijmn} m_{mn} n_{pq} D^{\mathrm{e}}_{pqkl}}{h + n_{mn} D_{mnpq} m_{pq}}\,, \tag{3.5}$$

where $\boldsymbol{D}^{\mathrm{e}}$ is the elastic stiffness operator, h is the hardening/softening modulus, $\boldsymbol{m}$ is the plastic flow direction vector (normal to a plastic potential) and $\boldsymbol{n}$ is the vector normal to the yield surface. As shown in [82], the special structure of the elastic-plastic tangent operator $\boldsymbol{D}^{\mathrm{ep}}$ in eq. (3.5) implies that it has only real eigenvalues even if it is non-symmetric, so that condition (3.4) is satisfied only when $h = 0$. This means that if one assumes $h > 0$, the diffuse bifurcation cannot occur.

However, when the material stability is lost due to softening or nonsymmetry of the tangent operator, a so-called discontinuous bifurcation is possible, cf. [15, 43, 45, 57, 60, 82]. For a homogeneous and homogeneously deformed body we investigate the possibility that upon a further increment of deformation a discontinuity of the deformation gradient across a plane with normal ν_i is admitted:

$$[\![\, u_{i,j} \,]\!] \equiv u^{+}_{i,j} - u^{-}_{i,j} \neq 0, \tag{3.6}$$

where $[\![\quad]\!]$ denotes a jump of a quantity while the '+' and '-' signs refer to the two sides of the discontinuity plane (Fig. 3.1). During this bifurcation the continuity of displacements and the equilibrium condition are preserved at each point. If the deformation satisfies the kinematic compatibility equations, it is piecewise homogeneous, so that, for an arbitrary vector μ_i, the strain jump can be written as:

$$[\![\, \epsilon_{ij} \,]\!] = \frac{1}{2}(\nu_i \mu_j + \nu_j \mu_i)\,. \tag{3.7}$$

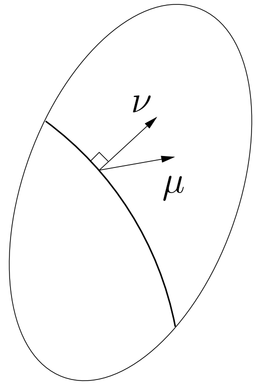

Figure 3.1: Material instability: discontinuity plane, after [48]

With the piecewise linear constitutive equation (3.2) we obtain the stress rate jump at the onset of the discontinuity:

$$[\![\dot{\sigma}_{ij}]\!] = D_{ijkl}[\![\dot{\epsilon}_{kl}]\!] \,, \tag{3.8}$$

where it is assumed that according to the concept of a linear comparison solid [26], the same tangent stiffness moduli represent the material behaviour on both sides of the discontinuity plane. Equilibrium requires that during the formation of the discontinuity the tractions t_j are continuous across the plane with normal ν_i:

$$[\![\dot{t}_j]\!] = \nu_i[\![\dot{\sigma}_{ij}]\!] = 0, \tag{3.9}$$

so substituting eq. (3.8) and the rate form of eq. (3.7) into eq. 3.9, and exploiting the symmetry property $D_{ijkl} = D_{ijlk}$ we obtain the following equation:

$$(\nu_i D_{ijkl} \nu_l)\mu_k = 0, \tag{3.10}$$

which has a non-trivial solution only when the determinant of the so-called acoustic tensor $Q_{jk} = \nu_i D_{ijkl} \nu_l$ is zero:

$$\det(Q_{jk}) = 0. \tag{3.11}$$

For a given tangent stiffness the last condition produces a vector ν_l, which defines the discontinuity direction. The vector μ_k can then be determined from eq. (3.10) and the jump mode $\nu_l \mu_k$ is known. For a shear band vector ν_l is perpendicular to μ_k.

The singularity of the acoustic tensor and the formation of the strain discontinuity correspond to the local loss of ellipticity of the rate equilibrium equations. The ellipticity is one of the necessary conditions for well-posedness of the rate boundary value problem (BVP), cf. references in [15]. Well-posedness is understood as the existence of a finite number of linearly independent and continuous solutions, of the continuum BVP.

The emergence of the discontinuities in the deformation gradient has been identified with strain localization since paper [60] was published. A shear band may be viewed as a zone of intense deformation bounded by two discontinuity planes. However, since the distance between those two planes remains undefined for a classical material model, they coincide giving localization in a set of measure zero. In this thesis the notion of strain localization is understood in a broader sense, as the emergence of bands of concentrated deformation due to material instabilities. Nevertheless, the first point in the deformation history for which there exists a nontrivial solution of eq. (3.10) marks the possible onset of localization.

Substituting the elasto-plastic stiffness matrix from eq. (3.5) into the definition of the acoustic tensor and analyzing eq. (3.11) it is possible to find the critical values of the hardening modulus h, for which ellipticity is lost, and the direction vector $\boldsymbol{\nu}$ normal to the discontinuity plane [45, 60]. The critical value of h, which may be positive for non-associated plasticity, and the direction $\boldsymbol{\nu}$ depend on the stress state as well as on the form of the yield and plastic potential functions. In numerical analysis of discrete systems condition (3.11) can be used to detect the loss of ellipticity and potential localization at an integration point level.

This type of analytical examination of the acoustic tensor is performed in [30, 66, 80]. The analysis determines the normalized value of the determinant of the acoustic tensor as a function of an angle defining the direction of the discontinuity plane in a two-dimensional case. It proves that the degree of non-associativeness measured by the difference between the friction coefficient $\sin\varphi$ and the dilatation coefficient $\sin\psi$ is the crucial instability factor.

It is noted that, in addition to the above analyzed so-called weak discontinuities, jumps in the displacement field itself (*strong* discontinuities) can be considered, cf. for instance [83]. They correspond to a displacement discontinuity (crack) along plane interfaces, while in the continuous parts of the body material stability and ellipticity are preserved. Since the softening behaviour is then concentrated in the interfaces, the BVP for the discontinuum remains well-posed.

However, in this work we look for solutions within the continuum mechanics description and propose to enhance the formulation with a form of nonlocal averaging, which regularizes the BVP in presence of material instabilities, cf. Fig. 3.2. In particular the family of gradient-dependent models is pursued. As shown in [46, 81], the occurrence of the discontinuity plane is then only possible for a very special structure of the constitutive operator. Usually ellipticity is guaranteed and localization in a set of measure zero is prevented.

Nevertheless, for the gradient dependent continuum the critical value of the hardening modulus and the direction of the localization band can be determined from the classical

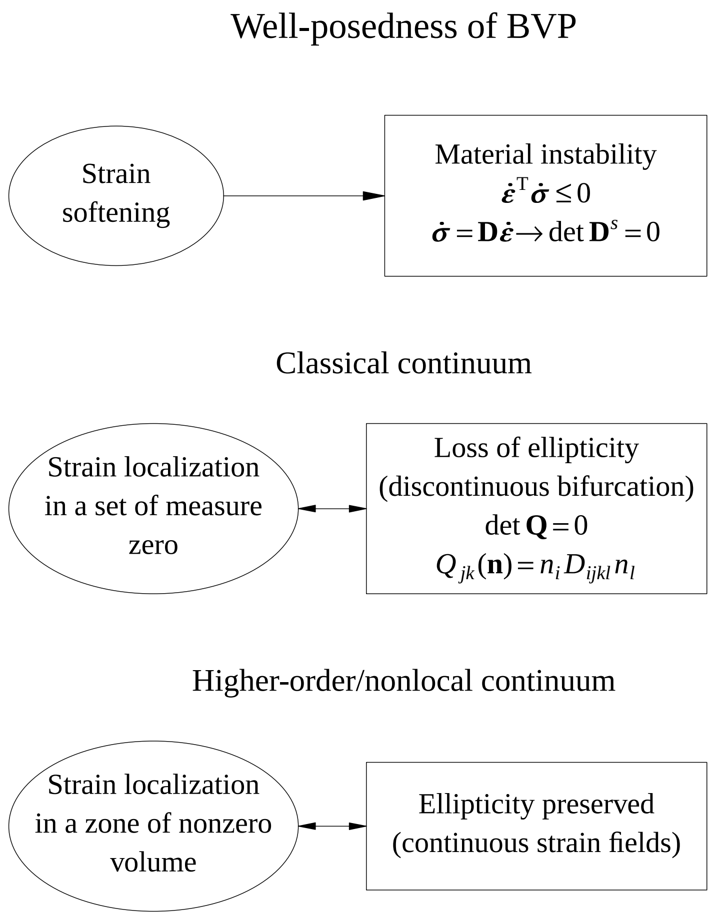

Figure 3.2: Illustration of ill-posedness problem and remedy, after [47]

condition of the acoustic tensor singularity (3.11) if prior to the moment of bifurcation into a localized deformation pattern the gradient terms have no influence on the solution.

3.2 Influence of fluid phase

In [35] the issue of instabilities in saturated two-phase materials is discussed in the dynamic context, i.e. acceleration wave speeds in a rate-independent elastic-plastic porous materials with ideal fluid phase are considered. The loss of hyperbolicity and well-posedness is related to the emergence of zero or conjugate complex wave speeds associated with a stationary discontinuity (standing localization wave) or flutter instability, respectively. The model is based on the theory of mixtures. The major conclusion is that the critical hardening modulus for which a stationary discontinuity is possible is equal to the modulus for the underlying drained solid. However, it is also shown that the flutter phenomenon can occur immediately upon the onset of plastic loading if plasticity is non-associative and both phases are assumed

to be incompressible. For compressible constituents this can also happen, while this type of instability is usually excluded for solid skeletons. Special cases of a BDP elastic-plastic solid and plastically contractant skeletons is considered.
The special case of undrained solid was analyzed in the dynamic stability context in [76] and chapter 11 of [79], leading to the conclusion that contractant materials become unstable at the critical state of maximum shear while for the dilatant materials instabilities occur in the softening regime of the underlying drained skeleton.

It was pointed out in [36] that the presence of the pore fluid can delay localization in viscoplasticity. This line of reasoning is examined in the set of papers of Schrefler and co-workers [61–63, 87, 88]. They discuss both theoretically and numerically the influence of the coupling of the equilibrium (or motion) equation to the mass continuity equation for the fluid phase. Within the context of dynamic analysis of partially saturated medium they focus on the phenomenon of cavitation caused by negative pore pressures and on the ability of the Laplacian present in the continuity equation to regularize the localization problem. The Laplacian which enters the formulation from the Darcy's law is scaled by the permeability coefficient. The regularization effect is related to an internal length parameter, derived to depend on what the authors call intrinsic permeability, on the fluid saturation, density, elastic modulus and wave number. For large permeability mesh sensitivity is still observed and for small permeability the estimated internal length parameter is very large resulting in distributed failure. It is also shown that the inclination of shear bands depends on the permeability and boundary conditions for the pore pressure field. The derivation of the internal length parameter based on permeability holds for a certain wave number domain and is impossible for a shear wave propagation problem. Therefore, like in this study, the authors also considered a Laplacian term in the yield condition [88].

An investigation of the plane-strain instability of saturated porous media is performed in [3]. It is concluded that the elastoplastic models can exhibit two-phase instability despite the fact that the solid phase remains stable. The contractant hardening materials are found to be more inclined to two-phase instability than dilatant ones. The two-phase instability, caused by solid-fluid interaction, may be delayed by the fluid compressibility.

The problem of strain localization in porous materials is also discussed in [31]. The author confirms that the localized solution is possible when the acoustic tensor associated with the underlying drained material becomes singular (the singularity of the undrained acoustic tensor then involves an unbounded discontinuity). Larsson presents an opinion that fully drained conditions have a major influence on the occurrence of the localization. It is concluded that soil under undrained conditions requires stronger softening than drained soil in order to reach a state where localization is possible. The influence of material parameters on the localization phenomena is also investigated. The permeability coefficient and the pore fluid compressibility is found to affect the localization phenomenon. In some cases the fluid can have a regularization effect.

The authors of the recent publications seem to agree that the incorporation of the fluid flow (via Darcy's velocity) introduces an internal length scale in the description but it is dependent on the integration time step and thus insufficient to regularize the problem. Such a conclusion and its explanation can be found for example in [5, 11].

3.3 Laplacian-dependent plasticity

Now, we revisit the gradient plasticity formulation [12, 39] in which the yield function which depends on the Laplacian of a hardening parameter ε^{p} is written as:

$$F(\boldsymbol{\sigma}, \varepsilon^{\mathrm{p}}, \nabla^2 \varepsilon^{\mathrm{p}}) = 0. \tag{3.12}$$

The yield function satisfies the Kuhn-Tucker conditions:

$$\dot{\Lambda} \geq 0\,, \;\; F \leq 0\,, \;\; \dot{\Lambda} F = 0, \tag{3.13}$$

in which Λ is the plastic multiplier. The gradient-dependence of the yield function implies that the plastic consistency condition $\dot{F} = 0$ is the following partial differential equation:

$$\frac{\partial F}{\partial \boldsymbol{\sigma}} \dot{\boldsymbol{\sigma}} + \frac{\partial F}{\partial \varepsilon^{\mathrm{p}}} \dot{\varepsilon}^{\mathrm{p}} + \frac{\partial F}{\partial \nabla^2 \varepsilon^{\mathrm{p}}} \nabla^2 \dot{\varepsilon}^{\mathrm{p}} = 0\;. \tag{3.14}$$

The plastic consistency condition (3.14) requires that

$$\dot{F} = \boldsymbol{n}^{\mathrm{T}} \dot{\boldsymbol{\sigma}} - h \dot{\Lambda} + g \nabla^2 \dot{\Lambda} = 0\;, \tag{3.15}$$

where $\boldsymbol{n}$ and h are given by:

$$\boldsymbol{n}^{\mathrm{T}} = \frac{\partial F}{\partial \boldsymbol{\sigma}}\,, \quad h = -\frac{\dot{\varepsilon}^{\mathrm{p}}}{\dot{\Lambda}} \frac{\partial F}{\partial \varepsilon^{\mathrm{p}}}\;. \tag{3.16}$$

and

$$g = \frac{\dot{\varepsilon}^{\mathrm{p}}}{\dot{\Lambda}} \frac{\partial F}{\partial \nabla^2 \varepsilon^{\mathrm{p}}} \tag{3.17}$$

is a positive gradient influence factor with the dimension of force. For $g = 0$ the classical plastic flow theory is retrieved, but for $g \neq 0$ the plastic multiplier is a solution of the partial differential equation (3.15). In order to compute $\dot{\Lambda}$ this differential equation should be solved.

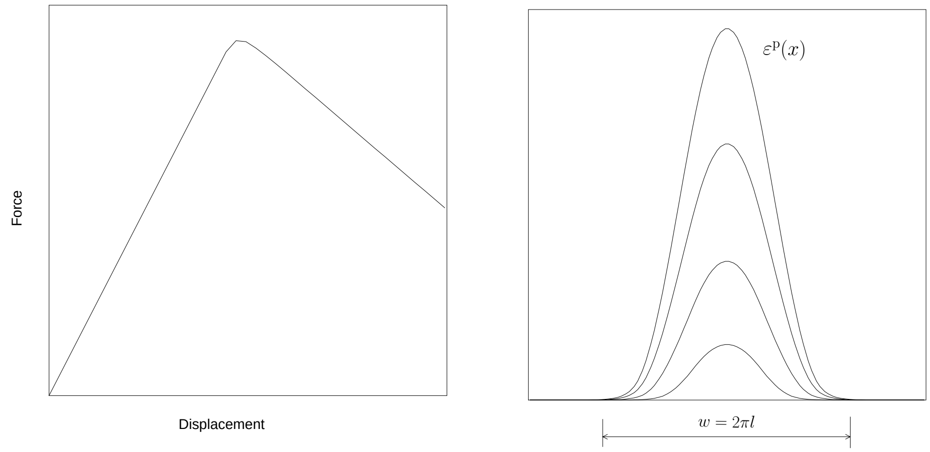

Figure 3.3: Typical evolution of the plastic strain distribution when softening results in localization [47]

As will be shown in Sect. 6.3, in the employed algorithm the yield condition (3.12) is written in a weak form, the plastic multiplier field is discretized and this additional integral equation is solved in parallel with the equilibrium problem. The coupled boundary value problem, its linearization and discretization are given in Sect. 6.3, cf. also [12, 13].

In the majority of papers on the subject the Laplacian-dependent yield function has the form

$$F = \tilde{\sigma}(\boldsymbol{\sigma}) - \sigma_{\mathrm{y}}(\varepsilon^{\mathrm{p}}) + g\nabla^2\varepsilon^{\mathrm{p}} = 0, \tag{3.18}$$

where $\tilde{\sigma}$ is an equivalent stress measure, σ_{y} is the yield strength (usually isotropic hardening/softening is assumed) and g is assumed to be constant, although it can be made dependent for instance on the equivalent plastic strain ε^{p} [46].

For instance, in the case of gradient-dependent BDP plasticity [66], assuming that only the cohesion exhibits the gradient dependence, the yield function takes the form:

$$F(\boldsymbol{\sigma}, \varepsilon^{\mathrm{p}}, \nabla^2\varepsilon^{\mathrm{p}}) = q + \alpha p - \beta c(\varepsilon^{\mathrm{p}}, \nabla^2\varepsilon^{\mathrm{p}}) \ , \tag{3.19}$$

and the plastic potential function remains as given in eq. (2.7).

It is emphasized that the gradient terms disappear from the constitutive equations if a homogeneous state of strain and stress is analyzed. The gradient terms are negligible if strains vary slowly in space (in the pre-peak regime of softening problems), but have a significant influence in the presence of strain localization (in the post-peak regime).

The enhancement of the classical theory has been made in order to preserve well-posedness of the governing equations for materials which do not comply with the material stability requirement [15, 37, 82], i.e. when a softening relation between stresses and strains is assumed

$h < 0$ or when non-associative plastic flow is postulated to reproduce experimental response of soil, making the tangent operator $\boldsymbol{D}^{\mathrm{ep}}$ nonsymmetric. For a softening medium the factor g can be associated with an internal length parameter l, e.g. in a one-dimensional analytical solution we have $g = -hl^2 > 0$ [12]. However, also for a hardening material the Laplacian term with $g > 0$ smoothes the solution [13].

It is illustrative to observe a typical evolution of the plastic strain in a one-dimensional localization problem or along a cross-section of the localization band in a two-dimensional problem. In Fig. 3.3 we can observe that the plastic zone has a constant width, which is estimated analytically by $w = 2\pi l$ [12].

Chapter 4

Modified Cam-clay model

The considered formulation is a combination of nonlinear elasticity and plasticity with a modified Cam-clay yield condition and is based on [22]. The modified Cam-clay model belongs to critical state models [20] and describes the behaviour of the soil skeleton. The constitutive equations are written in terms of the effective stress tensor. This elastic-plastic model is capable of reproducing the essential physical properties of soils, including hardening/softening and contraction/dilatation.

In the three-dimensional principal stress space the modified Cam-clay yield function is represented by an ellipsoidal surface, see Fig. 4.1, further on. In the $p - q$ plane it is an ellipse, symmetric about the hydrostatic axis, see Fig. 4.2.

The dependence of the yield condition on the third invariant of the stress tensor (Lode angle) is not incorporated in the description. On the other hand, the non-associativity of the plastic flow is taken into account. The elliptic shape of the yield function can be distorted to

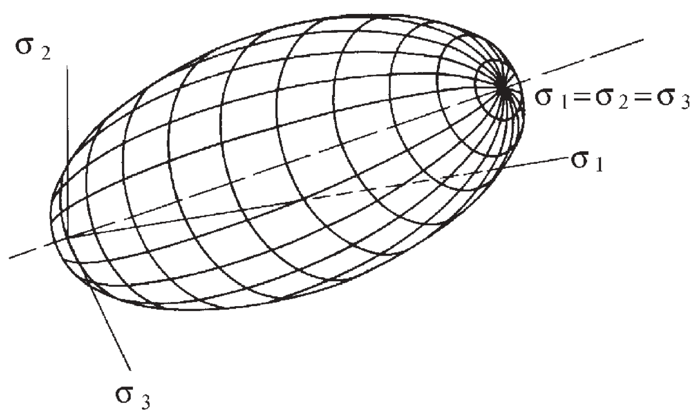

Figure 4.1: Ellipsoidal yield surface of the modified Cam-clay model

approximate better the experimental results [23, 28], although this is not done in the present work.

4.1 Nonlinear elasticity

In general, the elastic behaviour of soils is nonlinear. The pressure – volumetric elastic strain relation can be written as follows:

$$\mathrm{d}p = -K_t \, \mathrm{d}\theta^{\mathrm{e}}, \tag{4.1}$$

with tangential bulk modulus growing with increasing pressure:

$$K_t(p, e) = \frac{1+e}{\kappa} p, \tag{4.2}$$

where e - void ratio, κ - positive parameter called swelling index.
Substituting eq. (4.2) into eq. (4.1) we obtain:

$$\frac{\mathrm{d}p}{p} = -\frac{1+e}{\kappa} \, \mathrm{d}\theta^{\mathrm{e}}. \tag{4.3}$$

After integration over a finite increment we obtain the effective hydrostatic pressure as an expotential function of volumetric strain increment:

$$p(\Delta\theta^{\mathrm{e}}) = p_0 \exp\left[-\frac{1+e_0}{\kappa}\Delta\theta^{\mathrm{e}}\right]. \tag{4.4}$$

The subscript ’0’ indicates the values at the reference state, e.g. at the beginning of a loading step and Δ the difference between the value of a quantity at the current state and at the reference state. The secant bulk modulus $\bar{K}$ for the increment can be computed from eq. (4.1) as:

$$\bar{K} = \frac{p_0\left(1 - \exp\left[-\frac{1+e_0}{\kappa}\Delta\theta^{\mathrm{e}}\right]\right)}{\Delta\theta^{\mathrm{e}}} \tag{4.5}$$

or, when $\Delta\theta^{\mathrm{e}} \to 0$, it is given by:

$$\bar{K} = \frac{1+e_0}{\kappa} p_0. \tag{4.6}$$

The void ratio e is defined by the following relation between the pore volume V_p, skeleton volume V_s and material volume V:

$$e = \frac{V_p}{V_s} = \frac{V - V_s}{V_s} = \frac{V}{V_s} - 1. \tag{4.7}$$

It is assumed that the void ratio changes slowly and can be updated only once at the end of a loading step according to:

$$e(\Delta\theta) = (1 + e_0)\exp[\Delta\theta] - 1. \tag{4.8}$$

The nonlinear elasticity is described in terms of volumetric components. Assuming isotropy and constant Poisson's ratio ν we can calculate the secant shear modulus $\bar{G}$ as:

$$\bar{G} = \frac{3}{2}\frac{1-2\nu}{1+\nu}\bar{K} \tag{4.9}$$

and the deviatoric stress is updated according to:

$$\boldsymbol{\xi} = \xi_0 + 2\bar{G}\boldsymbol{R}^{-1}\Delta\boldsymbol{\gamma}^{\mathrm{e}}, \tag{4.10}$$

where $\boldsymbol{R} =$ diag$[1, 1, 1, 2, 2, 2]$. Further, the tangential operator is computed as:

$$\frac{\mathrm{d}\boldsymbol{\sigma}}{\mathrm{d}\boldsymbol{\epsilon}} = \frac{\mathrm{d}\boldsymbol{\xi}}{\mathrm{d}\boldsymbol{\epsilon}} - \boldsymbol{\Pi}\frac{\mathrm{d}p}{\mathrm{d}\boldsymbol{\epsilon}} \tag{4.11}$$

and eventually we obtain:

$$\frac{\mathrm{d}\boldsymbol{\sigma}}{\mathrm{d}\boldsymbol{\epsilon}} = 2\bar{G}\boldsymbol{Q}\boldsymbol{R}^{-1} + 2\frac{\partial\bar{G}}{\partial\Delta\theta^{\mathrm{e}}}\boldsymbol{R}^{-1}\Delta\boldsymbol{\gamma}\boldsymbol{\Pi}^T + K_t\boldsymbol{\Pi}\boldsymbol{\Pi}^T, \tag{4.12}$$

with:

$$\frac{\partial\bar{G}}{\partial\Delta\theta^{\mathrm{e}}} = \frac{3}{2}\frac{1-2\nu}{1+\nu}\left[\frac{K_t}{\Delta\theta^{\mathrm{e}}} + \frac{p-p_0}{\Delta\theta^{\mathrm{e}2}}\right] \tag{4.13}$$

or, for $\Delta\theta^{\mathrm{e}} \to 0$:

$$\frac{\partial\bar{G}}{\partial\Delta\theta^{\mathrm{e}}} = -\frac{3}{4}\frac{1-2\nu}{1+\nu}\left(\frac{1+e_0}{\kappa}\right)^2 p_0. \tag{4.14}$$

4.2 Associated plasticity

The modified Cam-clay yield function is written in terms of the second invariant of the deviatoric stress tensor, the internal friction angle, the current hydrostatic pressure, and a measure for the current degree of overconsolidation, which is a function of the plastic volumetric strain adopted as the hardening/softening parameter. The elliptic yield function (Fig. 4.2) can be written as:

$$F = q^2 + M^2 p(p - p_c) = 0, \tag{4.15}$$

where the equivalent deviatoric stress is defined in eq. 1.10. The shape of the ellipse is determined by a material constant M and does not change during hardening or softening. M is a function of friction angle ϕ and defines the inclination of the critical state line (CSL):

$$M = \frac{6\sin\phi}{3-\sin\phi}. \tag{4.16}$$

The yield surface intersects the hydrostatic axis at the origin and at the point $(p_c, 0)$. The preconsolidation pressure i.e. the largeest effective pressure the soil has ever experienced in its history is denoted by p_c. The evolution of the preconsolidation pressure p_c is related to the volumetric part of the plastic strain and given by a formula similar to eq. (4.4):

$$p_c = p_{c0} \exp(-\frac{1+e_0}{\lambda - \kappa} \Delta\theta^{\mathrm{p}}), \tag{4.17}$$

where λ is a hardening modulus which defines the inclination of the virgin consolidation line in the $(1+e)$ versus $\ln p$ diagram in Fig. 4.3, and θ^{p} denotes the plastic dilatation.
Since the fraction $\frac{1+e_0}{\lambda-\kappa}$ is positive the signs of $\dot{p_c}$ and $\dot{\theta^p}$ must be opposite. This means that the hardening (contraction) is observed for decreasing increment of plastic volumetric strain ($\dot{\theta^p} < 0 \Longrightarrow \dot{p_c} > 0$). The material exhibit softening (dilatation) for increasing increment of plastic volumetric strain ($\dot{\theta^p} > 0 \Longrightarrow \dot{p_c} < 0$). Note that the hardening rule has the character of the mixed hardening.

Let us introduce the so-called over-consolidation ratio (OCR) which is a relation between the initial preconsolidation pressure p_{c0} and the initial compressive pressure:

$$OCR = -\frac{p_{c0}}{p_0} \tag{4.18}$$

If $OCR \gg 1$ we deal with overconsolidated soil which has a tendency to a dilatant (softening) behaviour. The soil for which $OCR = 1$ is called normally consolidated and is prone to contraction (hardening).

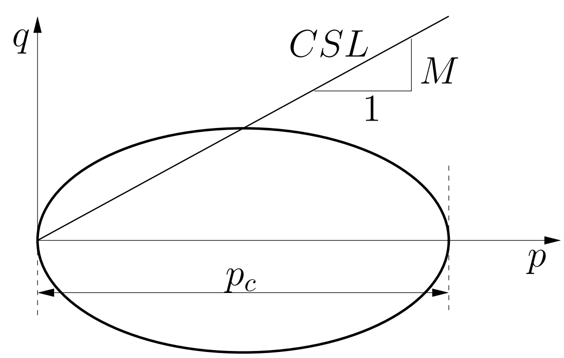

Figure 4.2: Material model: yield surface. CSL denotes the critical state line.

Unlike in [67], the additional pressure shift parameter in the yield condition has been abandoned here. It was proposed in [22] to enable the start of computations in the absence of initial stresses and motivated by cohesion, but its physical significance is not sufficiently clear, since the initial state of soil always involves some compression (positive pressure).

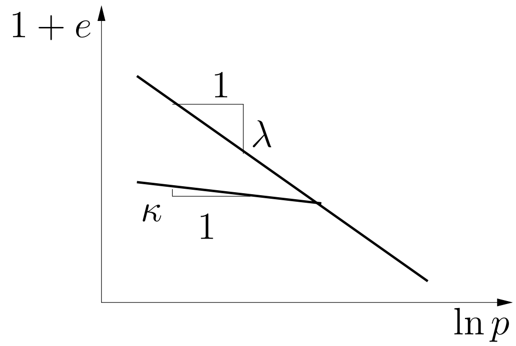

Figure 4.3: Material model: elastic behaviour.

4.3 Linearization in local Cam-clay plasticity

The rate equations are integrated over a finite time step with the implicit backward Euler integration scheme. At the beginning of an increment, denoted by '0', the stresses, the total and elastic strains and hardening parameter are known. The goal is to update these quantities. Here, the algorithm proposed in [6] is employed, cf. also [22, 28, 74].

Assuming the usual additive decomposition of the strain rates we can write for the volumetric strain rate as

$$\mathrm{d}\theta = \mathrm{d}\theta^{\mathrm{e}} + \mathrm{d}\theta^{\mathrm{p}} = \mathrm{d}\theta^{\mathrm{e}} - \mathrm{d}\Lambda \frac{\partial F}{\partial p} = \mathrm{d}\theta^{\mathrm{e}} - 2\mathrm{d}\Lambda M^2 (p-a) \tag{4.19}$$

and for the rate of the deviatoric strain vector as

$$\mathrm{d}\boldsymbol{\gamma} = \mathrm{d}\boldsymbol{\gamma}^{\mathrm{e}} + \mathrm{d}\boldsymbol{\gamma}^{\mathrm{p}} = \mathrm{d}\boldsymbol{\gamma}^{\mathrm{e}} + \mathrm{d}\Lambda \frac{\partial F}{\partial q} \left(\frac{\partial q}{\partial \boldsymbol{\xi}}\right)^{\mathrm{T}} = \mathrm{d}\boldsymbol{\gamma}^{\mathrm{e}} + 3\mathrm{d}\Lambda \boldsymbol{R}\boldsymbol{\xi}. \tag{4.20}$$

For a finite increment the update of the deviatoric stress is given by:

$$\boldsymbol{\xi} = \boldsymbol{\xi}_0 + 2\bar{G}\boldsymbol{R}^{-1}(\Delta\boldsymbol{\gamma} - \Delta\boldsymbol{\gamma}^{\mathrm{p}}). \tag{4.21}$$

If we assume that eq. (4.19) is valid for finite increments, the substitution of $\Delta\boldsymbol{\gamma}^{\mathrm{p}} = 3\Delta\Lambda\boldsymbol{R}\boldsymbol{\xi}$ into eq. (4.21) leads to a convenient relation between $\boldsymbol{\xi}$ and the trial deviatoric stress $\boldsymbol{\xi}_{trial}$:

$$\boldsymbol{\xi} = \frac{1}{1+6\bar{G}\Delta\Lambda}\boldsymbol{\xi}_{trial}, \qquad \boldsymbol{\xi}_{trial} = \boldsymbol{\xi}_0 + 2\bar{G}\boldsymbol{R}^{-1}\Delta\boldsymbol{\gamma}. \tag{4.22}$$

Then, the effective deviatoric stress is calculated according to:

$$q = \frac{1}{1+6\bar{G}\Delta\Lambda}\sqrt{\frac{3}{2}\boldsymbol{\xi}_{trial}^T \boldsymbol{R}\boldsymbol{\xi}_{trial}}. \tag{4.23}$$

In order to return to the yield surface using a fully implicit integration scheme, the following nonlinear system of equations is defined:

$$\boldsymbol{r} = \boldsymbol{r}(\boldsymbol{s}(\boldsymbol{\epsilon}), \boldsymbol{\epsilon}), \tag{4.24}$$

where $\boldsymbol{s}$ is a vector of the primary unknowns $\boldsymbol{s} = [p, q, \bar{G}, p_c, \Delta\Lambda]$ and $\boldsymbol{r}$ is a vector of residuals $\boldsymbol{r} = [r_1, r_2, r_3, r_4, r_5]$. The residuals in vector $\boldsymbol{r}$ are given by:

$$\begin{aligned}
r_1 &= p - p_0 \exp\left[-\frac{1+e_0}{\kappa}\Delta\theta^{\mathrm{e}}\right], && (4.25a)\\
r_2 &= q - \frac{1}{1+6\bar{G}\Delta\Lambda}\sqrt{\frac{3}{2}\left[\boldsymbol{\xi}_0 + 2\bar{G}\boldsymbol{R}^{-1}\Delta\boldsymbol{\gamma}\right]^T \boldsymbol{R}\left[\boldsymbol{\xi}_0 + 2\bar{G}\boldsymbol{R}^{-1}\Delta\boldsymbol{\gamma}\right]}, && (4.25b)\\
r_3 &= \bar{G} - \frac{3}{2}\frac{1-2\nu}{1+\nu}\frac{p_0(1-\exp\left[-\frac{1+e_0}{\kappa}\Delta\theta^{\mathrm{e}}\right])}{\Delta\theta^{\mathrm{e}}}, && (4.25c)\\
r_4 &= p_c - p_{c0}\exp\left[-\frac{1+e_0}{\lambda-\kappa}\Delta\theta^{\mathrm{p}}\right], && (4.25d)\\
r_5 &= q^2 + M^2 p\,(p - p_c). && (4.25e)
\end{aligned}$$

In the above system, $\Delta\theta^{\mathrm{e}}$ and $\Delta\theta^{\mathrm{p}}$ are obtained from eq. (4.19) as functions of $p,\ a$ and $\Delta\Lambda$.

The set of equations (4.25) is solved using the Newton-Raphson iteration scheme:

$$\boldsymbol{s}_{i+1} = \boldsymbol{s}_i - \left[\frac{\partial\boldsymbol{r}}{\partial\boldsymbol{s}}\right]^{-1}\boldsymbol{r}_i. \tag{4.26}$$

The consistent tangent operator is given by:

$$\frac{\mathrm{d}\boldsymbol{\sigma}}{\mathrm{d}\boldsymbol{\epsilon}} = \frac{\partial\boldsymbol{\xi}}{\partial\boldsymbol{\epsilon}} - \boldsymbol{\Pi}\frac{\partial p}{\partial\boldsymbol{\epsilon}} - \left[\frac{\partial\boldsymbol{\xi}}{\partial\boldsymbol{s}} - \boldsymbol{\Pi}\frac{\partial p}{\partial\boldsymbol{s}}\right]\left[\frac{\partial\boldsymbol{r}}{\partial\boldsymbol{s}}\right]^{-1}\left[\frac{\partial\boldsymbol{r}}{\partial\boldsymbol{\epsilon}}\right] \tag{4.27}$$

and the respective derivatives are listed in the Appendix.

4.4 Non-associated plasticity

In order to describe the soil behaviour in a more realistic way and to model the phenomenon of static liquefaction, the option of non-associative plasticity is required. Liquefaction is a phenomenon in which the shear resistance of soil vanishes due to the increase of pore pressure which reduces the effective pressure on solid particles. The plastic potential for non-associative plasticity is proposed in the form analogous to eq. 4.15:

$$G = q^2 + \bar{M}^2 p(p - p_{cG}) \tag{4.28}$$

in which $\bar{M}$ is a function of dilatation angle ψ:

$$\bar{M} = \frac{6\sin\psi}{3-\sin\psi}. \tag{4.29}$$

Variable p_{cG} is undefined in eq.(4.28) and has to be eliminated from the flow vector $\partial G/\partial p$ [75]. From condition $F = 0$, and denoting $\eta = \frac{q}{p}$, we can express overconsolidation measure

p_c as:

$$p_c = p\left[\left(\frac{\eta}{M}\right)^2 + 1\right] \tag{4.30}$$

Analogically, we can write:

$$p_{cg} = p\left[i\left(\frac{\eta}{\bar{M}}\right)^2 + 1\right] \tag{4.31}$$

Substituting eq. (4.31) into eq. (4.28) we can compute the flow vector $\partial G/\partial p$:

$$\frac{\partial G}{\partial p} = p\bar{M}^2 - p\eta^2 \tag{4.32}$$

However, we cannot use η computed at the trial state, so knowing that

$$\frac{\partial F}{\partial p} = pM^2 - p\eta^2 \tag{4.33}$$

we find:

$$p\eta^2 = pM^2 - \frac{\partial F}{\partial p} \tag{4.34}$$

and eventually obtain:

$$\frac{\partial G}{\partial p} = p(\bar{M}^2 - M^2) + \frac{\partial F}{\partial p} \tag{4.35}$$

where:

$$\frac{\partial F}{\partial p} = M^2(2p - p_c) \tag{4.36}$$

The volumetric strain rate is now given by:

$$\mathrm{d}\theta = \mathrm{d}\theta^{\mathrm{e}} + \mathrm{d}\theta^{\mathrm{p}} = \mathrm{d}\theta^{\mathrm{e}} - \mathrm{d}\Lambda\frac{\partial G}{\partial p} = \mathrm{d}\theta^{\mathrm{e}} - \mathrm{d}\Lambda M^2(2p - p_c) - \mathrm{d}\Lambda p(\bar{M}^2 - M^2). \tag{4.37}$$

Consequently all the functions of $\mathrm{d}\theta^{\mathrm{e}}$ and $\mathrm{d}\theta^{\mathrm{p}}$ have to be corrected and derivatives with respect to the hydrostatic pressure and the rate of the plastic multiplier have to be recalculated (see Appendix).

4.5 Numerical differentiation for consistent tangent

The exact linearization requires the computation of many derivatives. This task is sometimes cumbersome and analytical derivations can involve mistakes. Therefore, as was proposed among others in [25, 51, 52], numerically computed derivatives can either be used to check the analytical derivations (unless they are performed symbolically using for instance the MAPLE package) or simply to calculate the consistent tangent operator altogether.

In this work all approaches have been combined since the issue of correct computation of derivatives within the Newton algorithm turned out to be a nontrivial task due to interdependence of the involved variables. The numerical approximation of derivatives of function $F(\boldsymbol{x})$ in a linear space with versors $\boldsymbol{e}_i$ is performed using the finite difference central scheme:

$$\frac{\partial F(\boldsymbol{x})}{\partial x_i} = \frac{F(\boldsymbol{x} + h_i \boldsymbol{e}_i) - F(\boldsymbol{x} - h_i \boldsymbol{e}_i)}{2h_i} + \mathcal{O}(h_i^2) \tag{4.38}$$

or forward scheme

$$\frac{\partial F(\boldsymbol{x})}{\partial x_i} = \frac{F(\boldsymbol{x} + h_i \boldsymbol{e}_i) - F(\boldsymbol{x})}{h_i} + \mathcal{O}(h_i), \tag{4.39}$$

in which $x_i = \boldsymbol{x} \cdot \boldsymbol{e}_i$, $h_i = h_{opt} \max\{1.0, |x_i|\}$ and the optimal step (perturbation) size h_{opt} needs to be selected via numerical experiment (some guidelines are proposed in [51]). If f is a tensor-valued function of $\boldsymbol{x}$, the computations must be performed element by element. In this research the forward scheme has been used due to its simplicity (it requires only one additional determination of the value of f) with $h_{opt} = 10^{-7}$ or 10^{-8}.

4.6 One-element tests

In order to verify the material model implementation a set of simple one-element tests are performed. They also allow one to find out the features of the numerical model and understand the soil behaviour better.

For all of the calculations presented in the current section the drained conditions are considered. The calculations are carried out using 8-noded plane strain finite element (with the discretization of displacements). The element size is: 1m $\times$ 1m. The following material data are adopted: Poisson's ratio $\nu = 0.3$, swelling index $\kappa = 0.013$, initial void ratio $e_0 = 1.0$, compression index $\lambda = 0.05$, and material constant $M = 1.0$.

4.6.1 Biaxial compression

The biaxial compression test is performed for two cases, i.e. slightly preconsolidated soil (OCR=2) and strongly preconsolidated soil (OCR=10). In Fig. 4.4 on the left the initial stress generation is depicted. The initial stress vector is $\boldsymbol{\sigma}_0 = [-0.2, -0.2, -0.08, 0.0]$ MPa. The compression process is driven under displacement control, cf. Fig. 4.4 on the right. The results of calculations are presented in Figs 4.5-4.8. As expected, the responses obtained for the two cases are completely different.

When a loose sample is loaded, its volume decreases (cf. Fig. 4.5) inducing material densification and thus hardening. The initial yield surface expands, the value of preconsolidation pressure p_c increases from the initial value of p_c0. For a dense sample the peak load and then material softening is observed. This fact is associated with the initial contraction and subsequent dilatation of the specimen (cf. Fig 4.7). In Fig. 4.8 the evolution of the yield surface is shown. In this case the value of p_c decreases and the ellipse shrinks.

The explanation of such a behaviour lies in the granular structure of the material. When the dense sample is loaded, the pore volume becomes smaller at the beginning but later the only possibility for the material is to dilate. On the other hand, as illustrated in Fig. 2.2, the loose configuration has to contract (densify).

In both cases the yield surface evolution continues until the stress path intersects the critical state line. After that, the strength and volume of the specimen remain constant and the plastic flow becomes purely deviatoric.

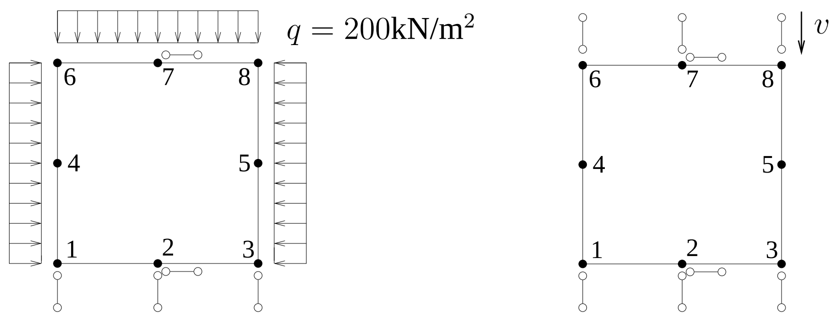

Figure 4.4: Biaxial compression test. Initial stress and loading - static and kinematic boundary conditions (initial stress remains).

4.6.2 Triaxial compression

One-element triaxial compression test is performed for normally consolidated soil (OCR=1) and heavily preconsolidated soil (OCR=5). In Fig. 4.9 on the left the initial stress generation is depicted. The initial stress components have values $\boldsymbol{\sigma}_0 = [-0.2, -0.2, -0.2, 0.0]$ MPa. The compression process is driven under displacement control, cf. Fig. 4.9 on the right. In Figs 4.10-4.13 the results of numerical simulations are presented.

Figs 4.10-4.11 show that the normally consolidated soil exhibits contraction and thus hardening. The value of p_c increases, the yield surface expands. On the contrary, when heavily preconsolidated soil is loaded the contraction and material softening is observed. The value of preconsolidation pressure decreases, see Figs 4.12-4.13.

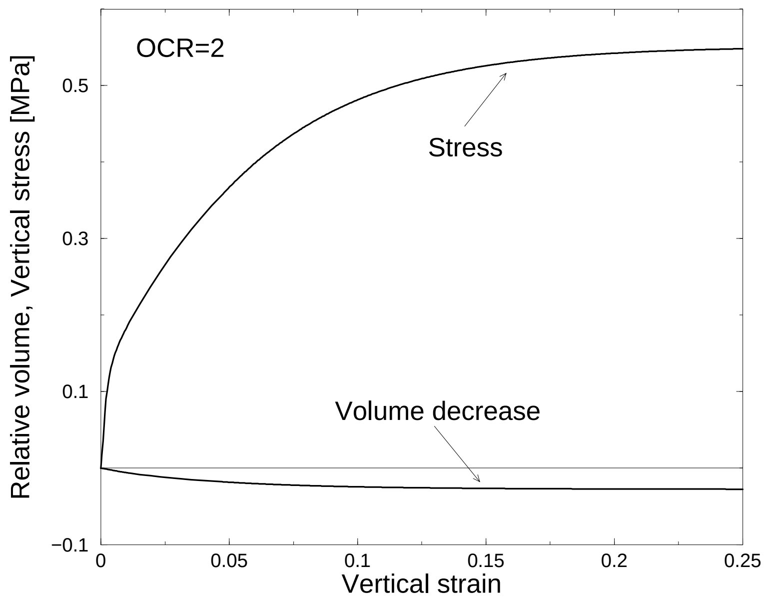

Figure 4.5: Stress-strain diagram for the vertical direction and relative volume evolution for normally consolidated soil and drained state (biaxial compression)

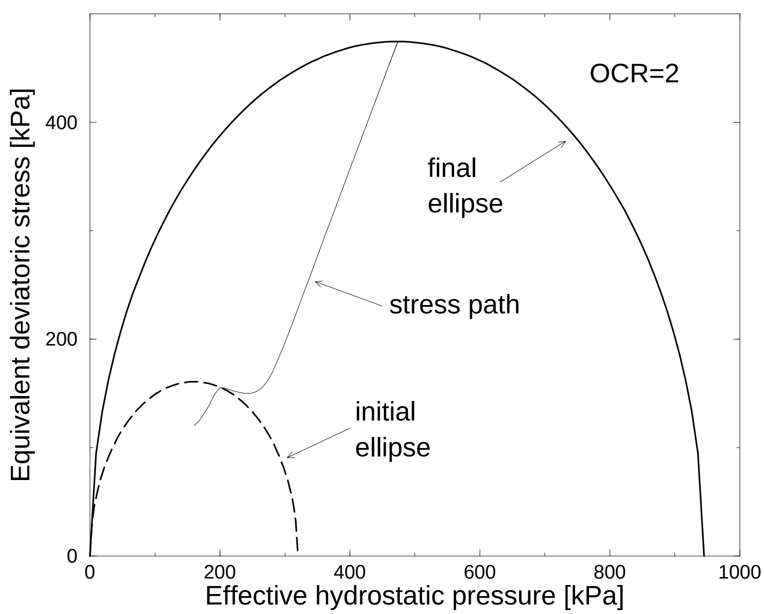

Figure 4.6: Yield surface evolution for normally consolidated soil and drained state during biaxial compression test

In both cases, the calculations are completed for the critical state with stress ratio $\frac{q}{p} = M$. After this state is reached, only the deviatoric plastic strain increments are observed, the material strength and volume remain constant and the yield surface evolution stops.

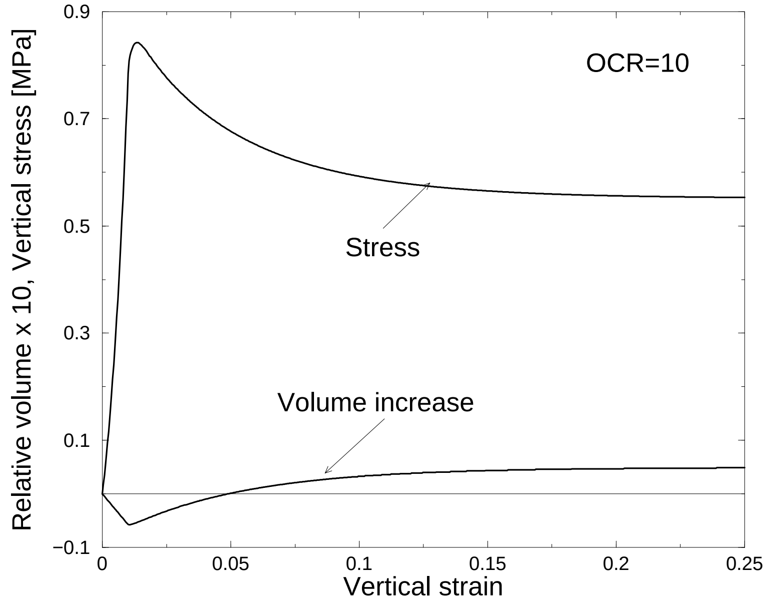

Figure 4.7: Stress-strain diagram for the vertical direction and relative volume evolution for strongly preconsolidated soil and drained state (biaxial compression)

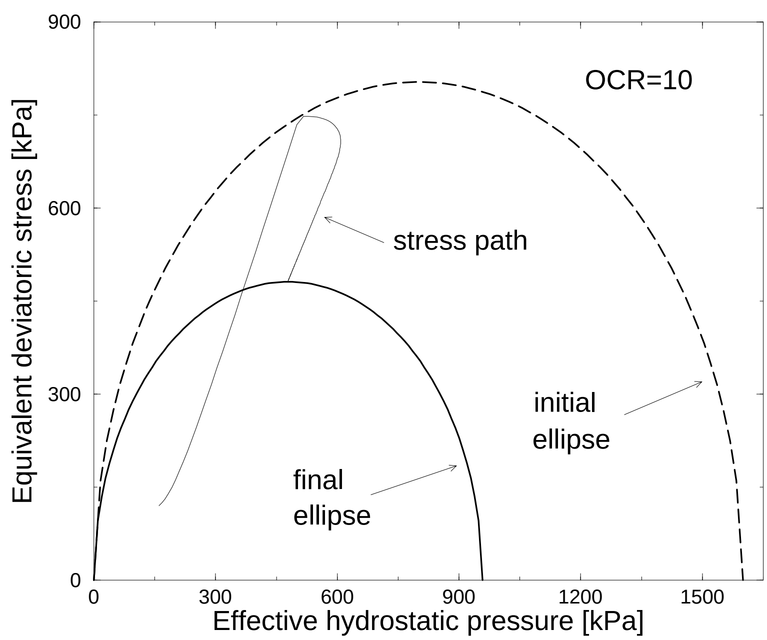

Figure 4.8: Yield surface evolution for strongly preconsolidated soil and drained state during biaxial compression test

4.6.3 Shear

The third of one-element tests is performed again for lightly (OCR=2) and heavily (OCR=5) preconsolidated material. The initial stress vector $\boldsymbol{\sigma}_0 = [-0.2, -0.2, -0.08, 0.0]$ MPa is

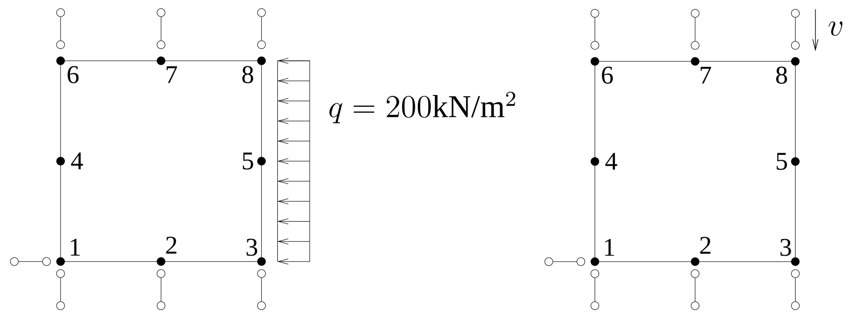

Figure 4.9: Triaxial compression test. Initial stress and loading - static and kinematic boundary conditions (initial stress remains).

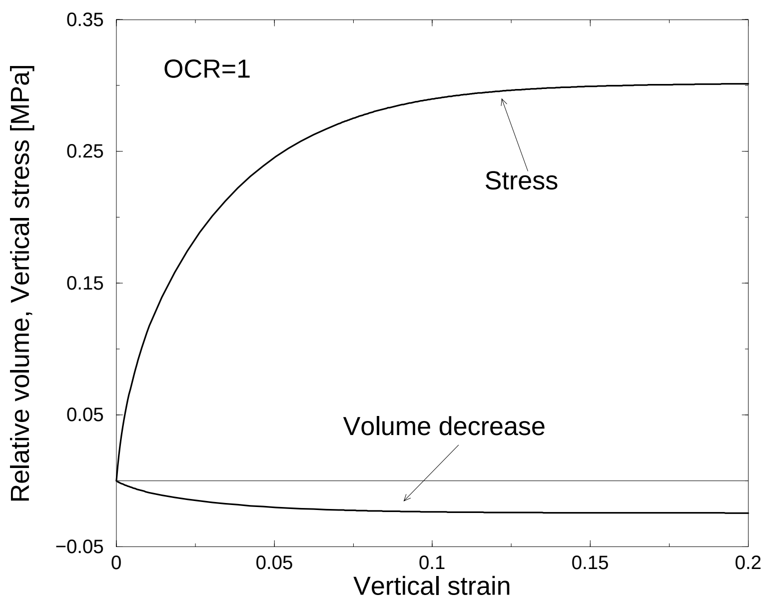

Figure 4.10: Stress-strain diagram for the vertical direction and relative volume evolution for normally consolidated soil and drained state (triaxial compression)

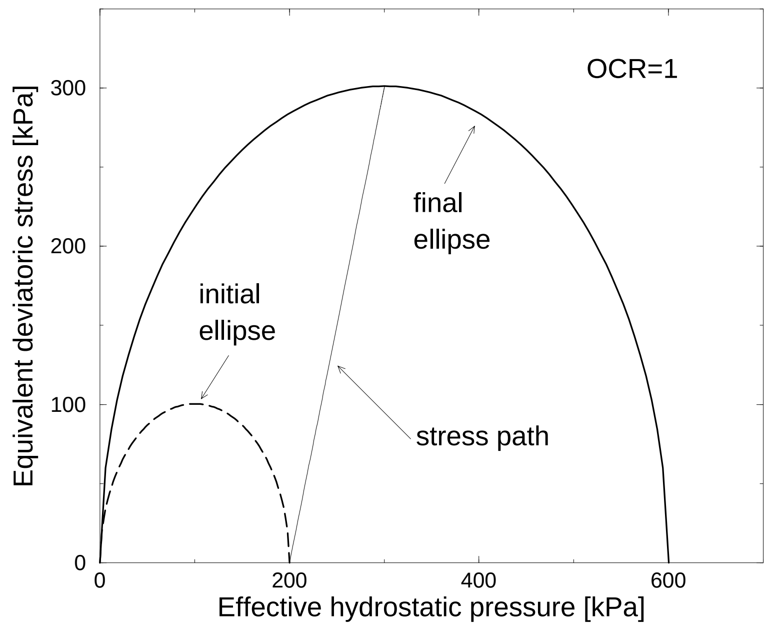

Figure 4.11: Yield surface evolution for normally consolidated soil and drained state during triaxial compression test

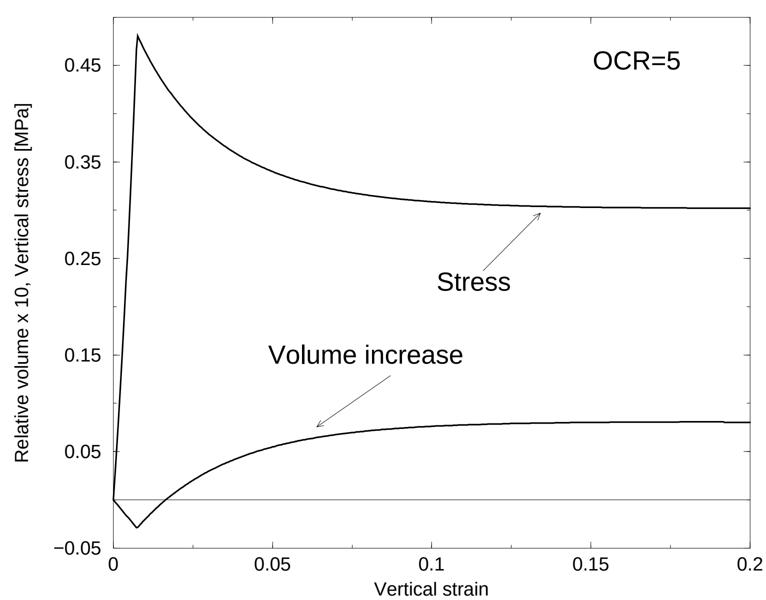

Figure 4.12: Stress-strain diagram for the vertical direction and relative volume evolution for strongly preconsolidated soil and drained state (triaxial compression)

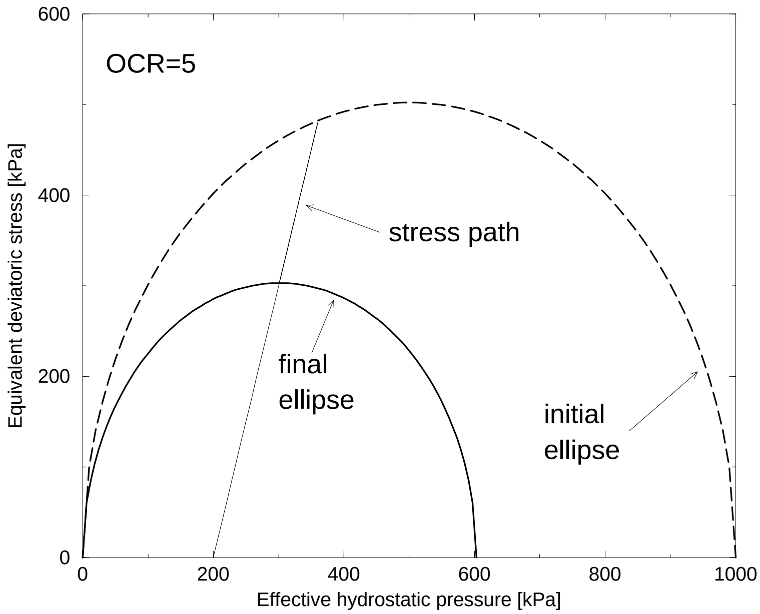

Figure 4.13: Yield surface evolution for strongly preconsolidated soil and drained state during triaxial compression test

generated as shown in Fig. 4.14 on the left. The shear process is driven under displacement control, cf. Fig. 4.14 on the right. In Figs 4.15-4.16 the results for the soil with OCR=2 are shown. As in the previous tests for the lightly overconsolidated material the volume of the sample decreases inducing hardening behaviour. For the heavily preconsolidated soil the peak load and then material softening associated with dilatation is encountered. The initial yield surface is shrinking due to a decreasing value of hardening/softening parameter p_c, cf. Figs 4.17-4.18.

In both cases, the yield surface stops evolving when the stress ratio $\frac{q}{p} = M$ is reached and the flow becomes purely deviatoric with constant material strength and volume.

It is necessary to point out that the volume changes start when the process becomes plastic. Thus, the stress path before reaching the yield surface is parallel to q-axis. The effective hydrostatic pressure does not change as long as $\Delta\theta = \Delta\theta^p = 0$.

4.7 Mesh-dependent localization test - biaxial compression

In order to show the mesh-dependence of the numerical solution the biaxial compression test is repeated for a multi-element configuration. The size of the specimen is now 1m $\times$ 2m.

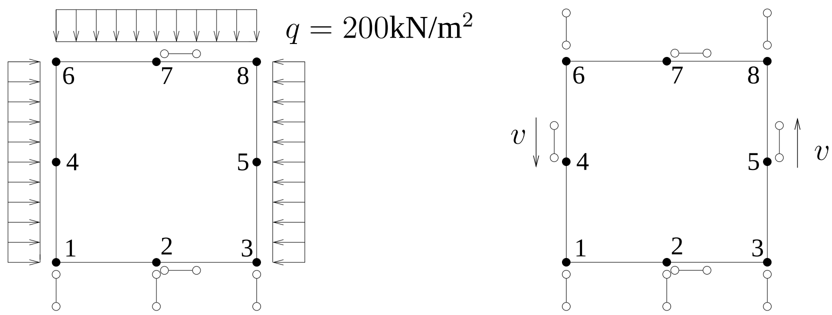

Figure 4.14: Pure shear test. Initial stress and loading - static and kinematic boundary conditions (initial stress remains).

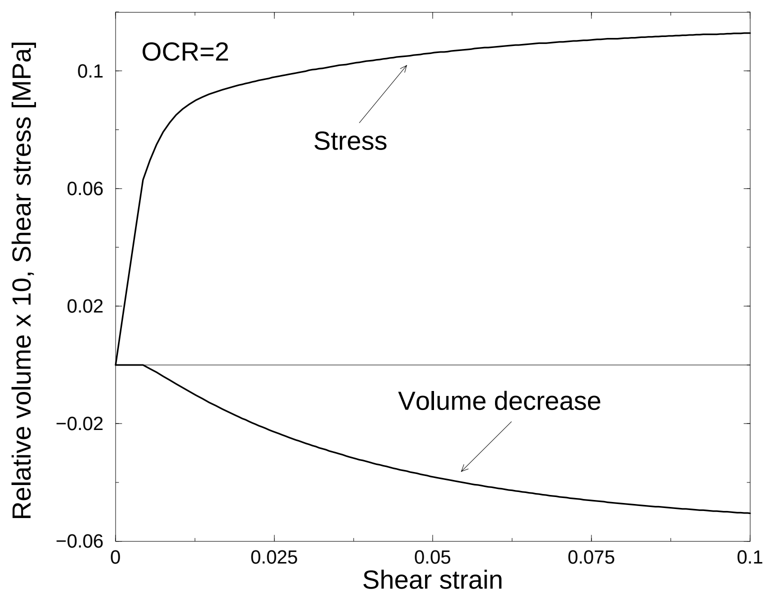

Figure 4.15: Stress-strain diagram for the vertical direction and relative volume evolution for normally consolidated soil and drained state (pure shear)

The model is discretized with 10 $\times$ 20, 20 $\times$ 40 and 40 $\times$ 80 finite elements.

The following material data are adopted: Poisson's ratio $\nu = 0.2$, swelling index $\kappa = 0.013$, initial void ratio $e_0 = 1.0$, hardening parameter $p_{c0} = 2.0$ MPa, compression index $\lambda = 0.032$, material constant $M = 1.1$. The initial stresses $\boldsymbol{\sigma}_0 = [-0.2, -0.2, -0.08, 0.0]$ MPa are generated in a similar way as in the case of one-element tests. To load the sample a vertical traction on the top edge is prescribed. For the local model the diplacement control cannot be used due to a snap-back response and the linearized arc length control is employed.

To initiate a shear band formation a small area in the bottom left-hand corner of the sample (one element for the coarse mesh, four elements for the medium one and sixteen for the fine one) is assigned a 10% smaller initial value of the overconsolidation measure

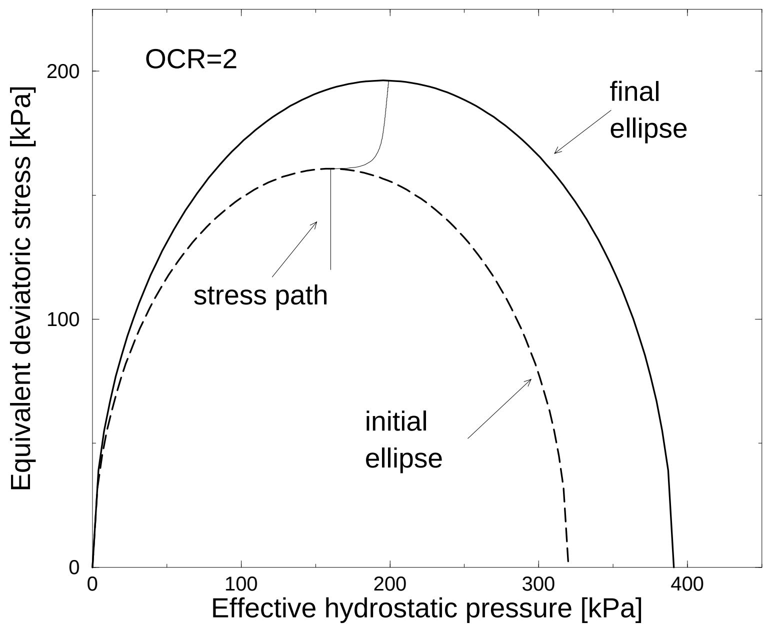

Figure 4.16: Yield surface evolution for normally consolidated soil and drained state during pure shear test

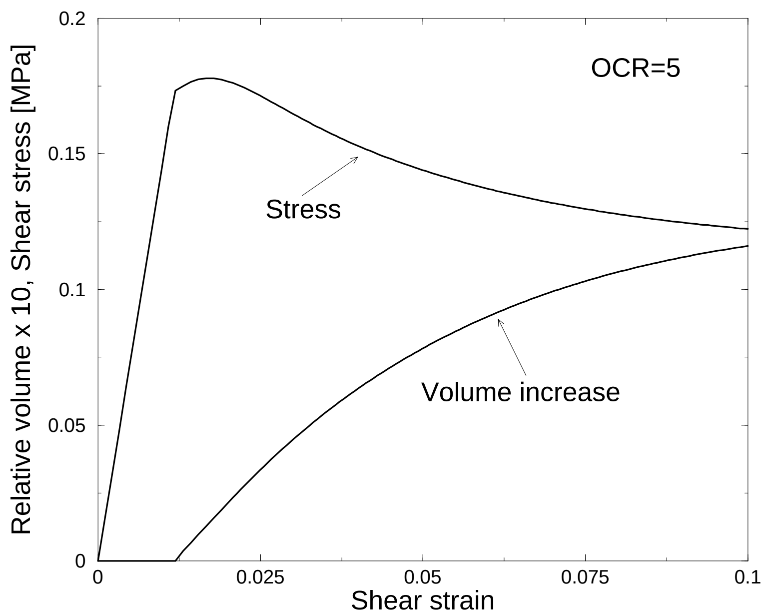

Figure 4.17: Stress-strain diagram for the vertical direction and relative volume evolution for strongly preconsolidated soil and drained state (pure shear)

$p_{c0} = 1.8$ MPa.

The sample with the area of imperfection marked is shown in Fig. 4.19. In Fig. 4.20 some experimental results of this test are shown.

In Figs 4.21-4.22 the results for the coarse, medium and fine meshes for the local Cam-

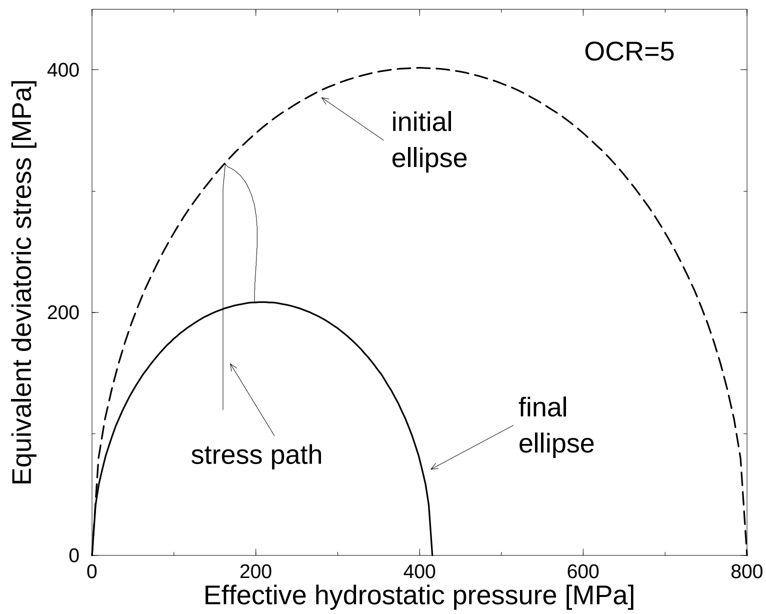

Figure 4.18: Yield surface evolution for strongly preconsolidated soil and drained state during pure shear test

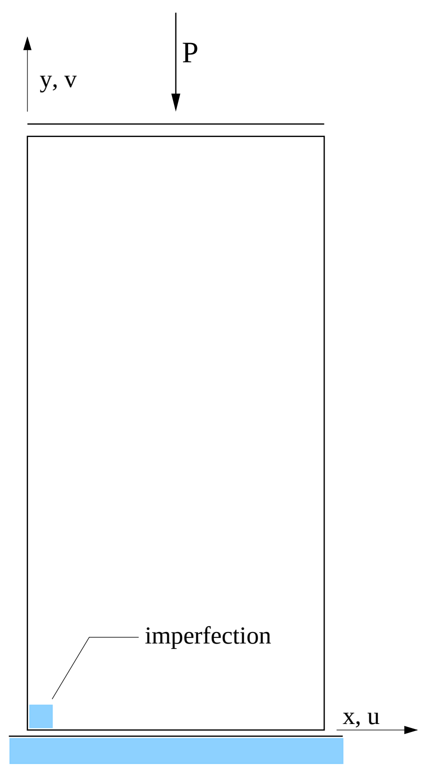

Figure 4.19: Biaxial compression test: the sample and imperfection location

clay model and drained conditions are shown. Since the material model used in computations is not regularized we observe mesh sensitivity of the obtained diagrams and deformation

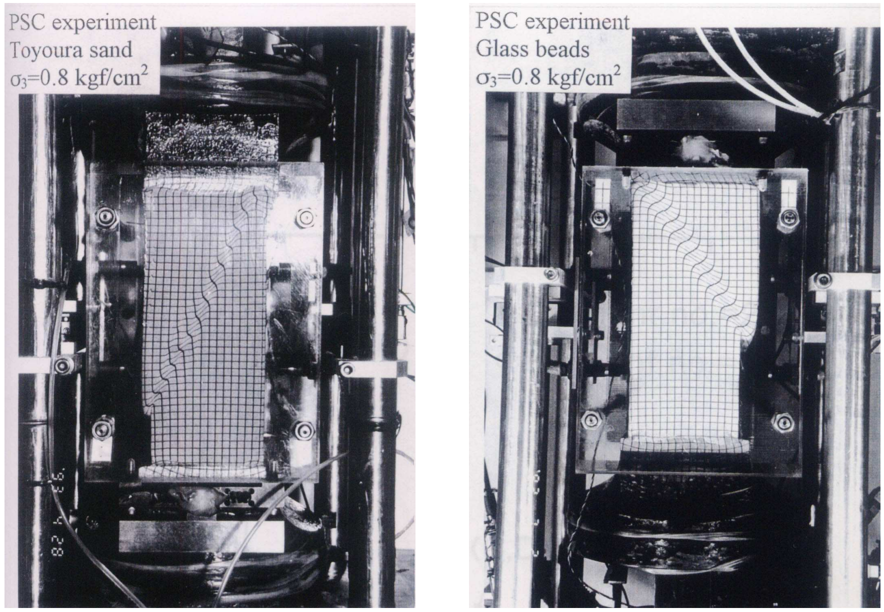

Figure 4.20: Biaxial compression test: experimental results, after [64]

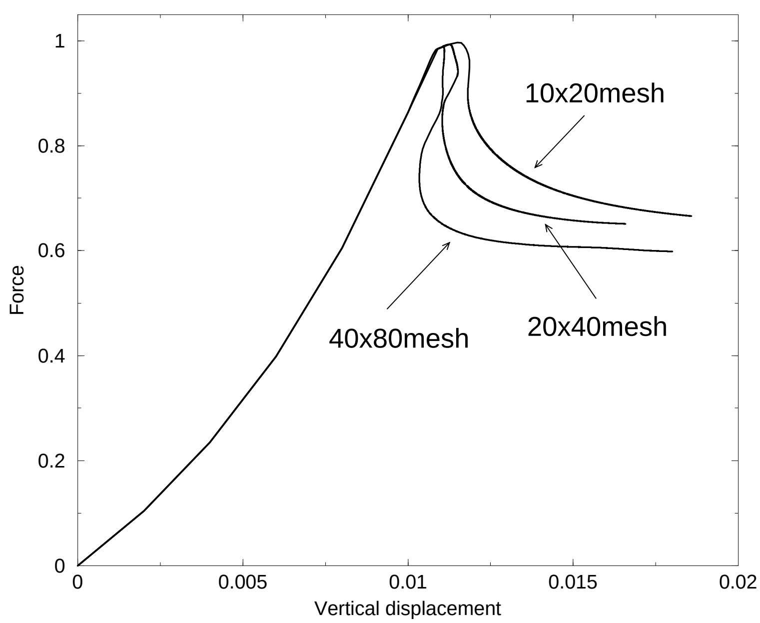

Figure 4.21: Load-deformation curves for local model in biaxial compression test

patterns. In the load-deformation curve in Fig. 4.21 a slight snap-back for the coarse mesh and a more distinct one for the medium and fine meshes are visible. Figs 4.23-4.22 show that the width of the shear band strongly depends on the discretization. Strains indeed localize in the narrowest possible area determined by the element size.

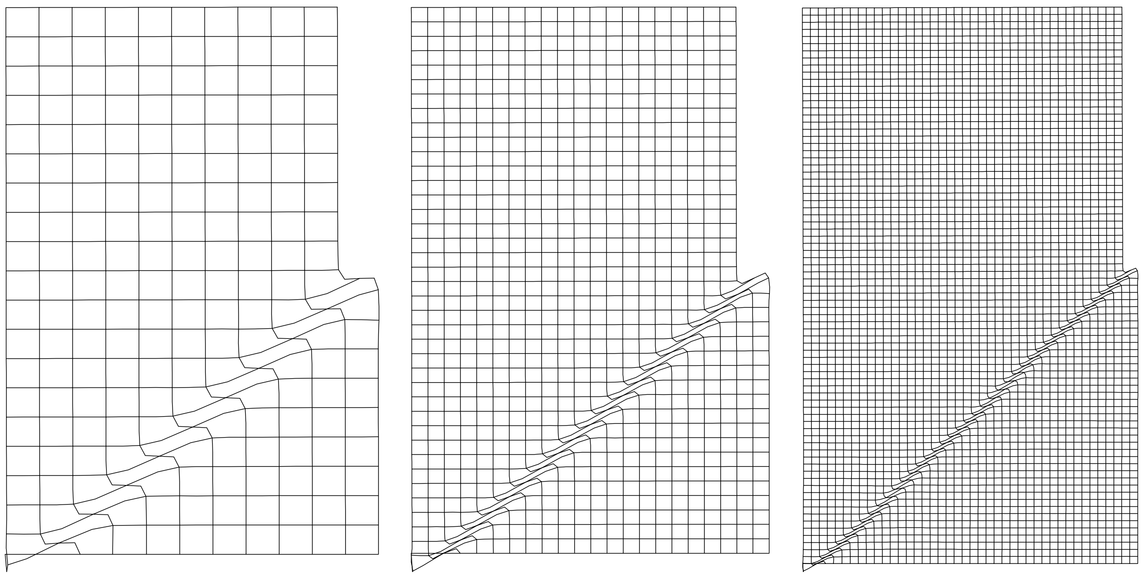

Figure 4.22: Deformed meshes for local model in biaxial compression test

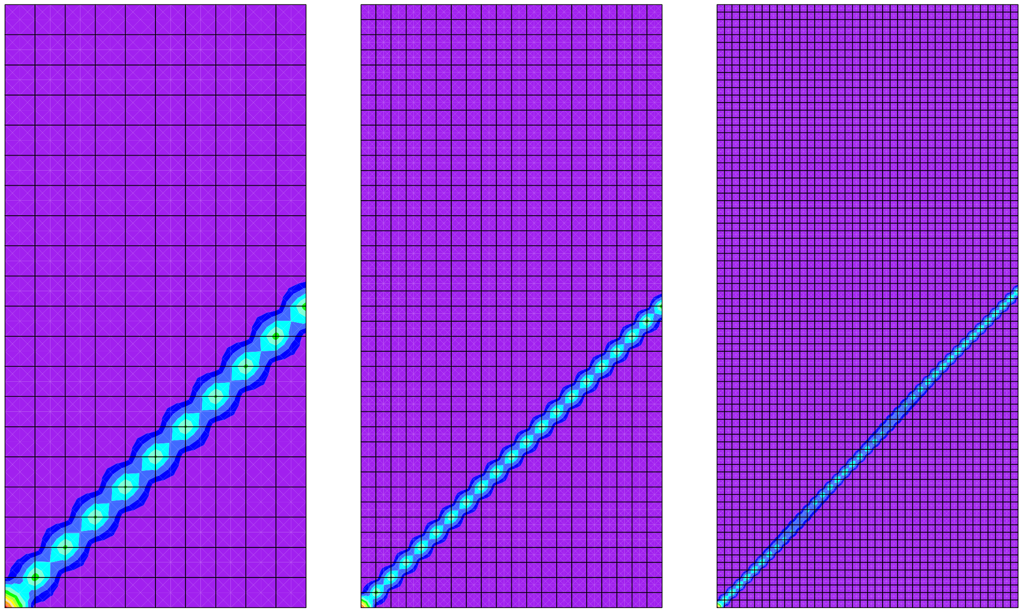

Figure 4.23: Equivalent plastic strain distribution for local model in biaxial compression test

Chapter 5

One- and two-phase modelling

The structure of soil is very complex. It is a multiphase material which consists of a solid skeleton and voids filled with fluids (usually water and air). Generally, voids are partly occupied by water and partly by air. We call such soil partially saturated (three-phase medium). In the case when pores are completely filled with water we deal with fully saturated soil (two-phase medium). The soil can also be dry if no free water is present. Interactions of the phases strongly affect the properties and behaviour of soils. In Fig. 5.1 the model of three-phase medium is presented. The figure contains the interpretation of some geotechnical notions like porosity and saturation ratio.

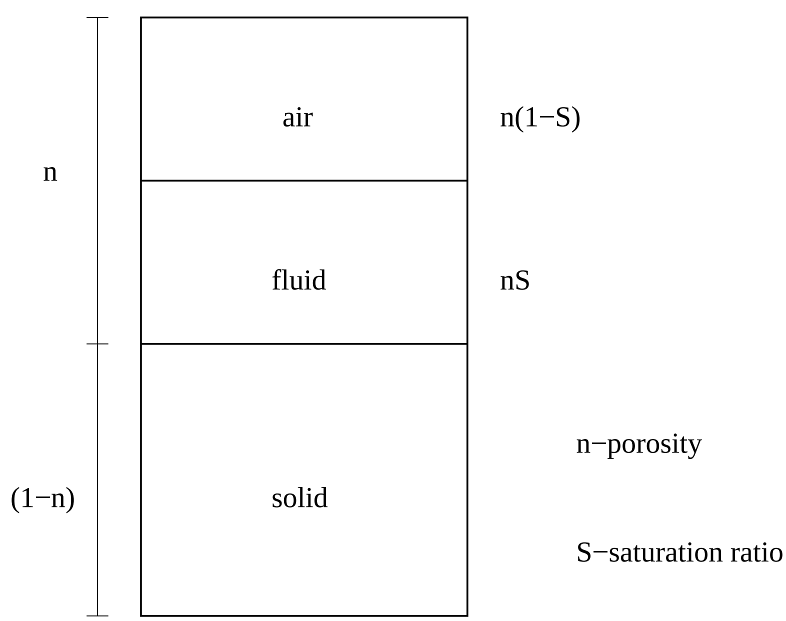

Figure 5.1: Thee-phase material model, after [86]

5.1 Partially saturated soil

Partially saturated soil is a three-phase material. The problem variables are: the solid displacement, water pore pressure and air pore pressure. In the present model it is assumed that the gaseous phase remains at constant (atmospheric) pressure. This assumption allows one to reduce the number of problem variables from three to two (solid displacement, water pore pressure). Such a two-phase medium, with the assumption of incompressibility of solid grains, is governed by the following two equations [73, 90]:

$$\boldsymbol{L}^{\mathrm{T}}\boldsymbol{\sigma}_t + \hat{\rho}\boldsymbol{g} = \boldsymbol{0}, \tag{5.1}$$

$$\boldsymbol{\nabla}\cdot\dot{\boldsymbol{u}} + \boldsymbol{\nabla}\cdot\boldsymbol{v}_d - (nS_f + n\frac{\partial S_f}{\partial p_f}K_f)\dot{\theta}_f = 0, \quad \dot{\theta}_f = -\frac{\dot{p_f}}{K_f} \tag{5.2}$$

with:

$$\boldsymbol{\sigma_t} = \boldsymbol{\sigma} - \boldsymbol{\Pi}\, S_f\, p_f, \tag{5.3}$$

$$\hat{\rho} = (1-n)\rho_s + nS_f\rho_f, \tag{5.4}$$

$$\boldsymbol{v}_d = -k_r(S_f)\boldsymbol{k}\boldsymbol{\nabla}(\frac{p_f}{\gamma_f} + z), \tag{5.5}$$

where $\hat{\rho}$ - saturated density of the soil-fluid mixture, ρ_s - density of the solid phase, ρ_f - density of the fluid phase, $\boldsymbol{g}$ - gravitation vector, $\boldsymbol{u}$ - displacement vector, n - porosity θ_f - volumetric strain of compressible fluid, $\boldsymbol{k}$ - permeability matrix and z-coordinate in the direction of gravitation governing the stationary state of pore pressures without loading, K_f - bulk modulus for the fluid, S_f - saturation ratio, $k_r(S_f)$ - relative permeability coefficient. The porosity n and void ratio e are related by:

$$n = \frac{e}{1+e}, \quad e = \frac{V_p}{V_s}, \tag{5.6}$$

where V_p - pore volume and V_s - skeleton volume.

Eqs (5.1) and (5.2) require appropriate boundary and initial conditions. The initial conditions for displacements and pore pressures at time $t = 0$ are:

$$\boldsymbol{u} = \boldsymbol{u}_0, \tag{5.7a}$$

$$p_f = p_{f0}. \tag{5.7b}$$

The boundary conditions to be satisfied at any time t are:

$$\boldsymbol{\sigma}_t\boldsymbol{\nu} = \bar{\boldsymbol{t}} \;\; on \;\; \Gamma_t, \tag{5.8a}$$

$$\boldsymbol{v}_d\boldsymbol{\nu} = \bar{\boldsymbol{q}} \;\; on \;\; \Gamma_q, \tag{5.8b}$$

$$\boldsymbol{u} = \bar{\boldsymbol{u}} \;\; on \;\; \Gamma_u, \tag{5.8c}$$

$$p_f = \bar{p}_f \;\; on \;\; \Gamma_p, \tag{5.8d}$$

where $\Gamma_t \cdots \Gamma_p$ are appropriate boundary parts, such that $\Gamma_t \cap \Gamma_u = \varnothing$, $\Gamma_t \cup \Gamma_u = \Gamma$, $\Gamma_q \cap \Gamma_p = \varnothing$, $\Gamma_q \cup \Gamma_p = \Gamma$. In Fig. 5.1 the example of the boundary conditions is shown.

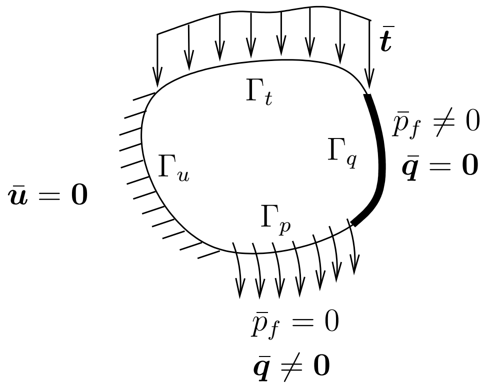

Figure 5.2: Boundary conditions for two-phase medium

For $S_f = 1$ this formulation collapses to the fully saturated soil.

5.2 Fully saturated soil

Fully saturated soil is a two-phase material. The problem variables are: the solid displacement vector and the water pore pressure. Such a two-phase medium, with the assumption of incompressibility of solid grains, is governed by the following two equations [73,90]:

$$\boldsymbol{L}^{\mathrm{T}} \boldsymbol{\sigma}_t + \hat{\rho} \boldsymbol{g} = \mathbf{0}, \tag{5.9}$$

$$\boldsymbol{\nabla}^{\mathrm{T}} \dot{\boldsymbol{u}} + \boldsymbol{\nabla}^{\mathrm{T}} \boldsymbol{v}_d + n \frac{\dot{p}_f}{K_f} = 0, \tag{5.10}$$

with:

$$\boldsymbol{\sigma_t} = \boldsymbol{\sigma} - \boldsymbol{\Pi}\, p_f, \tag{5.11}$$

$$\hat{\rho} = (1-n)\rho_s + n\rho_f, \tag{5.12}$$

and Darcy's fluid flow velocity given by:

$$\boldsymbol{v}_d = -\boldsymbol{k} \boldsymbol{\nabla} \frac{p_f}{\gamma_f}, \tag{5.13}$$

notice that p_f is the excess pore pressure.
Eq. (5.9) represents the balance of momentum and eq. (5.10) the balance of mass. They require appropriate boundary and initial conditions, cf. eq.(5.8) and eq.(5.8).

5.3 Drained state

If we assume long-term load together with appreciable permeability, fluid flows out freely and in this case pore pressures are independent of the material deformation (excess pore pressure is equal to zero; $p_f = 0$). We can consider soil as a one phase medium and apply the algorithms described in Sections 4.3 and/or 6.2.

5.4 Undrained state

Another case where we can limit our consideration to one-phase medium is the undrained state. We deal with such a case for rapidly loaded soil and/or zero permeability, when the fluid motion is prevented. In this case Darcy's velocity is equal to zero ($\boldsymbol{v}_d = \mathbf{0}$) and from the mass balance equation (5.10) we have:

$$\dot{\theta} = \boldsymbol{\nabla} \cdot \dot{\boldsymbol{u}} = n\dot{\theta}_f, \tag{5.14}$$

where the velocity of fluid volume change $\dot{\theta}_f$ can be written as:

$$\dot{\theta}_f = -\frac{\dot{p}_f}{K_f}. \tag{5.15}$$

Assuming the linear relation between the rate of the pore pressure and the rate of the material volume change we eventually obtain:

$$p_f = -\frac{K_f}{n}\theta = -\frac{K_f(1+e)}{e}\theta. \tag{5.16}$$

Again we do not need to solve the coupled problem in eqs(5.9- 5.10). It is enough to substitute eq.(5.16) with $\theta = \boldsymbol{\Pi}^{\mathrm{T}}\boldsymbol{\varepsilon}$ into the rate form of eq.(5.11) and then eq. (5.11) into the rate form of eq.(5.9) to calculate the total stress as:

$$\boldsymbol{\sigma_t} = \boldsymbol{\sigma} + \boldsymbol{\Pi}\,\frac{K_f}{n}\theta. \tag{5.17}$$

and to see that we only have to modify the tangent stiffness obtained for the drained state according to:

$$\boldsymbol{D}^{\mathrm{u}} = \boldsymbol{D}^{\mathrm{d}} + \frac{K_f}{n}\boldsymbol{\Pi}\boldsymbol{\Pi}^{\mathrm{T}} \tag{5.18}$$

5.5 Linearization and discretization for two-phase medium

The governing equations in the analysis of the coupled deformation and fluid flow problem are derived from the mechanical equilibrium of the soil skeleton and the mass balance of the pore fluid. The unknown variables in the obtained system of equations are not only the solid displacements and fluid pore pressure but also their rates. The solution of such a system of equations requires the application of a stable and accurate time integration scheme.

5.5.1 Integration in time

The discretization in time is usually carried out using the generalized trapezoidal method (the Θ-method). With this method, all time dependent variables are estimated at some intermediate point with the interval depending on the chosen value of Θ. To assure the unconditional stability of the algorithm, the integration coefficient should satisfy the condition $\Theta \geq \frac{1}{2}$. This method and the problems of convergence, consistency and stability of the numerical algorithms (and various aspects of their analysis) are covered for instance in [27]. In the discussed implementation the backward Euler scheme with $\Theta = 1$ is used. The application of this integration method gives:

$$\boldsymbol{u}_{N+1} = \boldsymbol{u}_N + \Delta t \, \dot{\boldsymbol{u}}_N + \Theta \Delta t \Delta \dot{\boldsymbol{u}}_{N+1}, \tag{5.19}$$

$$p_{N+1} = p_N + \Delta t \, \dot{p}_N + \Theta \Delta t \Delta \dot{p}_{N+1} \tag{5.20}$$

5.5.2 Two-phase (fully saturated) medium, u-p element

In Sect. 5.2 the strong form of the coupled deformation and fluid flow problem for a fully saturated medium is described. For the finite element approach weak forms of momentum and mass balance equations are required. The pore pressure field is then discretized in addition to the displacements.

The weak format of the momentum balance reads:

$$\int_\Omega \boldsymbol{v}^{\mathrm{T}} (\boldsymbol{L}^{\mathrm{T}} \boldsymbol{\sigma}_t + \hat{\rho} \boldsymbol{g}) \, \mathrm{d}\Omega = \boldsymbol{0} \quad \forall \boldsymbol{v}. \tag{5.21}$$

The weak format of the mass balance is:

$$\int_\Omega w \left(\boldsymbol{\nabla} \cdot \dot{\boldsymbol{u}} + \boldsymbol{\nabla} \cdot \boldsymbol{v}_d + n \frac{\dot{p}_f}{K_f} \right) \, \mathrm{d}\Omega = 0 \quad \forall w. \tag{5.22}$$

In eqs.(5.21 - 5.22) $\boldsymbol{v}$ and $\boldsymbol{w}$ are suitable weighting functions. After integration by parts and using natural boundary conditions we obtain:

$$\int_\Omega (\boldsymbol{L}\boldsymbol{v})^{\mathrm{T}} \boldsymbol{\sigma}_t \, \mathrm{d}\Omega - \int_\Omega \boldsymbol{v}^{\mathrm{T}} \hat{\rho} \boldsymbol{g} \, \mathrm{d}\Omega - \int_{\Gamma_t} \boldsymbol{v}^{\mathrm{T}} \, \bar{\boldsymbol{t}} \, \mathrm{d}\Gamma = \boldsymbol{0}, \tag{5.23}$$

$$\int_{\Omega} w \boldsymbol{\nabla}^{\mathrm{T}} \dot{\boldsymbol{u}} \, \mathrm{d}\Omega - \int_{\Omega} (\boldsymbol{\nabla} w)^{\mathrm{T}} \boldsymbol{v}_d \, \mathrm{d}\Omega + \int_{\Omega} w \frac{n}{K_f} \dot{p}_f \, \mathrm{d}\Omega + \int_{\Gamma_q} w \, \bar{\boldsymbol{q}} \, \mathrm{d}\Gamma_q = 0. \tag{5.24}$$

Let us introduce the following finite element interpolation functions for the approximated fields:

$$\boldsymbol{u} = \boldsymbol{N} \, \bar{\boldsymbol{u}} \, , \quad p_f = \boldsymbol{N}_p \, \bar{\boldsymbol{p}} \, , \quad \boldsymbol{v} = \boldsymbol{N} \, \bar{\boldsymbol{v}} \, , \quad w = \boldsymbol{N}_p \, \bar{\boldsymbol{w}}, \tag{5.25}$$

where $\bar{\boldsymbol{u}}$ and $\bar{\boldsymbol{p}}$ are the nodal displacement and nodal pore pressure vectors, respectively. According to the Galerkin approach, the weighting functions are interpolated similarly. The used interpolation functions are quadratic for the displacements and linear for the pore pressure. The displacements are interpolated between eight nodes and excess pore pressure using four nodes, see Fig. 5.3. With above definitions and with assumption of linear kinematic relation $\boldsymbol{\varepsilon} = \boldsymbol{L}\boldsymbol{u}$, the discretization of strains can be expressed as:

$$\boldsymbol{\epsilon} = \boldsymbol{B}\bar{\boldsymbol{u}}, \tag{5.26}$$

where $\boldsymbol{B} = \boldsymbol{L}\boldsymbol{N}$. We also have $\boldsymbol{L}\boldsymbol{v} = \boldsymbol{B}\bar{\boldsymbol{v}}$.

Introducing the above expressions into eq. (5.23) we obtain the discretized equilibrium condition:

$$\int_{\Omega} \bar{\boldsymbol{v}}^{\mathrm{T}} \left(\boldsymbol{B}^{\mathrm{T}} \boldsymbol{\sigma} - \boldsymbol{B}^{\mathrm{T}} \boldsymbol{\Pi} \boldsymbol{N}_p \bar{\boldsymbol{p}} \right) \mathrm{d}\Omega - \int_{\Omega} \bar{\boldsymbol{v}}^{\mathrm{T}} \boldsymbol{N}^{\mathrm{T}} \hat{\rho} \boldsymbol{g} \mathrm{d}\Omega - \int_{\Gamma_t} \bar{\boldsymbol{v}}^{\mathrm{T}} \boldsymbol{N}^{\mathrm{T}} \bar{\boldsymbol{t}} \mathrm{d}\Gamma = \boldsymbol{0}. \tag{5.27}$$

It must be satisfied for any $\bar{\boldsymbol{v}}^{\mathrm{T}}$, so we obtain for the unknown time step $N+1$:

$$\int_{\Omega} \left(\boldsymbol{B}^{\mathrm{T}} \boldsymbol{\sigma}_{N+1} - \boldsymbol{B}^{\mathrm{T}} \boldsymbol{\Pi} \boldsymbol{N}_p \bar{\boldsymbol{p}}_{N+1} \right) \mathrm{d}\Omega = \boldsymbol{f}_{ext}, \tag{5.28}$$

where:

$$\boldsymbol{f}_{ext} = \int_{\Omega} \boldsymbol{N}^{\mathrm{T}} \hat{\rho}_{N+1} \boldsymbol{g} \mathrm{d}\Omega + \int_{\Gamma_t} \boldsymbol{N}^{\mathrm{T}} \bar{\boldsymbol{t}}_{N+1} \mathrm{d}\Gamma. \tag{5.29}$$

Incremental-iterative algorithm is used with the following decomposition:

$$\boldsymbol{\sigma}_{N+1}^{(i+1)} = \boldsymbol{\sigma}_{N+1}^{(i)} + \Delta \boldsymbol{\sigma}^{(i+1)}, \quad p_{N+1}^{(i+1)} = p_{N+1}^{(i)} + \Delta p^{(i+1)}, \tag{5.30}$$

where $\Delta\boldsymbol{\sigma}^{(i+1)}$ and $\Delta p^{(i+1)}$ denote iterative corrections of $\boldsymbol{\sigma}_{N+1}$ and p_{N+1} respectively, in iteration $(i+1)$. After linearization the relation (5.28) becomes:

$$\begin{aligned} \int_{\Omega} \boldsymbol{B}^{\mathrm{T}} \boldsymbol{D}_{N+1}^{ep(i)} \boldsymbol{B} \mathrm{d}\Omega \, \Delta \bar{\boldsymbol{u}}^{(i+1)} - \int_{\Omega} \boldsymbol{B}^{\mathrm{T}} \boldsymbol{\Pi} \boldsymbol{N}_p \mathrm{d}\Omega \, \Delta \bar{\boldsymbol{p}}^{(i+1)}, \\ = \boldsymbol{f}_{ext\,N+1} - \boldsymbol{f}_{int\,N+1} \end{aligned} \tag{5.31}$$

where

$$\boldsymbol{f}_{int\,N+1} = \int_\Omega \left(\boldsymbol{B}^\mathrm{T}\boldsymbol{\sigma}^{(i)}_{N+1} - \boldsymbol{B}^\mathrm{T}\boldsymbol{\Pi}\boldsymbol{N}_p\bar{\boldsymbol{p}}^{(i)}_{N+1} \right) \mathrm{d}\Omega. \tag{5.32}$$

The discretized weak form of the mass balance equation can be expressed as:

$$\begin{aligned} &\int_\Omega \bar{\boldsymbol{w}}^\mathrm{T}\boldsymbol{N}_p^\mathrm{T}\boldsymbol{\Pi}^\mathrm{T}\boldsymbol{B}\dot{\bar{\boldsymbol{u}}}\;\mathrm{d}\Omega - \int_\Omega \bar{\boldsymbol{w}}^\mathrm{T}\boldsymbol{\nabla}\boldsymbol{N}_p{}^\mathrm{T}\boldsymbol{v}_d\;\mathrm{d}\Omega \\ &+ \int_\Omega \bar{\boldsymbol{w}}^\mathrm{T}\boldsymbol{N}_p^\mathrm{T}\frac{n}{K_f}\boldsymbol{N}_p\dot{\bar{\boldsymbol{p}}}\;\mathrm{d}\Omega + \int_{\Gamma_q} \bar{\boldsymbol{w}}^\mathrm{T}\boldsymbol{N}_p^\mathrm{T}\bar{\boldsymbol{q}}\;\mathrm{d}\Gamma = \boldsymbol{0}. \end{aligned} \tag{5.33}$$

For any $\bar{\boldsymbol{w}}^\mathrm{T} \neq \boldsymbol{0}$, and introducing Darcy's law (5.13), we obtain for the current time step:

$$\begin{aligned} &\int_\Omega \boldsymbol{N}_p^\mathrm{T}\boldsymbol{\Pi}^\mathrm{T}\boldsymbol{B}\mathrm{d}\Omega\;\dot{\bar{\boldsymbol{u}}}_{N+1} + \frac{1}{\gamma_f}\int_\Omega (\boldsymbol{\nabla}\boldsymbol{N}_p)^\mathrm{T}\boldsymbol{k}\boldsymbol{\nabla}\boldsymbol{N}_p\mathrm{d}\Omega\;\bar{\boldsymbol{p}}_{N+1} \\ &+ \int_\Omega \boldsymbol{N}_p^\mathrm{T}\frac{n}{K_f}\boldsymbol{N}_p\mathrm{d}\Omega\;\dot{\bar{\boldsymbol{p}}}_{N+1} = -\int_{\Gamma_q} (\boldsymbol{N}_p)^\mathrm{T}\bar{\boldsymbol{q}}_{N+1}\mathrm{d}\Gamma \end{aligned}$$

After linearization we have:

$$\begin{aligned} &\int_\Omega \boldsymbol{N}_p^\mathrm{T}\boldsymbol{\Pi}^\mathrm{T}\boldsymbol{B}\mathrm{d}\Omega\;\Delta\dot{\bar{\boldsymbol{u}}}^{(i+1)} + \frac{1}{\gamma_f}\int_\Omega (\boldsymbol{\nabla}\boldsymbol{N}_p)^\mathrm{T}\boldsymbol{k}\boldsymbol{\nabla}\boldsymbol{N}_p\mathrm{d}\Omega\;\Delta\bar{\boldsymbol{p}}^{(i+1)} \\ &+ \int_\Omega \boldsymbol{N}_p^\mathrm{T}\frac{n}{K_f}\boldsymbol{N}_p\mathrm{d}\Omega\;\Delta\dot{\bar{\boldsymbol{p}}}^{(i+1)} = -\int_{\Gamma_q} (\boldsymbol{N}_p)^\mathrm{T}\bar{\boldsymbol{q}}_{N+1}\mathrm{d}\Gamma - \int_\Omega \boldsymbol{N}_p^\mathrm{T}\boldsymbol{\Pi}^\mathrm{T}\boldsymbol{B}\mathrm{d}\Omega\;\dot{\bar{\boldsymbol{u}}}^{(i)}_{N+1} \\ &-\frac{1}{\gamma_f}\int_\Omega (\boldsymbol{\nabla}\boldsymbol{N}_p)^\mathrm{T}\boldsymbol{k}\boldsymbol{\nabla}\boldsymbol{N}_p\mathrm{d}\Omega\;\bar{\boldsymbol{p}}^{(i)}_{N+1} - \int_\Omega \boldsymbol{N}_p^\mathrm{T}\frac{n}{K_f}\boldsymbol{N}_p\mathrm{d}\Omega\;\dot{\bar{\boldsymbol{p}}}^{(i)}_{N+1}. \end{aligned} \tag{5.34}$$

Applying the time integration scheme introduced in Sect. 5.5.1, we eventually obtain:

$$\begin{aligned} &\int_\Omega \boldsymbol{N}_p^\mathrm{T}\boldsymbol{\Pi}^\mathrm{T}\boldsymbol{B}\;\mathrm{d}\Omega\;\Delta\bar{\boldsymbol{u}}^{(i+1)} \\ &+ \left(\frac{\Delta t}{\gamma_f}\int_\Omega (\boldsymbol{\nabla}\boldsymbol{N}_p)^\mathrm{T}\boldsymbol{k}\boldsymbol{\nabla}\boldsymbol{N}_p\;\mathrm{d}\Omega + \int_\Omega \boldsymbol{N}_p^\mathrm{T}\frac{n}{K_f}\boldsymbol{N}_p\;\mathrm{d}\Omega \right)\Delta\bar{\boldsymbol{p}}^{(i+1)} = \\ &\Delta t\left(-\int_{\Gamma_q} (\boldsymbol{N}_p)^\mathrm{T}\bar{\boldsymbol{q}}_{N+1}\;\mathrm{d}\Gamma - \int_\Omega \boldsymbol{N}_p^\mathrm{T}\boldsymbol{\Pi}^\mathrm{T}\boldsymbol{B}\;\mathrm{d}\Omega\;\dot{\bar{\boldsymbol{u}}}^{(i)}_{N+1} \right. \\ &\left. -\frac{1}{\gamma_f}\int_\Omega (\boldsymbol{\nabla}\boldsymbol{N}_p)^\mathrm{T}\boldsymbol{k}\boldsymbol{\nabla}\boldsymbol{N}_p\;\mathrm{d}\Omega\;\bar{\boldsymbol{p}}^{(i)}_{N+1} - \int_\Omega \boldsymbol{N}_p^\mathrm{T}\frac{n}{K_f}\boldsymbol{N}_p\;\mathrm{d}\Omega\;\dot{\bar{\boldsymbol{p}}}^{(i)}_{N+1} \right). \end{aligned}$$

Let us rewrite the obtained coupled system of linearized equations in a matrix form:

$$\begin{bmatrix} \boldsymbol{K}^{(i)}_{N+1} & -\boldsymbol{C} \\ \boldsymbol{C}^\mathrm{T} & \left(\frac{\Delta t}{\gamma_f}\boldsymbol{H} + \boldsymbol{M}\right) \end{bmatrix} \begin{bmatrix} \Delta\bar{\boldsymbol{u}}^{(i+1)} \\ \Delta\bar{\boldsymbol{p}}^{(i+1)} \end{bmatrix} = \begin{bmatrix} \boldsymbol{f}_{ext\,N+1} - \boldsymbol{f}^{(i)}_{int\,N+1} \\ \boldsymbol{f}^{(i)}_{f\,N+1} \end{bmatrix} \tag{5.35}$$

where:

$$\boldsymbol{K}_{N+1}^{(i)} = \int_\Omega \boldsymbol{B}^{\mathrm{T}} \boldsymbol{D}_{N+1}^{ep(i)} \boldsymbol{B} \mathrm{d}\Omega, \tag{5.36}$$

$$\boldsymbol{C} = \int_\Omega \boldsymbol{B}^{\mathrm{T}} \boldsymbol{\Pi} \boldsymbol{N}_p \mathrm{d}\Omega, \tag{5.37}$$

$$\boldsymbol{H} = \int_\Omega (\boldsymbol{\nabla} \boldsymbol{N}_p)^{\mathrm{T}} \boldsymbol{k} \boldsymbol{\nabla} \boldsymbol{N}_p \mathrm{d}\Omega, \tag{5.38}$$

$$\boldsymbol{M} = \int_\Omega \boldsymbol{N}_p^{\mathrm{T}} \frac{n}{K_f} \boldsymbol{N}_p \mathrm{d}\Omega, \tag{5.39}$$

$$\boldsymbol{f}_f = \Delta t \left(- \int_{\Gamma_q} (\boldsymbol{N}_p)^{\mathrm{T}} \bar{\boldsymbol{q}}_{N+1} \mathrm{d}\Gamma - \boldsymbol{C}^{\mathrm{T}} \dot{\bar{\boldsymbol{u}}}_{N+1}^{(i)} - \frac{1}{\gamma_f} \boldsymbol{H} \bar{\boldsymbol{p}}_{N+1}^{(i)} - \boldsymbol{M} \dot{\bar{\boldsymbol{p}}}_{N+1}^{(i)} \right).$$

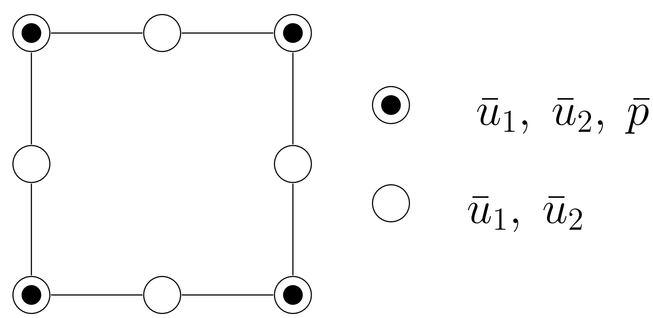

Figure 5.3: Two-phase u-p element

Applying the derivations shown above to equations (5.1) and (5.2) we can obtain a similar set of linear equations for partially saturated soil [73].

5.6 One-element undrained tests

Now, the simple one-element tests described in Sect. 4.6 are repeated for the undrained state. The additional material data for the undrained conditions is $K_f = 10.0$ MPa. The results for the drained and undrained analysis are compared for the biaxial and triaxial compression test. The triaxial compression test for the undrained state is then repeated for non-associative plasticity. The results for undrained shear are also included.

5.6.1 Drained/undrained biaxial compression

The results for the drained and undrained analyses are compared for the biaxial compression test with slightly and heavily preconsolidated soil. For the drained state excess pore pressure $p_F = 0$. For the undrained state the pore pressure is proportional to the change of solid skeleton volume and evolves according to eq. (5.16). The effective stress can be obtained from eq. (5.17). In Fig. 5.4 and in Fig. 5.6 the difference between the total and effective stress is shown. The soil strength is lower in undrained than in drained conditions because of the generated pore pressures. The influence of the vertical strain on the volume changes and excess pore pressure is also presented. For the case of dilatation due to large preconsolidation, the volume increase induces the negative excess pore pressure and the final value of effective vertical stress is higher than the one of the total stress. In Fig. 5.5 and in Fig. 5.7 the stress paths and the yield surfaces evolution for the drained and undrained analysis are compared. In both considered cases, the critical state line is reached earlier for the undrained state. However, for strongly overconsolidated soil the final value of p_c is larger for the undrained state. For a strongly overconsolidated soil, the presence of the fluid phase generates a cohesive effect resulting in a larger residual load level.

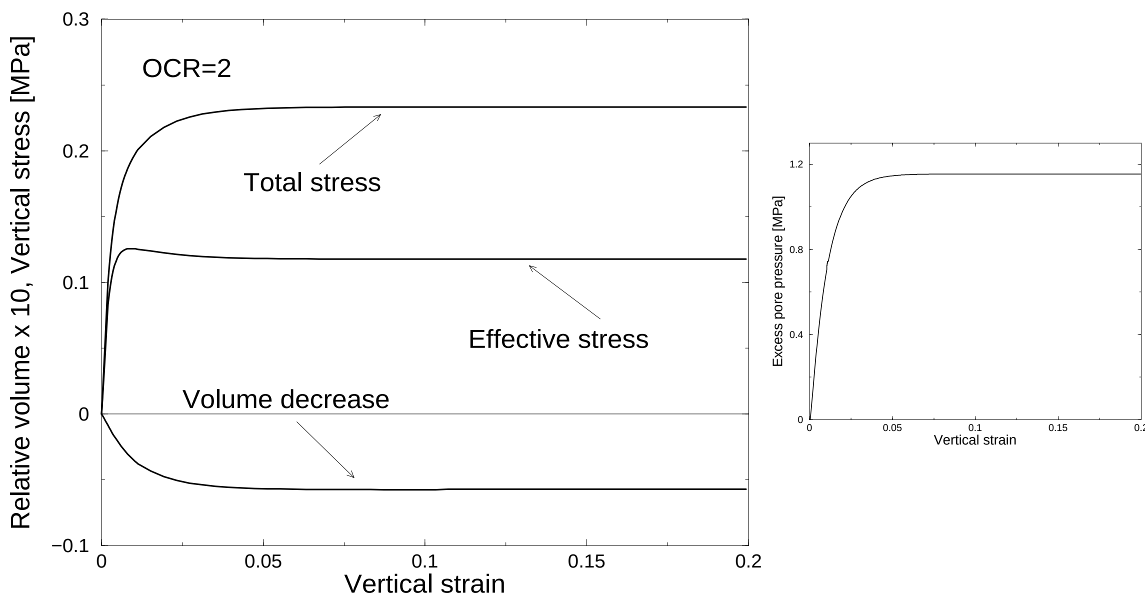

Figure 5.4: Stress-strain diagram for the vertical direction, relative volume and excess pore pressure evolution for slightly preconsolidated soil and undrained state (biaxial compression)

5.6.2 Drained/undrained triaxial compression

The comparison of the results obtained in a triaxial compression test for the limiting cases of the drained and undrained conditions is also performed. The normally consolidated and strongly preconsolidated soil is taken into account. In Fig. 5.8 and in Fig. 5.10 the volume changes, the excess pore pressure, total and effective stress is shown in relation to the

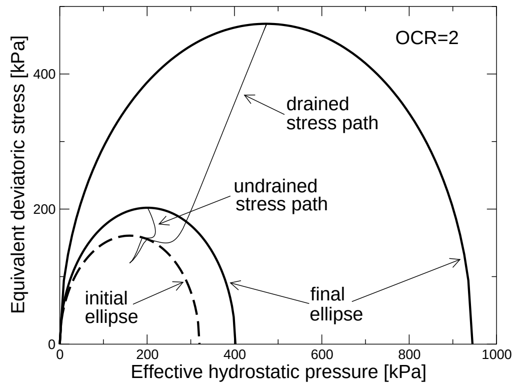

Figure 5.5: Yield surface evolution for slightly preconsolidated soil; comparison of drained and undrained state (biaxial compression)

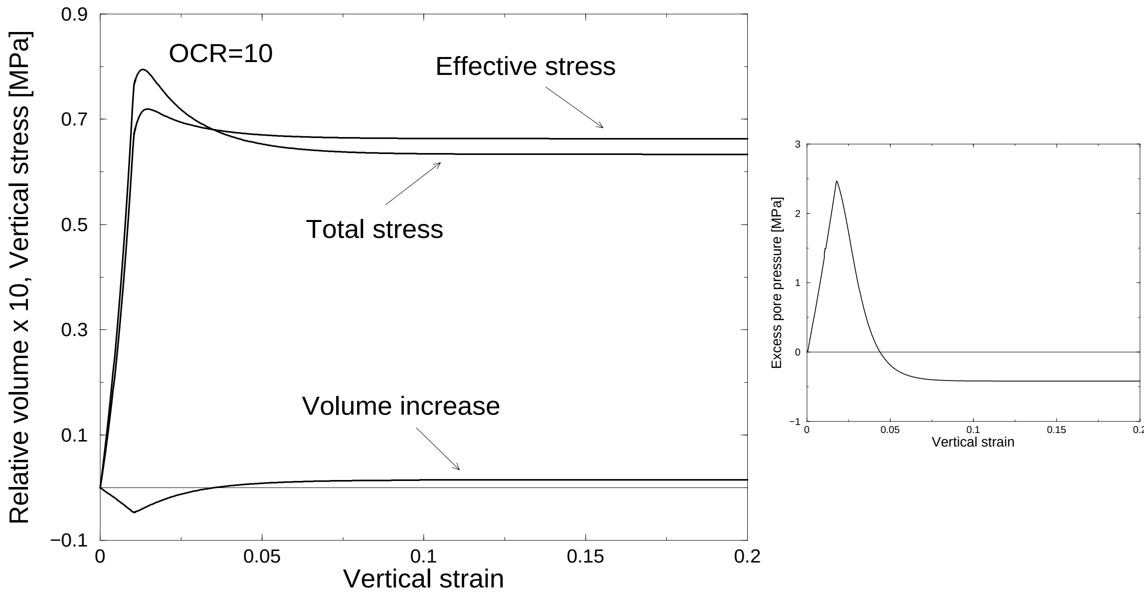

Figure 5.6: Stress-strain diagram for the vertical direction, relative volume and excess pore pressure evolution for strongly preconsolidated soil and undrained state (biaxial compression)

vertical strain. In Fig. 5.9 and in Fig. 5.11 the stress paths and yield surfaces evolution are presented. Similar observations can be made to those presented in the previous section can be made. The stress path reaches the critical state earlier in case of the undrained conditions, both for contractant and dilatant soil. Analysing the stress paths for the normally consolidated soil, we can notice that it turns left during the plastic process which results in the ’softening’ in the diagram of the effective stress. However, generally contraction and hardening is observed. On the contrary, in the case of preconsolidated material, when the yield surface is reached, the stress path turns right. The effective stress diagram does not exhibit the softening behaviour of the soil.

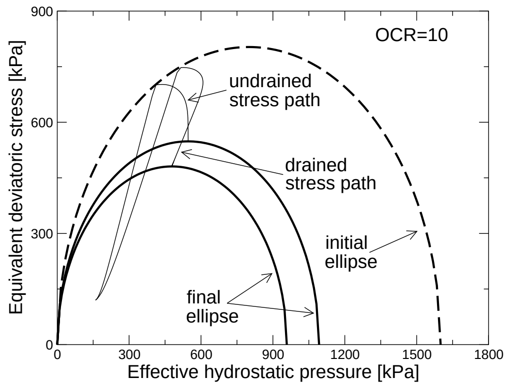

Figure 5.7: Yield surface evolution for strongly preconsolidated soil; comparison of drained and undrained state (biaxial compression)

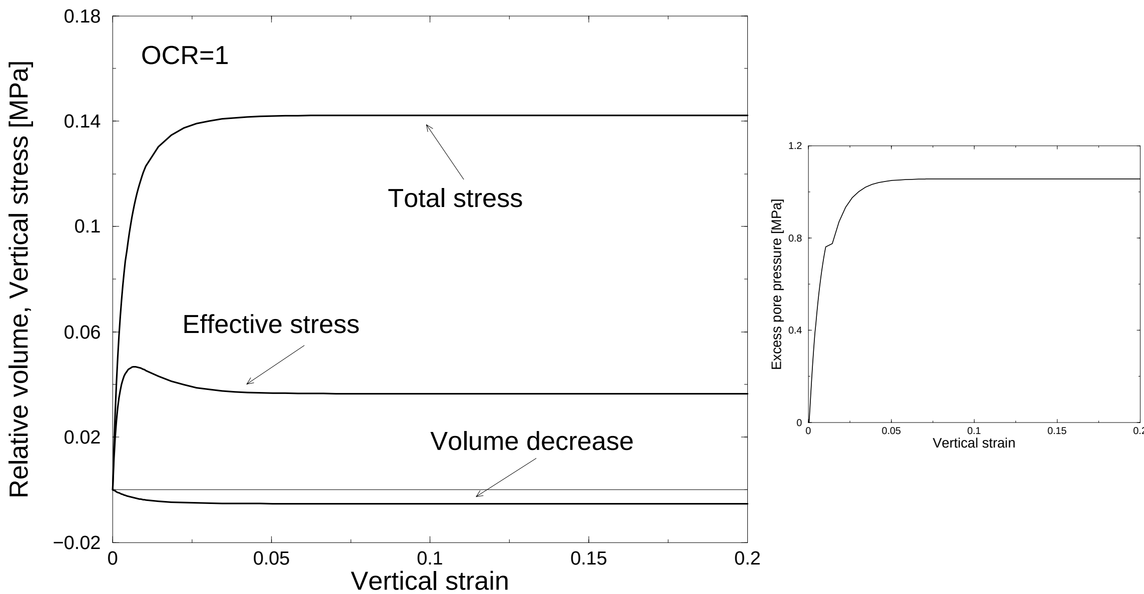

Figure 5.8: Stress-strain diagram for the vertical direction, relative volume and excess pore pressure evolution for normally consolidated soil and undrained state (triaxial compression)

5.6.3 Undrained triaxial compression - non-associated plasticity

One-element triaxial-compression test is now reconsidered for a one-phase medium under undrained conditions and different values of ratio $M/\bar{M}$. The presented test was described in [72]. The following material data are adopted: $\nu = 0.3$, $K_f = 1.0e10$ kPa (almost incompressible fluid), $\kappa = 0.01$, $e_0 = 1.0$, $p_c = 200$ kPa, $\lambda = 0.05$, $\bar{M} = 1.2$ and $M = 1.2; 1.0; 0.8; 0.6$.

The initial stresses $\boldsymbol{\sigma}_0 = [-200, -200, -200, 0.0]$ kPa is generated. The compression process is driven under displacement control. The vertical displacement of the nodes on the top

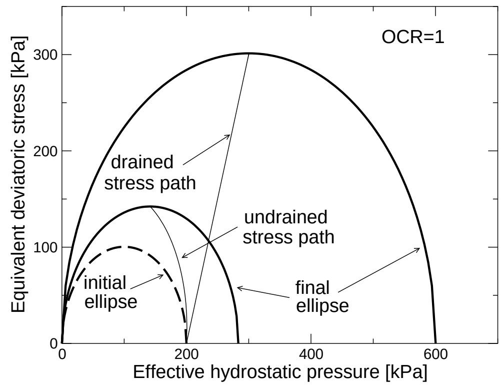

Figure 5.9: Yield surface evolution for normally consolidated soil; comparison of drained and undrained state (triaxial compression)

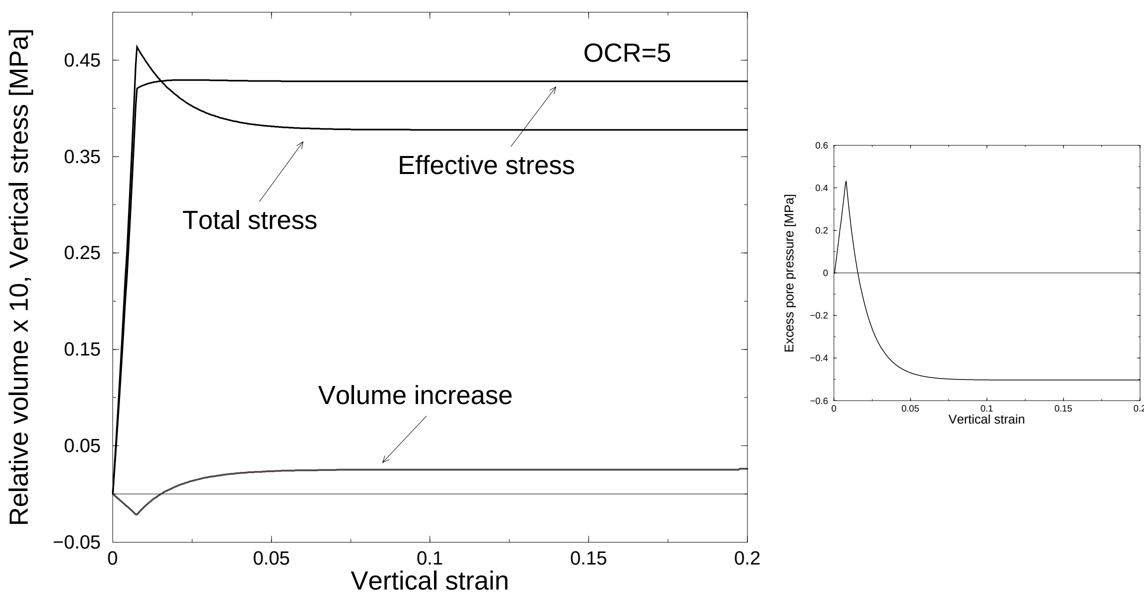

Figure 5.10: Stress-strain diagram for the vertical direction, relative volume and excess pore pressure evolution for strongly preconsolidated soil and undrained state (triaxial compression)

edge is prescribed. In Fig. 5.12 the results of calculations are presented. The inclination of the CSL is now defined by $\bar{M}$ and point (p,q) in the critical state is not the 'top point' of the yield surface (for $M \neq \bar{M}$). For increasing non-associativity the strength of material decreases.

5.6.4 Drained/undrained shear

At last the results for undrained shear test are included. Again the behaviour of slightly and heavily preconsolidated soil under drained and undrained conditions are compared. In

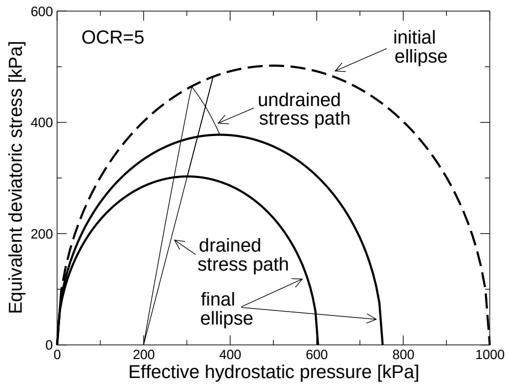

Figure 5.11: Yield surface evolution for strongly preconsolidated soil; comparison of drained and undrained state (triaxial compression)

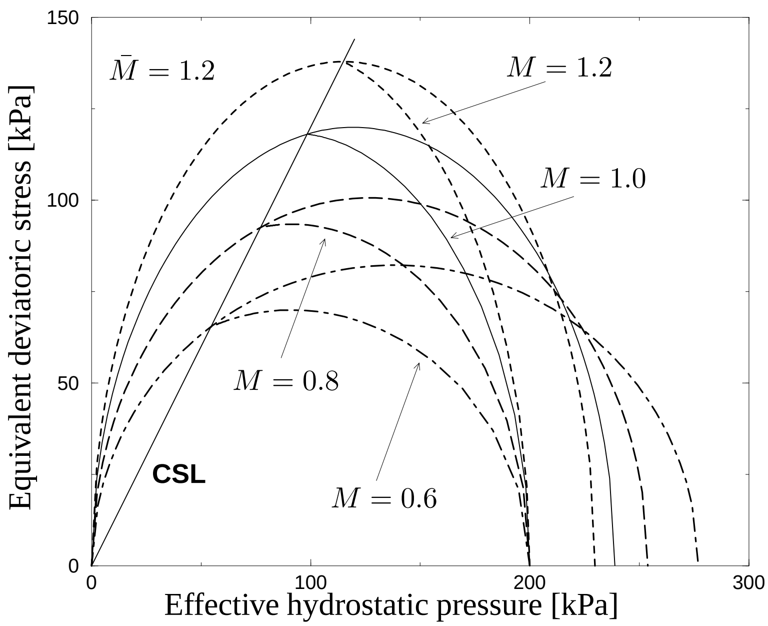

Figure 5.12: Finall yield surfaces and loading paths for $\bar{M} = 1.2$ and various values of M for undrained triaxial compression test

Fig. 5.13 and in Fig. 5.15 the volume changes, the excess pore pressure, and shear stress is shown in relation to the vertical strain. Note that the shear stress is not affected by pore pressure evolution so there is no difference between the total and effective (shear) stress. In Fig. 5.14 and in Fig. 5.16 the stress paths and yield surfaces evolution are presented. Like in the previously presented tests, the slightly preconsolidated soil contracts and heavily preconsolidated one dilates. The stress path reaches the critical state earlier in case of the undrained conditions, both for contractant and dilatant soil.

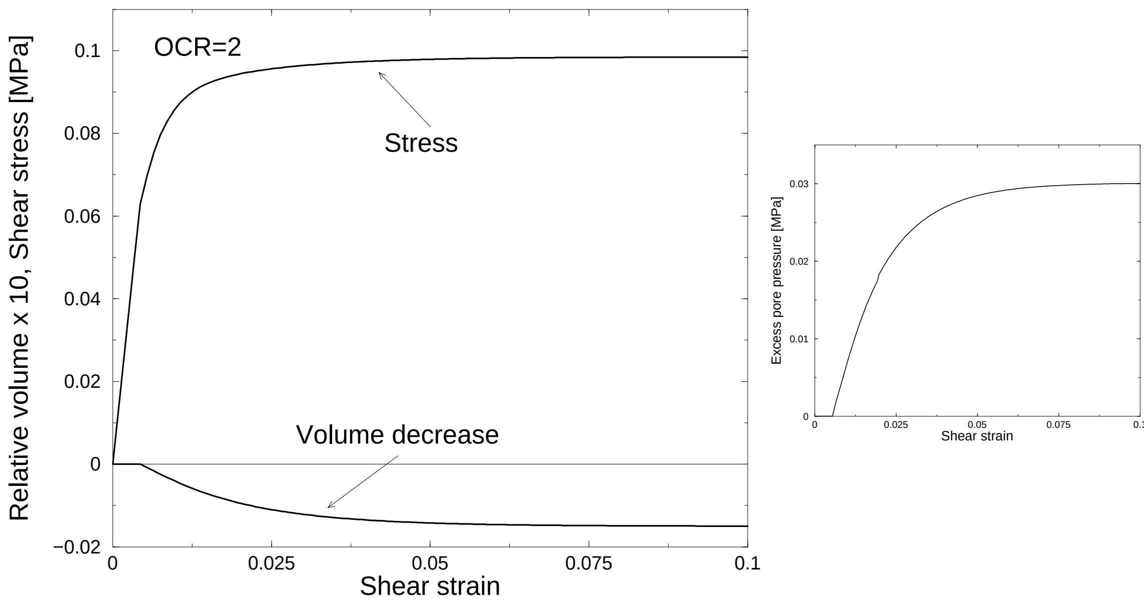

Figure 5.13: Stress-strain diagram for the vertical direction, relative volume and excess pore pressure evolution for slightly preconsolidated soil and undrained state (pure shear)

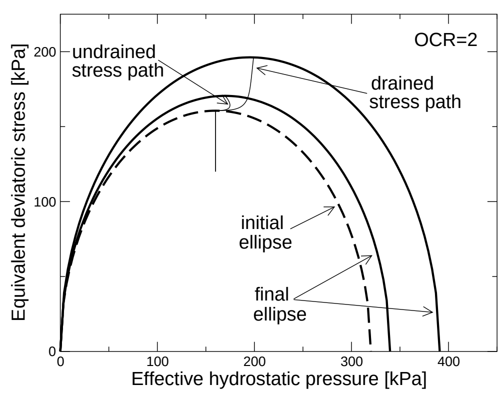

Figure 5.14: Yield surface evolution for slightly preconsolidated soil; comparison of drained and undrained state (pure shear)

5.7 Simple two-phase tests

The following simple tests are performed in order to verify the numerical implementation of the finite element described in Sect. 5.5.2. The calculations are repeated after [73].

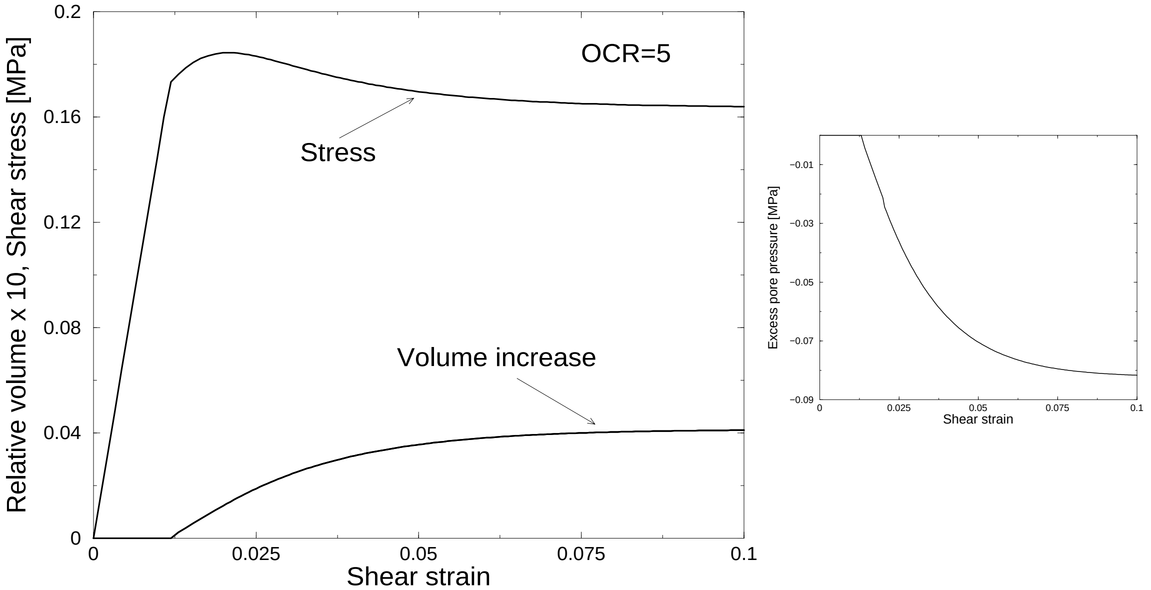

Figure 5.15: Stress-strain diagram for the vertical direction, relative volume and excess pore pressure evolution for strongly preconsolidated soil and undrained state (pure shear)

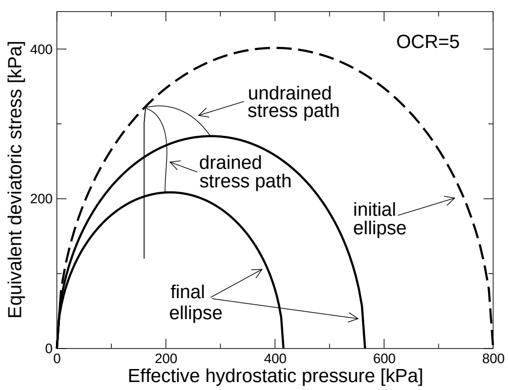

Figure 5.16: Yield surface evolution for strongly preconsolidated soil; comparison of drained and undrained state (pure shear)

5.7.1 Uniaxial consolidation - one element test

This example shows the results for a simple one element test which is used to verify the performance of the implemented numerical algorithm for the two-phase medium. The boundary conditions and loading function are depicted in Fig. 5.17. The specimen is loaded by vertical traction along the upper edge. The condition $q = 0$ means that the boundary is impermeable. Water can flow out of the sample only through the part of the boundary where $p_f = 0$.

The computations are carried out using the two-phase linear elastic and elasto-plastic

Cam-clay model for a fully saturated medium. The following material data are adopted: $E = 1.0e04$ kPa, $\nu = 0.3$, $\gamma_f = 10$ kN/m^3, $K_f = 1.0e08$ kPa, $k = 1.0$ e-03 m/day for the elastic model and additionally $\kappa = 0.013$, $e_0 = 1.0$, $p_c = 0.3$ kPa, $\lambda = 0.032$, $M = 1.1$, $K_f = 1.0e05$ kPa, $k = 1.0$ m/day for the Cam-clay model.

In Fig. 5.18 the dependence of pore pressure p_f on time is shown. As expected, the pore pressure increases at the beginning of the loading process (with growing loading) and then, because the pore fluid flows out, it decreases to zero.

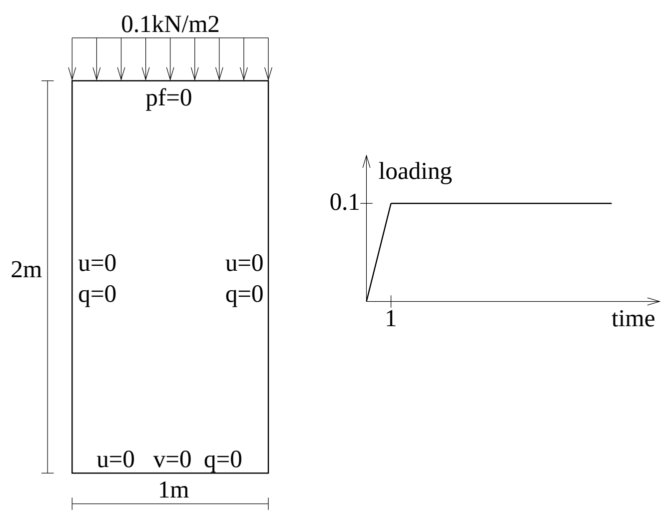

Figure 5.17: Consolidation test: geometry, static and kinematic boundary conditions

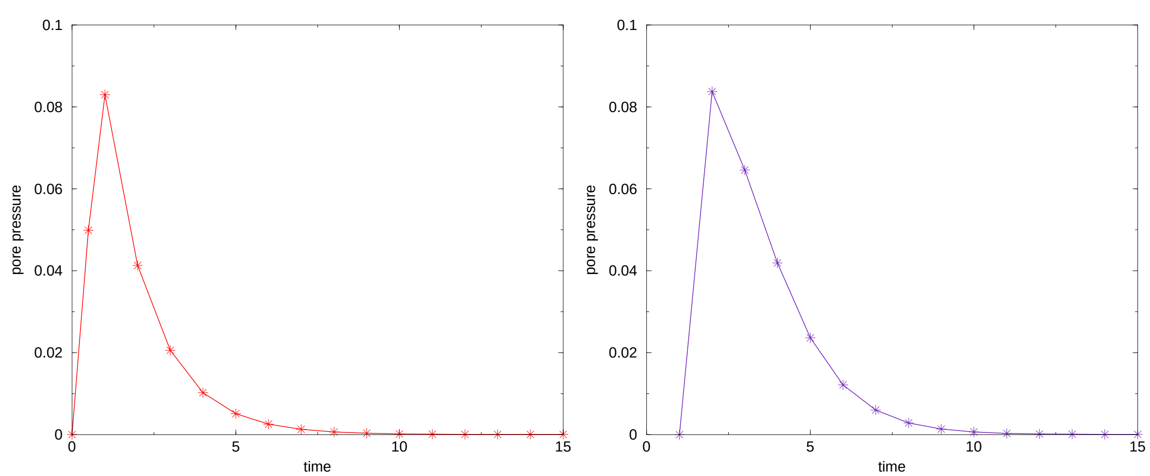

Figure 5.18: Dependence of pore pressure on time for linear elasticity (left) and for Cam-clay model (right)

5.7.2 Uniaxial consolidation - soil column

A similar problem as the previous one is analyzed for a multi-element configuration. The specimen of size 1m $\times$ 10m is discretized with 10 elements. The boundary conditions and loading function are similar as for the one element test and are shown in Fig. 5.19.
The computations are performed using the linear elastic and elasto-plastic Cam-clay model for the fully saturated two-phase medium. The following material data are adopted for linear elastic model: $E = 1.0e04$ kPa, $\nu = 0.3$, $\gamma_f = 10$ kN/m^3, $K_f = 1.0e08$ kPa, $k = 1.0$ e-02 m/day, and for Cam-clay model $\kappa = 0.013$, $e_0 = 1.0$, $p_c = 0.3$kPa, $\lambda = 0.032$, $M = 1.1$, $K_f = 1.0e05$ kPa, $k = 1.0$ m/day.

In Fig. 5.20 the dependence of the pore pressure on the time and *y* coordinate (height) is shown. In Fig. 5.21 and Fig. 5.22 the distribution of the pore pressure along the vertical axis for some time steps is presented, cf. [86].

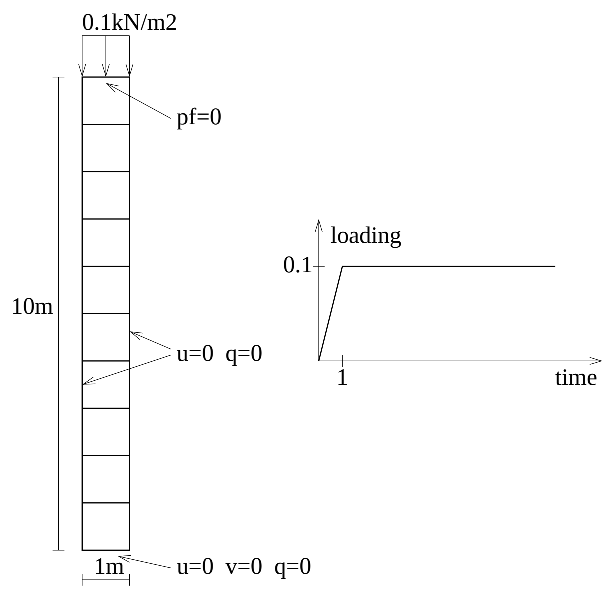

Figure 5.19: Consolidation test: geometry, static and kinematic boundary conditions

5.8 Localization in biaxial compression in two-phase medium

One of the major goals of the thesis is to examine the influence of the fluid phase on instabilities in the Cam-clay soil model. As mentioned in the introduction, it is claimed that the fluid phase can introduce some regularization into the numerical model. Therefore, the biaxial compression test presented in Sect. 4.7 is now repeated for a two-phase medium. For

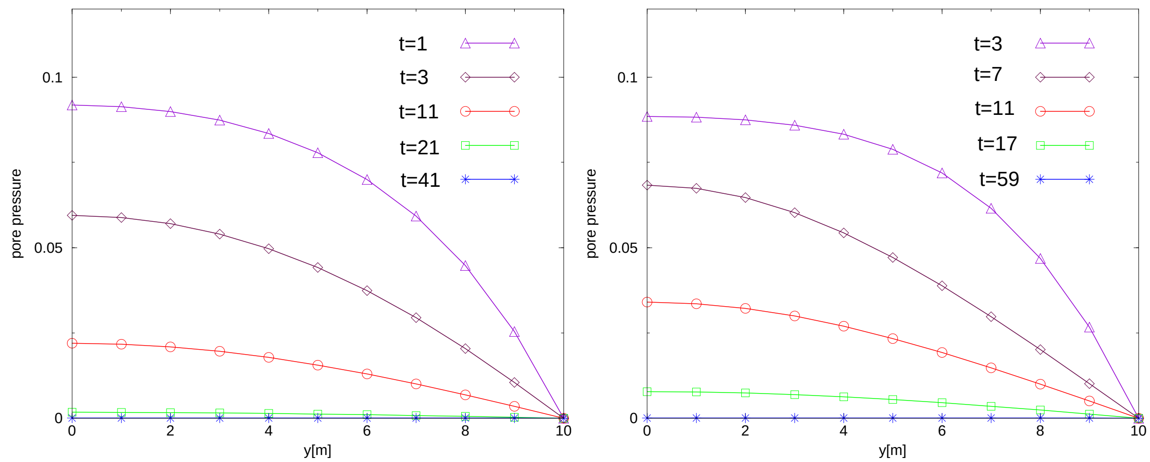

Figure 5.20: Dependence of pore pressure on time and y coordinate for linear elasticity (left) and for Cam-clay model (right)

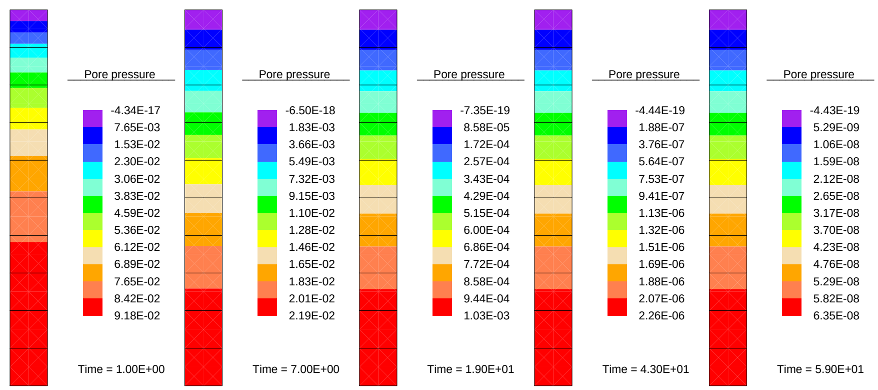

Figure 5.21: Pore pressure distribution - linear elasticity

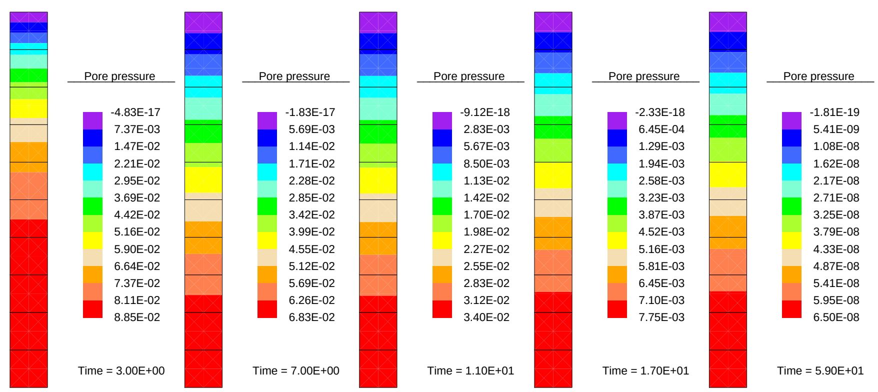

Figure 5.22: Pore pressure distribution - Cam-clay model

the fluid phase the additional material data are taken: $\gamma_f = 10$ kN/m^3, $K_f = 1.0e05$ kPa, $k = 1.0$ e-06 m/day. At first, the boundary conditions are such that fluid cannot flow out of the sample (homogeneous natural boundary condition). The initial excess pore pressure is

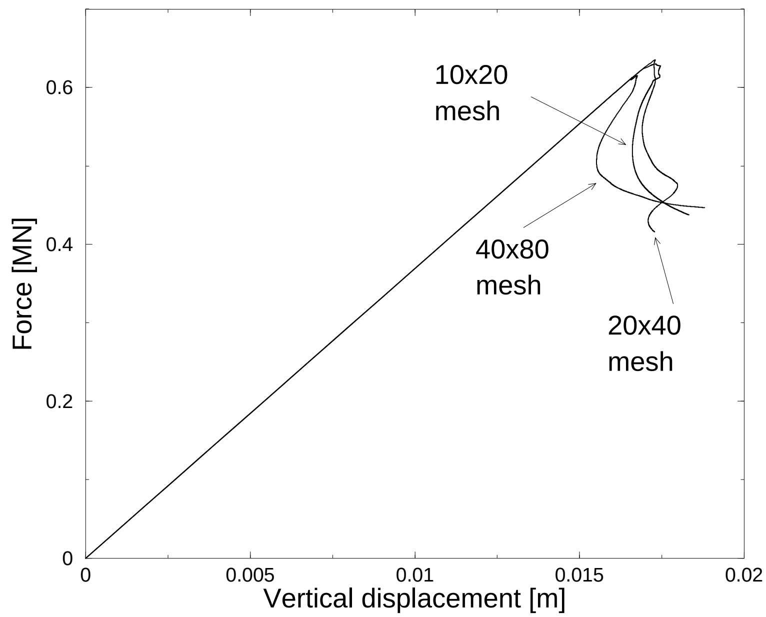

Figure 5.23: Load-deformation curves for $k = 1.0$ e-06 m/day (biaxial compression test for local Cam-clay model)

equal to zero.

As can be seen in Figs 5.23-5.25 the numerical results are not mesh-independent in this case. For the fine mesh the calculations were not completed due to convergence problems. Note that the contour plots for the second invariant of the strain tensor would look similarly to those of the vertical strain presented in Fig. 5.24. However, the pore pressure distribution shown in Fig. 5.25 does not exhibit localization in the narrowest zone, and in this respect it is similar for all the three meshes. At the same time, in Fig. 5.23 a distinct snap-back is visible in the load-deformation curve (sometimes even two snap-backs are simulated). This fact and the problems with convergence during calculations suggest that in comparison to the one-phase medium the two phase material is less stable.

In order to avoid the numerical difficulties and snap-backs the calculations are then repeated for $p_{c0} = 1.0$ MPa ($p_{c0} = 0.9$ MPa for the imperfect region in the bottom left-hand corner of the sample). The results for this data set (for two meshes) are presented in Figs 5.26-5.27. The diagrams in Fig. 5.26 are different for coarse and fine meshes, the vertical strain distribution (Fig. 5.27 left) shows the shear bands dependent on the adopted discretization, but the pore pressure distribution in Fig. 5.27 (right) seems to be nearly mesh-independent. The range of values in the contour plots are not given but can be found in [68].

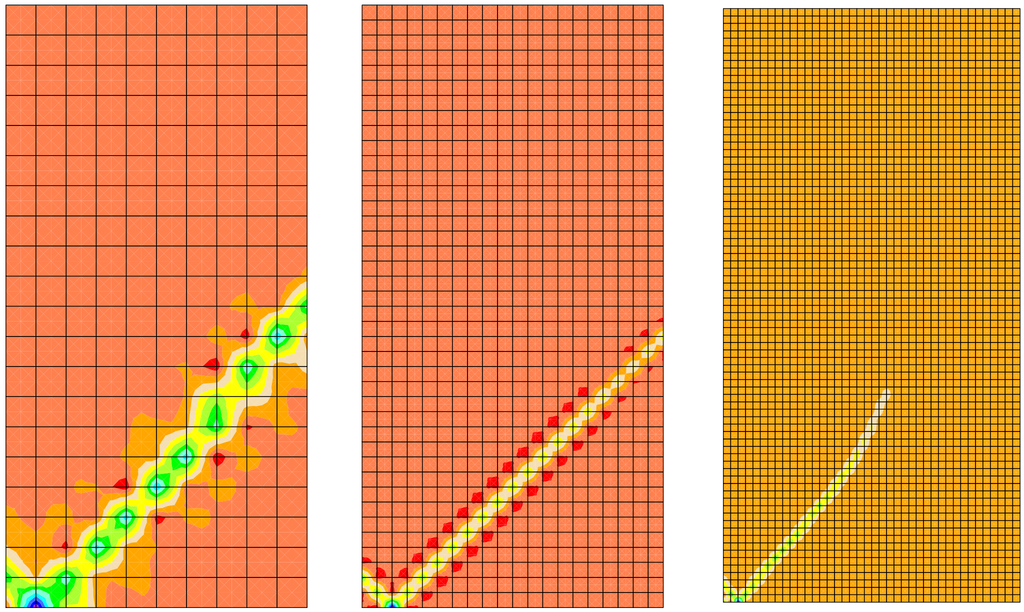

Figure 5.24: Vertical strain distribution for k = 1.0 e-06 m/day (biaxial compression test for local Cam-clay model)

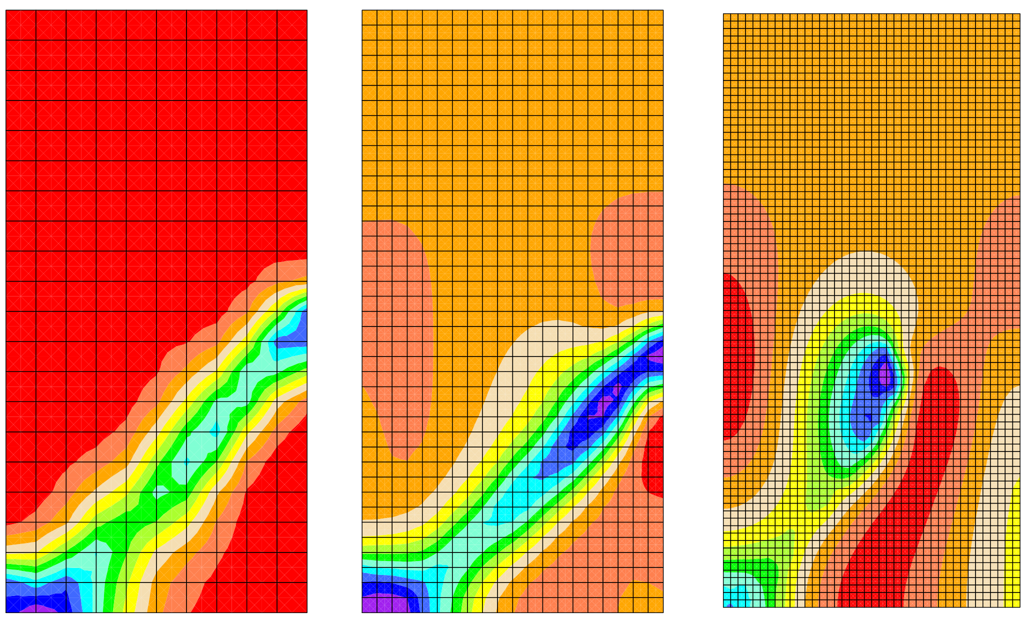

Figure 5.25: Pore pressure distribution for k = 1.0 e-06 m/day (biaxial compression test for local Cam-clay model)

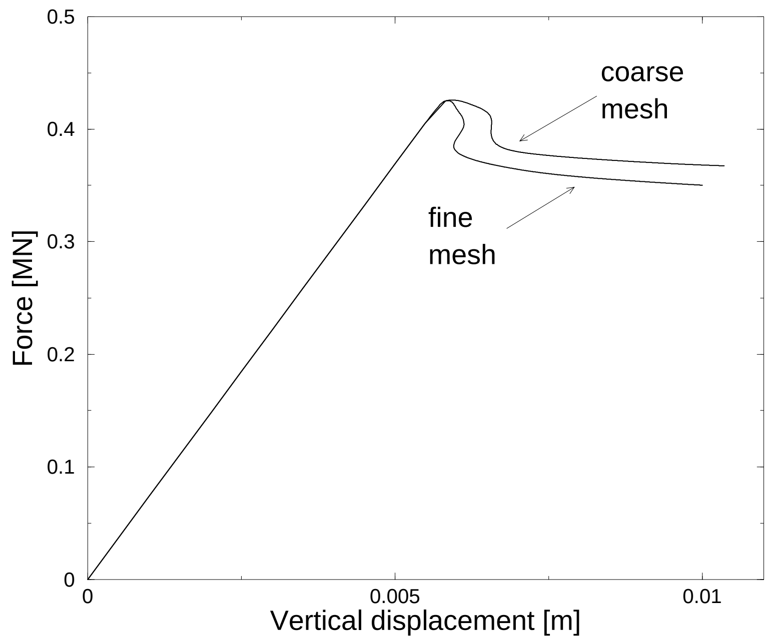

Figure 5.26: Load-deformation curves for $k = 1.0$ e-06 m/day and $p_{c0} = 1.0$MPa (biaxial compression test for local Cam-clay model)

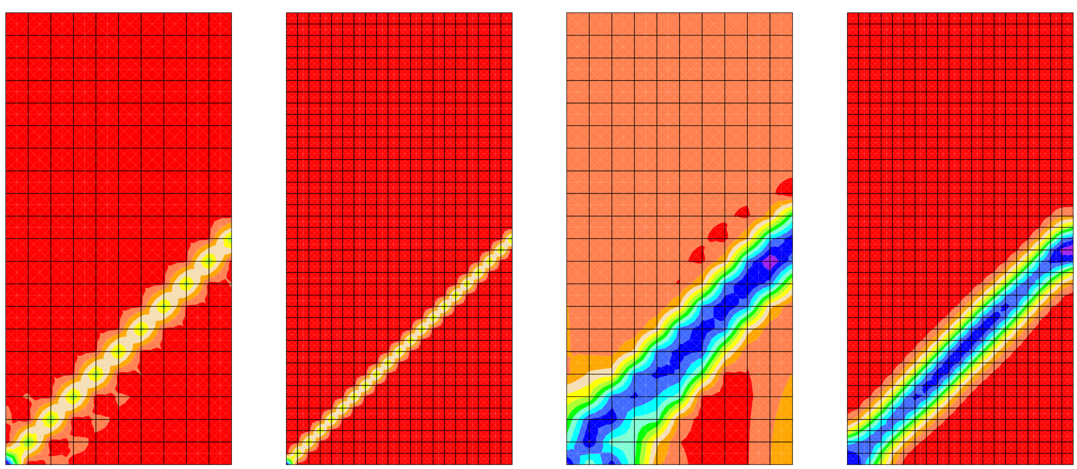

Figure 5.27: Vertical strain (left) and pore pressure (right) distribution for $k = 1.0$ e-06 m/day and $p_{c0} = 1.0$MPa (biaxial compression test for local Cam-clay model)

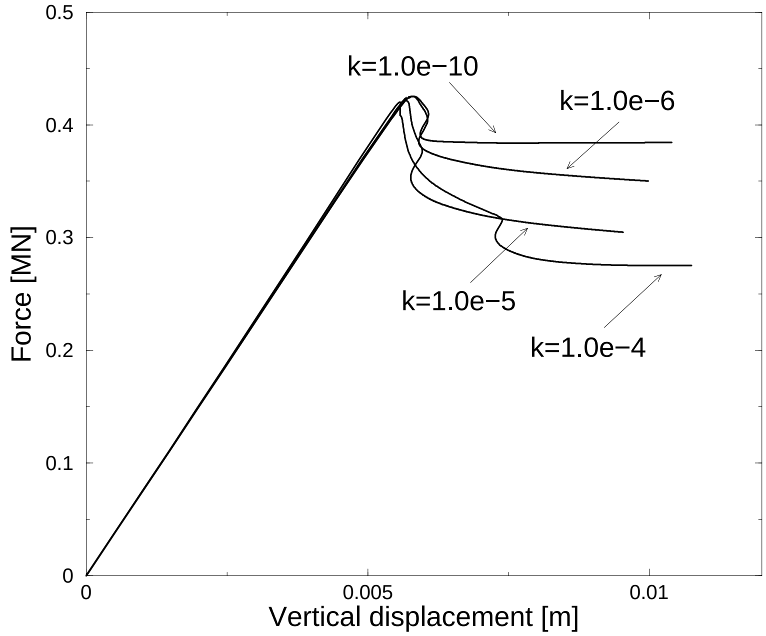

Figure 5.28: Load-deformation curves for different values of permeability coefficient and permeable upper edge (local Cam-clay model)

5.9 Influence of permeability coefficient in biaxial compression

In order to examine the role of permeability coefficient k in the regularization effect of the fluid, the calculations for various values of k ($k = 1.0$ e-04 m/day, $k = 1.0$ e-05 m/day, $k = 1.0$ e-06 m/day, $k = 1.0$ e-10 m/day) and for a permeable top edge have been performed. The obtained contour plots for the vertical strain turned out to be mesh-dependent. Irrespectively of the value of k the strains localize in the narrowest possible area determined by the element size. The selected results (for one mesh only) are presented in Figs 5.28-5.30. On the other hand, the value of the permeability coefficient influences the direction of the localization band (cf. Fig. 5.29) and the critical load level for which the instability occurs (cf. Fig. 5.28). Moreover, for the case of permeable top edge, the pore pressure distribution depends strongly on the value of permeability coefficient, cf. Fig. 5.30. For large permeability no localized pore pressure pattern is found.

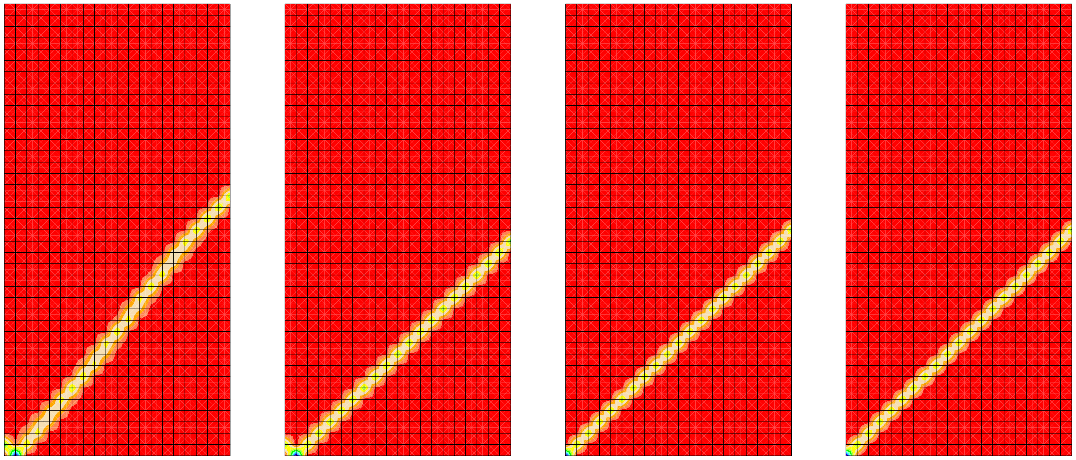

Figure 5.29: Vertical strain distribution for different values of permeability coefficient: $k = 1.0$ e-04 m/day, $k = 1.0$ e-05 m/day, $k = 1.0$ e-06 m/day, $k = 1.0$ e-10 m/day, from left to right (local Cam-clay model)

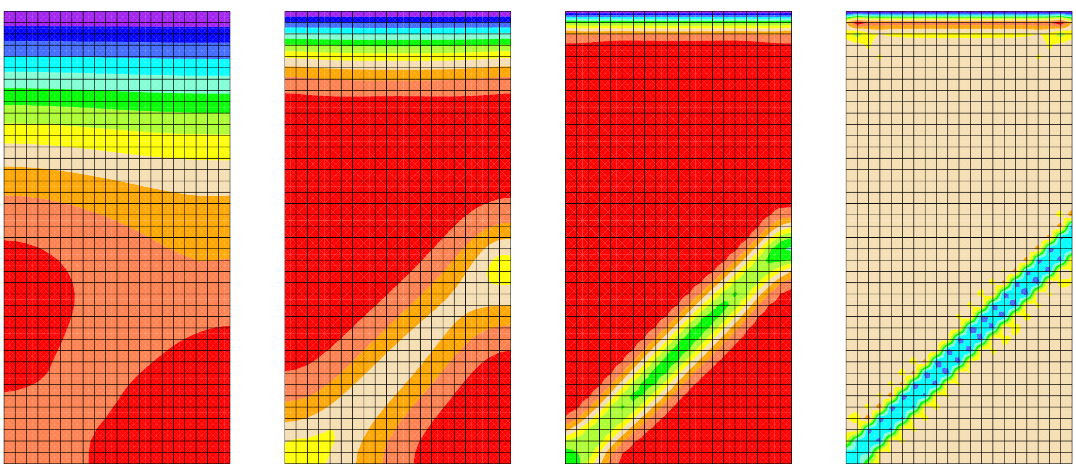

Figure 5.30: Pore pressure distribution for different values of permeability coefficient: $k = 1.0$ e-04 m/day, $k = 1.0$ e-05 m/day, $k = 1.0$ e-06 m/day, $k = 1.0$ e-10 m/day, from left to right (local Cam-clay model)

Chapter 6

Regularization

The dilatant (softening) and possibly also non-associative response of the Cam-clay model implies the necessity of regularization in order to avoid the loss of ellipticity of the governing equations and to stabilize the numerical response. Although alternative regularization methods could prove equally effective or simpler in terms of implementation, cf. [8], a gradient enhancement of the model is employed in this thesis.

6.1 Gradient enhancement of the Cam-clay yield function

In general, higher-order spatial gradients of different components of the constitutive model can be incorporated. If isotropy is assumed, the Laplacian is an optimal regularizing operator. The elastic part of a model can be made gradient-dependent by adding (or subtracting) Laplacians of elastic strain components, scaled with a square of a length parameter, to (or from) the strains themselves [1, 2]. Otherwise, as discussed in the previous section, a plasticity model can include the Laplacian of some equivalent plastic strain measure in the yield condition [12, 39, 56, 69] or evolution equations for the plastic variables [56, 78]. Yet another gradient-enhancement is achieved using additional averaging equations for suitable equivalent quantities or all (inelastic) strain tensors components [14, 18, 19, 49, 50].

Here, it is proposed to make the Cam-clay yield function dependent on the Laplacian of the hardening/softening parameter θ^{p} or of the plastic multiplier Λ. In result, the yield condition $F = 0$ in eq. (4.15) becomes a differential equation which must be solved numerically in addition to the equilibrium equations, cf. [12, 13]. This is achieved by taking the weak form of the yield function (which means the yield condition is not imposed pointwise, but in an integral sense, as was first proposed in [55]), and discretizing the plastic multiplier as a primary unknown next to displacements. This means that the backward Euler algorithm at the integration point level, described in Sect. 6.1, is employed for the first four residuals, in which $\Delta\Lambda$ is now a parameter computed from the nodal values of the discretized field. As has been explained, the fifth equation $(r_5 = 0)$ is solved at the global level, and the consistent tangent operator derived in eq. (4.27) must be modified accordingly.

It remains to specify the form of gradient-enhancement of the Cam-clay yield function. In principle, it is possible to assume that $p_c = p_c(\theta^{\mathrm{p}}, \nabla^2\theta^{\mathrm{p}})$ in eq. (4.15) or introduce a gradient term directly in the yield function:

$$F = q^2 + M^2 p\,[p - p_c(\theta^{\mathrm{p}}) + g\nabla^2(\theta^{\mathrm{p}})], \tag{6.1}$$

where $g > 0$ is a gradient scaling factor proportional to a square of an internal length scale l. There are however two difficulties: a) θ^{p} is not a monotonically growing parameter, so for dilatation the influence of the gradient term will be stabilizing, but for $\Delta\theta^{\mathrm{p}} < 0$ the gradient term should rather be switched off; b) since according to eq. (4.19) the volumetric plastic strain increment depends not only on Λ, but also on p and p_c, the gradient of a product of three functions would have to be computed.

Therefore, it is proposed to incorporate the Laplacian of the plastic multiplier itself, either in the form:

$$F = q^2 + M^2 p\,[p - p_c(\theta^{\mathrm{p}}) + g\nabla^2(\Lambda)], \tag{6.2}$$

or by writing:

$$F = q^2 + M^2 p\,[p - p_c(\bar{\theta}^{\mathrm{p}})], \tag{6.3}$$

where $\bar{\theta}^{\mathrm{p}}$ is a function of the averaged plastic multiplier $\bar{\Lambda}$ and the latter quantity is defined as:

$$\bar{\Lambda} = \Lambda + l^2\nabla^2(\Lambda). \tag{6.4}$$

The former option results in a stabilizing gradient effect on the yield function evolution irrespective of the sign of θ^{p}, the latter results in a slower growth of the quantity due to averaging, which is stabilizing only for dilatation.

Finally, the format in eq. (6.3) opens a possibility of using an additional averaging equation for the plastic multiplier, cf. [19], instead of the gradient-dependent yield condition. The averaging equation has the form:

$$\bar{\Lambda} - l^2\nabla^2(\bar{\Lambda}) = \Lambda, \tag{6.5}$$

and its weak form can be discretized instead of the weak form of the yield condition in order to compute $\bar{\Lambda}$. This however might require a modification of the evolution law for the preconsolidation measure.

6.2 Linearization and discretization in gradient plasticity

We start from the analysis of a single-phase medium. The finite element implementation is based on the following two weak-form equations governing respectively the static equilibrium and the plastic consistency:

$$\int_\Omega (\boldsymbol{L}\boldsymbol{v})^{\mathrm{T}}\boldsymbol{\sigma}\,\mathrm{d}V = \int_\Omega \boldsymbol{v}^{\mathrm{T}}\rho\boldsymbol{g}\,\mathrm{d}V + \int_\Gamma \boldsymbol{v}^{\mathrm{T}}\bar{\boldsymbol{t}}\,\mathrm{d}S, \tag{6.6a}$$

$$\int_\Omega v_p\,F(\boldsymbol{\sigma},\Lambda,\nabla^2\Lambda)\mathrm{d}V = 0\,, \tag{6.6b}$$

where $\boldsymbol{v}$ and v_p are suitable weighting functions. For a simple yield function, e.g. for Burzyński-Drucker-Prager (BDP) plasticity theory, the plastic multiplier Λ is proportional to the plastic strain measure ε^{p}. Equation (6.6b) requires the discretization of the Λ field.

Equations (6.6) are written for iteration $i+1$ of the incremental-iterative algorithm and the following decomposition is used:

$$\boldsymbol{\sigma}^{(i+1)} = \boldsymbol{\sigma}^{(i)} + \mathrm{d}\boldsymbol{\sigma}\,,\quad \Lambda^{(i+1)} = \Lambda^{(i)} + \mathrm{d}\Lambda. \tag{6.7}$$

In eq. (6.7) $\mathrm{d}\boldsymbol{\sigma}$ denotes the corrective increments in iteration $(i+1)$, which in eq. (5.30) where denoted by $\Delta\boldsymbol{\sigma}^{(i+1)}$. The yield function F is developed in a truncated Taylor series around $(\boldsymbol{\sigma}^{(i)},\Lambda^{(i)})$ to obtain the following incremental equations:

$$\int_\Omega (\boldsymbol{L}\boldsymbol{v})^{\mathrm{T}}\mathrm{d}\boldsymbol{\sigma}\,\mathrm{d}V = f_{ext} - f_{int} \tag{6.8a}$$

$$\int_\Omega v_p\,[\boldsymbol{n}^{\mathrm{T}}\mathrm{d}\boldsymbol{\sigma} - h\,\mathrm{d}\Lambda + g\nabla^2(\mathrm{d}\Lambda)]\,\mathrm{d}V = -\int_\Omega v_p\,F(\boldsymbol{\sigma}^{(i)},\Lambda^{(i)},\nabla^2\Lambda^{(i)})\,\mathrm{d}V, \tag{6.8b}$$

with

$$f_{ext} = \int_\Gamma \boldsymbol{v}^{\mathrm{T}}\bar{\boldsymbol{t}}\,\mathrm{d}S + \int_\Omega \boldsymbol{v}^{\mathrm{T}}\rho\boldsymbol{g}\,\mathrm{d}V, \tag{6.9a}$$

$$f_{int} = \int_\Omega (\boldsymbol{L}\boldsymbol{v})^{\mathrm{T}}\boldsymbol{\sigma}^{(i)}\,\mathrm{d}V. \tag{6.9b}$$

It is important to notice that, if the yield condition (3.12) is used in the classical return mapping algorithm to distinguish elastic and plastic states, a C^1-continuous interpolation of Λ is unavoidable, otherwise $\nabla^2\Lambda$ loses meaning [13, 46]. Therefore, the Laplacian term is not removed from the left-hand side of eq. (6.8b) using Green's formula, although this can be done if a homogeneous non-standard boundary condition $(\nabla\mathrm{d}\Lambda)^{\mathrm{T}}\boldsymbol{\nu} = 0$ is assumed ($\boldsymbol{\nu}$ is the vector normal to the surface of the plastic part of the body).

Adopting the standard additive decomposition of strain rate $\dot{\boldsymbol{\epsilon}}$ into an elastic and a plastic part, the stress rate is written as:

$$\dot{\boldsymbol{\sigma}} = \boldsymbol{D}^{\mathrm{e}}(\dot{\boldsymbol{\epsilon}} - \dot{\Lambda}\boldsymbol{m}). \tag{6.10}$$

Substituting the incremental form of eq. (6.10) into eqs (6.8a) and (6.8b) we obtain:

$$\int_\Omega (\boldsymbol{L}\boldsymbol{v})^{\mathrm{T}}\boldsymbol{D}^{\mathrm{e}}\mathrm{d}\boldsymbol{\epsilon}\,\mathrm{d}V - \int_\Omega (\boldsymbol{L}\boldsymbol{v})^{\mathrm{T}}\boldsymbol{D}^{\mathrm{e}}\boldsymbol{m}^{(i)}\,\mathrm{d}\Lambda\,\mathrm{d}V = f_{ext} - f_{int}, \tag{6.11a}$$

$$\begin{aligned}\int_\Omega v_p\,\boldsymbol{n}^{\mathrm{T}(i)}\boldsymbol{D}^{\mathrm{e}}\mathrm{d}\boldsymbol{\epsilon}\,\mathrm{d}V - \int_\Omega v_p\left[(h^{(i)} + \boldsymbol{n}^{\mathrm{T}(i)}\boldsymbol{D}^{\mathrm{e}}\boldsymbol{m}^{(i)})\,\mathrm{d}\Lambda - g\nabla^2(\mathrm{d}\Lambda)\right]\mathrm{d}V = \\ = -\int_\Omega v_p\,F(\boldsymbol{\sigma}^{(i)}, \Lambda^{(i)}, \nabla^2\Lambda^{(i)})\,\mathrm{d}V,\end{aligned} \tag{6.11b}$$

Next, we discretize eqs (6.11a) and (6.11b). The displacements $\boldsymbol{u}$ and the plastic multiplier Λ are interpolated as follows:

$$\boldsymbol{u} = \boldsymbol{N}\bar{\boldsymbol{u}}\,, \qquad \Lambda = \boldsymbol{h}^{\mathrm{T}}\bar{\boldsymbol{\Lambda}}, \tag{6.12}$$

where $\boldsymbol{N}$ and $\boldsymbol{h}$ contain interpolation polynomials for the displacements and the plastic multiplier, respectively, and $\bar{\boldsymbol{u}}$ and $\bar{\boldsymbol{\Lambda}}$ are arrays which contain their respective discrete nodal values. Consequently, we obtain for the strains $\boldsymbol{\epsilon}$ and the Laplacian of the plastic multiplier:

$$\boldsymbol{\epsilon} = \boldsymbol{B}\bar{\boldsymbol{u}}\,, \qquad \nabla^2\Lambda = \boldsymbol{s}^{\mathrm{T}}\bar{\boldsymbol{\Lambda}}, \tag{6.13}$$

where $\boldsymbol{B} = \boldsymbol{L}\boldsymbol{N}$ and $\boldsymbol{s} = \nabla^2\boldsymbol{h}$. The respective weighting functions are interpolated similarly according to the Galerkin approach. The used interpolation functions are quadratic for the displacements and cubic (Hermitean) for the plastic multiplier. Invoking the usual argument that the weighting functions are arbitrary, the discrete counterpart of eqs (6.11) is the following set of linear algebraic equations:

$$\begin{bmatrix} \boldsymbol{K}_{uu} & \boldsymbol{K}_{u\Lambda} \\ \boldsymbol{K}_{\Lambda u} & \boldsymbol{K}_{\Lambda\Lambda} \end{bmatrix} \begin{bmatrix} \mathrm{d}\bar{\boldsymbol{u}} \\ \mathrm{d}\bar{\boldsymbol{\Lambda}} \end{bmatrix} = \begin{bmatrix} \boldsymbol{f}_{ext} - \boldsymbol{f}_{int} \\ \boldsymbol{f}_\Lambda \end{bmatrix}, \tag{6.14}$$

where the respective submatrices are:

$$\boldsymbol{K}_{uu} = \int_\Omega \boldsymbol{B}^{\mathrm{T}}\boldsymbol{D}^{\mathrm{e}}\boldsymbol{B}\,\mathrm{d}V, \tag{6.15a}$$

$$\boldsymbol{K}_{u\Lambda} = -\int_\Omega \boldsymbol{B}^{\mathrm{T}}\boldsymbol{D}^{\mathrm{e}}\boldsymbol{m}^{(i)}\boldsymbol{h}^{\mathrm{T}}\,\mathrm{d}V, \tag{6.15b}$$

$$\boldsymbol{K}_{\Lambda u} = -\int_\Omega \boldsymbol{h}\boldsymbol{n}^{\mathrm{T}(i)}\boldsymbol{D}^{\mathrm{e}}\boldsymbol{B}\,\mathrm{d}V, \tag{6.15c}$$

$$\boldsymbol{K}_{\Lambda\Lambda} = \int_\Omega [(h^{(i)} + \boldsymbol{n}^{\mathrm{T}(i)}\boldsymbol{D}^{\mathrm{e}}\boldsymbol{m}^{(i)})\boldsymbol{h}\boldsymbol{h}^{\mathrm{T}} - g\boldsymbol{h}\boldsymbol{s}^{\mathrm{T}}]\,\mathrm{d}V, \tag{6.15d}$$

$$\boldsymbol{f}_\Lambda = \int_\Omega \boldsymbol{h}F(\boldsymbol{\sigma}^{(i)}, \Lambda^{(i)}, \nabla^2\Lambda^{(i)})\,\mathrm{d}V. \tag{6.15e}$$

and $\boldsymbol{f}_{ext}$ and $\boldsymbol{f}_{int}$ are the external and internal force vectors, respectively. For an elastic process we set $\boldsymbol{n} = \boldsymbol{m} = \boldsymbol{0}$, so the off-diagonal matrices are zero, but matrix $\boldsymbol{K}_{\lambda\Lambda}$ is non-singular, so that $\mathrm{d}\bar{\boldsymbol{\Lambda}} = \boldsymbol{0}$ is obtained. Further details of finite element implementation can be found in [13].

One further remark on linearization is however made. In the gradient-dependent BDP plasticity one obtains the consistent tangent operator by differentiating the incremental constitutive relation (6.10):

$$\Delta\boldsymbol{\sigma} = \boldsymbol{D}^{\mathrm{e}}(\Delta\boldsymbol{\epsilon} - \Delta\Lambda\boldsymbol{m}) \tag{6.16}$$

to obtain:

$$\mathrm{d}\boldsymbol{\sigma} = \boldsymbol{D}^{\mathrm{e}}\left(\mathrm{d}\boldsymbol{\epsilon} - \mathrm{d}\Lambda\boldsymbol{m} - \Delta\Lambda\frac{\mathrm{d}\boldsymbol{m}}{\mathrm{d}\boldsymbol{\sigma}}\mathrm{d}\boldsymbol{\sigma}\right). \tag{6.17}$$

Bringing the last term to the left-hand side we realize that for consistent linearization $\boldsymbol{D}^{\mathrm{e}}$ must be substituted in eqs. 6.14 by the following operator:

$$\boldsymbol{D}^{cons} = \left(\boldsymbol{I} + \Delta\Lambda\boldsymbol{D}^{\mathrm{e}}\frac{\mathrm{d}\boldsymbol{m}}{\mathrm{d}\boldsymbol{\sigma}}\right)^{-1}\boldsymbol{D}^{\mathrm{e}}. \tag{6.18}$$

6.3 Gradient-dependent Cam-clay plasticity; u-Λ element

In the numerical implementation we focus on the gradient-dependent Cam-clay yield function proposed in eq. (6.2), written in terms of the stress invariants and the plastic multiplier:

$$F(\boldsymbol{\sigma}, \Lambda, \nabla^2\Lambda) = q^2 + M^2 p\,[p - p_c(\Delta\theta^{\mathrm{p}}) + g\nabla^2\Lambda]. \tag{6.19}$$

The gradient coefficient g scales the nonlocality effect and provides stabilization (hardening) in the model. Its unit results from the fact that the unit of the yield function is $[kN^2/m^4]$, hence the unit of the plastic multiplier is $[m^2/kN]$ and of its Laplacian $[1/kN]$. Unlike the standard gradient plasticity, the Laplacian term is here additionally scaled by pressure p.
The preconsolidation parameter p_c evolves according to eq. (4.17):

$$p_c = p_{c0}\exp(-\frac{1+e_0}{\lambda-\kappa}\Delta\theta^{\mathrm{p}}). \tag{6.20}$$

The increment of plastic dilatation according to eq. (4.19) is computed as:

$$\mathrm{d}\theta^{\mathrm{p}} = -\mathrm{d}\Lambda M^2(2p - p_c + g\nabla^2\Lambda). \tag{6.21}$$

We will now derive the specific form of the two weak-form equations of static equilibrium and plastic consistency (6.6), written for iteration $i+1$. With $F^{(i+1)} = F^{(i)} + \mathrm{d}F$ and the decompositions in eq. (6.7), they have the form:

$$\int_\Omega (\boldsymbol{L}\boldsymbol{v})^{\mathrm{T}} \mathrm{d}\boldsymbol{\sigma}\, \mathrm{d}V = f_{ext} - f_{int} \tag{6.22a}$$

$$-\int_\Omega v_p \left[\frac{\partial F}{\partial \boldsymbol{\sigma}} \mathrm{d}\boldsymbol{\sigma} + \frac{\partial F}{\partial \Lambda} \mathrm{d}\Lambda + \frac{\partial F}{\partial \nabla^2 \Lambda} \nabla^2(\mathrm{d}\Lambda) \right] \mathrm{d}V = f_\Lambda \tag{6.22b}$$

where the chain rule has been used to compute $\mathrm{d}f$, f_{ext} and f_{int} are defined in eqs (6.9) and f_Λ is defined as:

$$f_\Lambda = \int_\Omega v_p\, F\left(\boldsymbol{\sigma}^{(i)}, \Lambda^{(i)}, \nabla^2 \Lambda^{(i)}\right) \mathrm{d}V. \tag{6.23}$$

As in the previous section, the algorithm involves the discretization of the plastic multiplier field. It is computed from nodal values and plays the role similar to strains: the return mapping algorithm is now driven by the increments of strain and plastic multiplier. In the internal iterative loop performed at the integration point to compute the stress satisfying the yield condition both $\boldsymbol{\epsilon}$ and Λ (or their total increments $\Delta\boldsymbol{\epsilon}$ and $\Delta\Lambda$) are constant. However, both these fields change in the global equilibrium iterations, so that the linearization of stress is now computed as:

$$\mathrm{d}\boldsymbol{\sigma} = \frac{\mathrm{d}\boldsymbol{\sigma}}{\mathrm{d}\boldsymbol{\epsilon}} \mathrm{d}\boldsymbol{\epsilon} + \frac{\mathrm{d}\boldsymbol{\sigma}}{\mathrm{d}\Lambda} \mathrm{d}\Lambda. \tag{6.24}$$

We now have to determine the stress increment $\mathrm{d}\boldsymbol{\sigma}$ and the derivatives in eq. (6.22b).

In the algorithm for the gradient-dependent Cam-clay plasticity we follow the concept of consistent linearization used for the local model. Hence, we write:

$$\boldsymbol{\sigma} = \boldsymbol{\sigma}\left(\boldsymbol{s}(\Delta\boldsymbol{\epsilon}, \Delta\Lambda), \Delta\boldsymbol{\epsilon}, \Delta\Lambda\right), \tag{6.25}$$

where vector $\boldsymbol{s} = [p, q, \bar{G}, p_c]$ now contains only four primary unknowns. The Newton algorithm similar to the one described in Sect. 6.1 is used to compute these unknowns, only now we deal with residuals $\boldsymbol{r} = [r_1, r_2, r_3, r_4]$, and the Jacobian matrix $\boldsymbol{J} = \frac{\partial \boldsymbol{r}}{\partial \boldsymbol{s}}$ has the size 4×4. The respective derivatives in eq. (6.24) are computed according to eq. (4.27):

$$\frac{\mathrm{d}\boldsymbol{\sigma}}{\mathrm{d}\boldsymbol{\epsilon}} = \frac{\partial \boldsymbol{\sigma}}{\partial \boldsymbol{s}} \frac{\mathrm{d}\boldsymbol{s}}{\mathrm{d}\boldsymbol{\epsilon}} + \frac{\partial \boldsymbol{\sigma}}{\partial \boldsymbol{\epsilon}} = \frac{\partial \boldsymbol{\xi}}{\partial \boldsymbol{\epsilon}} - \boldsymbol{\Pi} \frac{\partial p}{\partial \boldsymbol{\epsilon}} - \left(\frac{\partial \boldsymbol{\xi}}{\partial \boldsymbol{s}} - \boldsymbol{\Pi} \frac{\partial p}{\partial \boldsymbol{s}} \right) \boldsymbol{J}^{-1} \left(\frac{\partial \boldsymbol{r}}{\partial \boldsymbol{\epsilon}} \right) \tag{6.26}$$

and the following one:

$$\frac{\mathrm{d}\boldsymbol{\sigma}}{\mathrm{d}\Lambda} = \frac{\partial \boldsymbol{\sigma}}{\partial \boldsymbol{s}} \frac{\mathrm{d}\boldsymbol{s}}{\mathrm{d}\Lambda} + \frac{\partial \boldsymbol{\sigma}}{\partial \Lambda} = \frac{\partial \boldsymbol{\xi}}{\partial \Lambda} - \boldsymbol{\Pi} \frac{\partial p}{\partial \Lambda} - \left(\frac{\partial \boldsymbol{\xi}}{\partial \boldsymbol{s}} - \boldsymbol{\Pi} \frac{\partial p}{\partial \boldsymbol{s}} \right) \boldsymbol{J}^{-1} \left(\frac{\partial \boldsymbol{r}}{\partial \Lambda} \right). \tag{6.27}$$

The partial derivatives are given in the Appendix, in particular from the Jacobian for the local model one can compute $\frac{\partial \boldsymbol{r}}{\partial \Lambda} = \boldsymbol{J}_{i5},\ i = 1 \ldots 4.$

Next, the increment of stress $\mathrm{d}\boldsymbol{\sigma}$ from eq. (6.24) is substituted into eqs (6.22):

$$\int_\Omega (\boldsymbol{L}\boldsymbol{v})^{\mathrm{T}} \frac{\mathrm{d}\boldsymbol{\sigma}}{\mathrm{d}\boldsymbol{\epsilon}} \mathrm{d}\boldsymbol{\epsilon}\, \mathrm{d}V + \int_\Omega (\boldsymbol{L}\boldsymbol{v})^{\mathrm{T}} \frac{\mathrm{d}\boldsymbol{\sigma}}{\mathrm{d}\Lambda} \mathrm{d}\Lambda\, \mathrm{d}V = f_{ext} - f_{int} \tag{6.28a}$$

$$- \int_\Omega v_p \frac{\partial F}{\partial \boldsymbol{\sigma}} \frac{\mathrm{d}\boldsymbol{\sigma}}{\mathrm{d}\boldsymbol{\epsilon}} \mathrm{d}\boldsymbol{\epsilon}\, \mathrm{d}V - \int_\Omega v_p \left(\frac{\partial F}{\partial \boldsymbol{\sigma}} \frac{\mathrm{d}\boldsymbol{\sigma}}{\mathrm{d}\Lambda} + \frac{\partial F}{\partial \Lambda} \right) \mathrm{d}\Lambda\, \mathrm{d}V - \\ - \int_\Omega v_p \frac{\partial F}{\partial \nabla^2 \Lambda} \nabla^2 (\mathrm{d}\Lambda)\, \mathrm{d}V = f_\Lambda \tag{6.28b}$$

The remaining derivatives are computed as follows:

$$\frac{\partial F}{\partial \boldsymbol{\sigma}} = \frac{\partial F}{\partial q} \frac{\partial q}{\partial \boldsymbol{\xi}} \frac{\partial \boldsymbol{\xi}}{\partial \boldsymbol{\sigma}} + \frac{\partial F}{\partial p} \frac{\partial p}{\partial \boldsymbol{\sigma}} = 3\boldsymbol{\xi}^{\mathrm{T}} \boldsymbol{R}\boldsymbol{Q} - \frac{1}{3} M^2 (2p - p_c + g\nabla^2\Lambda) \boldsymbol{\Pi}^{\mathrm{T}}, \tag{6.29}$$

$$\frac{\partial F}{\partial \Lambda} = -M^2 p \frac{\partial p_c}{\partial \theta^{\mathrm{p}}} \frac{\partial \theta^{\mathrm{p}}}{\partial \Lambda}, \tag{6.30}$$

$$\frac{\partial p_c}{\partial \theta^{\mathrm{p}}} = -p_{c0} B \exp(-B\Delta\theta^{\mathrm{p}}), \qquad \frac{\partial \theta^{\mathrm{p}}}{\partial \Lambda} = -M^2(2p - p_c + g\nabla^2\Lambda), \tag{6.31}$$

$$\frac{\partial F}{\partial \nabla^2 \Lambda} = M^2 g p. \tag{6.32}$$

Finally, as in eqs (6.12) we discretize eqs (6.11a) and (6.11b) to obtain the set of linear algebraic equations similar to (6.14) with the following definitions of the submatrices (the iteration index has been skipped):

$$\boldsymbol{K}_{uu} = \int_\Omega \boldsymbol{B}^{\mathrm{T}} \frac{\mathrm{d}\boldsymbol{\sigma}}{\mathrm{d}\boldsymbol{\epsilon}} \boldsymbol{B}\, \mathrm{d}V, \tag{6.33a}$$

$$\boldsymbol{K}_{u\Lambda} = - \int_\Omega \boldsymbol{B}^{\mathrm{T}} \frac{\mathrm{d}\boldsymbol{\sigma}}{\mathrm{d}\Lambda} \boldsymbol{h}^{\mathrm{T}}\, \mathrm{d}V, \tag{6.33b}$$

$$\boldsymbol{K}_{\Lambda u} = - \int_\Omega \boldsymbol{h} \frac{\partial F}{\partial \boldsymbol{\sigma}} \frac{\mathrm{d}\boldsymbol{\sigma}}{\mathrm{d}\boldsymbol{\epsilon}} \boldsymbol{B}\, \mathrm{d}V, \tag{6.33c}$$

$$\boldsymbol{K}_{\Lambda\Lambda} = - \int_\Omega \left[\left(\frac{\partial F}{\partial \boldsymbol{\sigma}} \frac{\mathrm{d}\boldsymbol{\sigma}}{\mathrm{d}\Lambda} + \frac{\partial F}{\partial \Lambda} \right) \boldsymbol{h}\boldsymbol{h}^{\mathrm{T}} + \frac{\partial F}{\partial \nabla^2 \Lambda} \boldsymbol{h}\boldsymbol{p}^{\mathrm{T}} \right] \mathrm{d}V, \tag{6.33d}$$

$$\boldsymbol{f}_\Lambda = \int_\Omega \boldsymbol{h} F(\boldsymbol{\sigma}, \Lambda, \nabla^2\Lambda)\, \mathrm{d}V. \tag{6.33e}$$

In Fig. 6.1 the nodes are marked in which the appropriate field is interpolated (eight nodes for the displacements and four for the plastic multiplier).

6.4 Discretization-independent localization in biaxial compression test

The results presented in Sect. 4.7 show the mesh-sensitivity of the numerical simulations for the biaxial compression test. In order to avoid this the modified Cam-clay model has

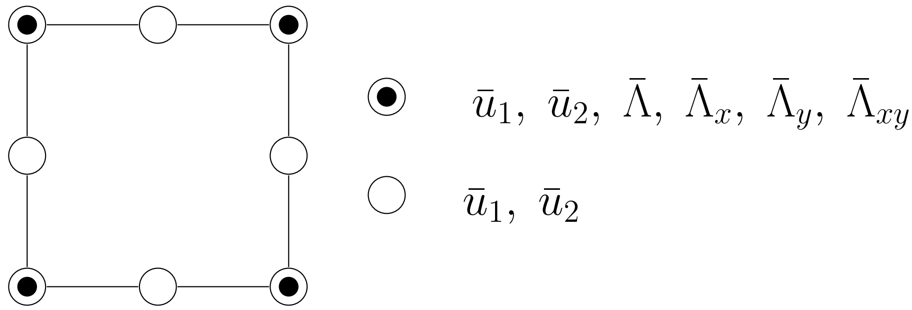

Figure 6.1: Regularized finite element u-Λ

been regularized in the way described in Sect. 6.3, i.e. the gradient term $g\nabla^2\Lambda$ has been included in the plasticity function. The following calculations are repeated with the gradient-dependent Cam-clay model to study the effectiveness of the introduced regularization. The following additional material model parameter has been adopted: $g = 0.05$ kN^2/m^2.

The diagrams in Fig 6.2 as well as the localization patterns shown in Figs 6.3-6.4 prove the mesh-independence of numerical results for the gradient-dependent Cam-clay model. In fact, unlike in the gradient plasticity with a standard (e.g. Huber-Mises) yield function and linear softening [13], in Cam-clay gradient plasticity the shear band width grows since softening is nonlinear. The shear band patterns in Figs 6.4-6.3 are plotted for the vertical displacement of the upper edge equal to 0.016m. The distribution of volume changes (plastic dilatancy increments) exhibits at first similar shear bands as the profiles of the second invariant of the deviatoric strain tensor, but as the critical state is approached, the material volume ceases to change.

6.5 Influence of gradient scaling factor g

The following example allows us to investigate the influence of the gradient scaling factor on the obtained results. Two values of gradient constant g are considered: $g = 0.025$ kN^2/m^2 and $g = 0.05$ kN^2/m^2. In Fig. 6.5 the load-deformation curves are shown. It can be noticed that the solution for a $g = 0.05$ kN^2/m^2 is a bit more ductile. In Figs 6.6- 6.7 the distribution of the equivalent plastic strain at various stages of numerical calculations is presented for two values of g. We can observe that the shear bands evolve during the loading process. The width of the localization zone is different for the two considered cases and determined by the value of g. It can easily be noticed that the shear band width is growing with the increasing gradient scaling factor.

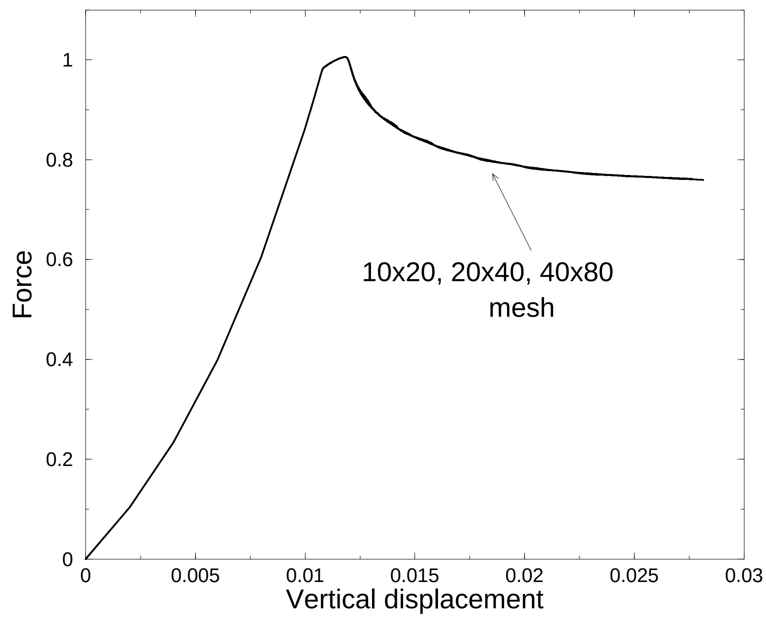

Figure 6.2: Load-deformation curves (gradient Cam-clay model)

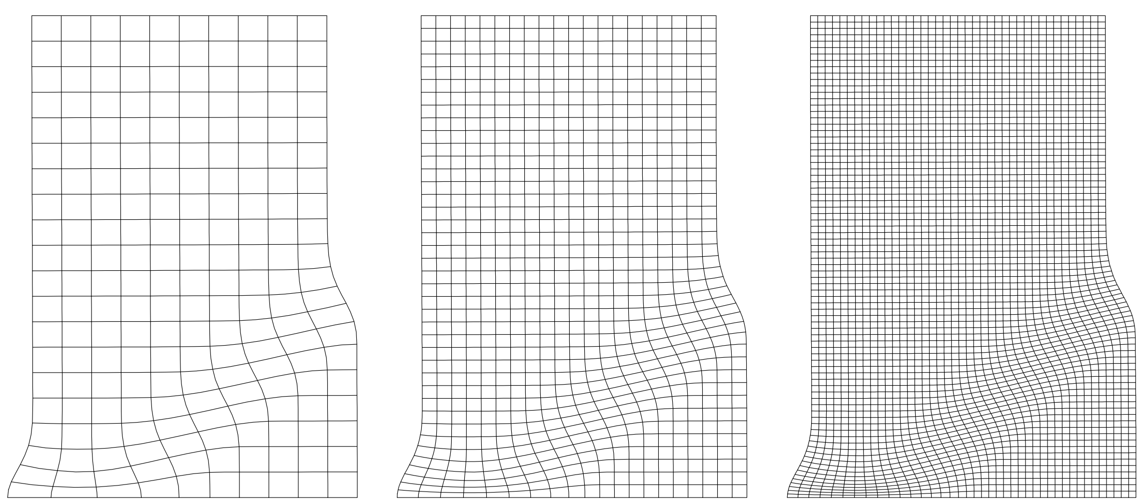

Figure 6.3: Deformed meshes (gradient Cam-Clay model)

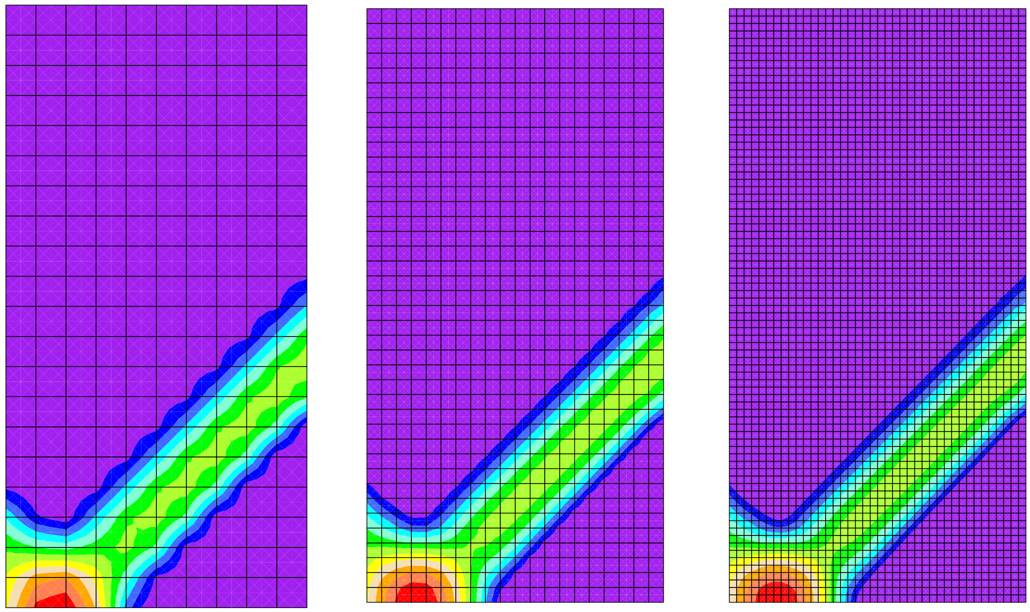

Figure 6.4: Distribution of invariant J_2 of strain tensor (gradient Cam-Clay model)

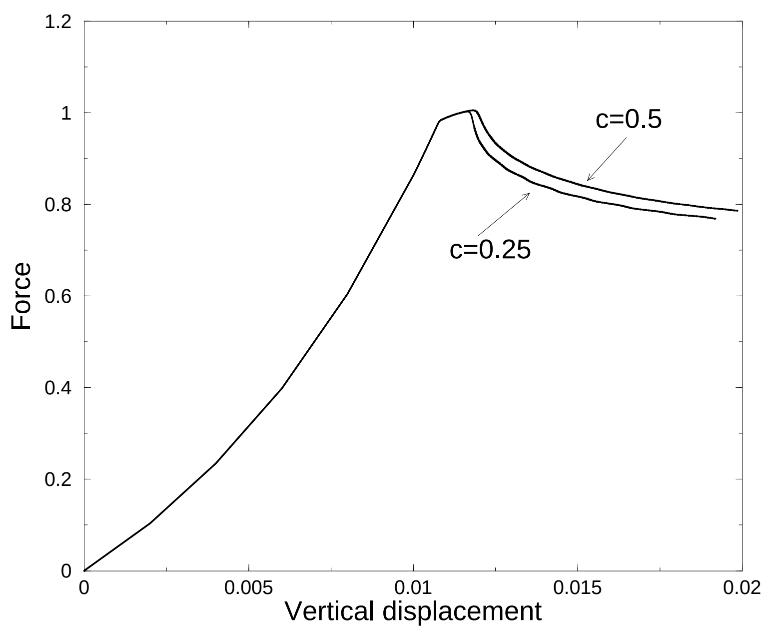

Figure 6.5: Load-deformation curves for different values of gradient scaling factor $g = 0.025$ kN^2/m^2 and $g = 0.05$ kN^2/m^2

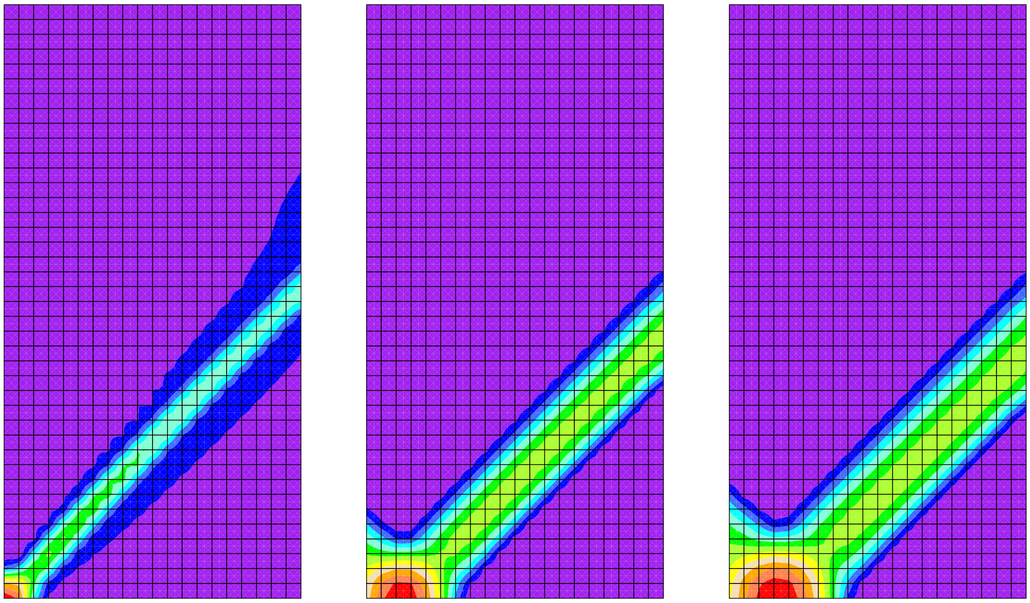

Figure 6.6: Equivalent plastic strain distribution for gradient scaling factor $g = 0.025$ kN^2/m^2/

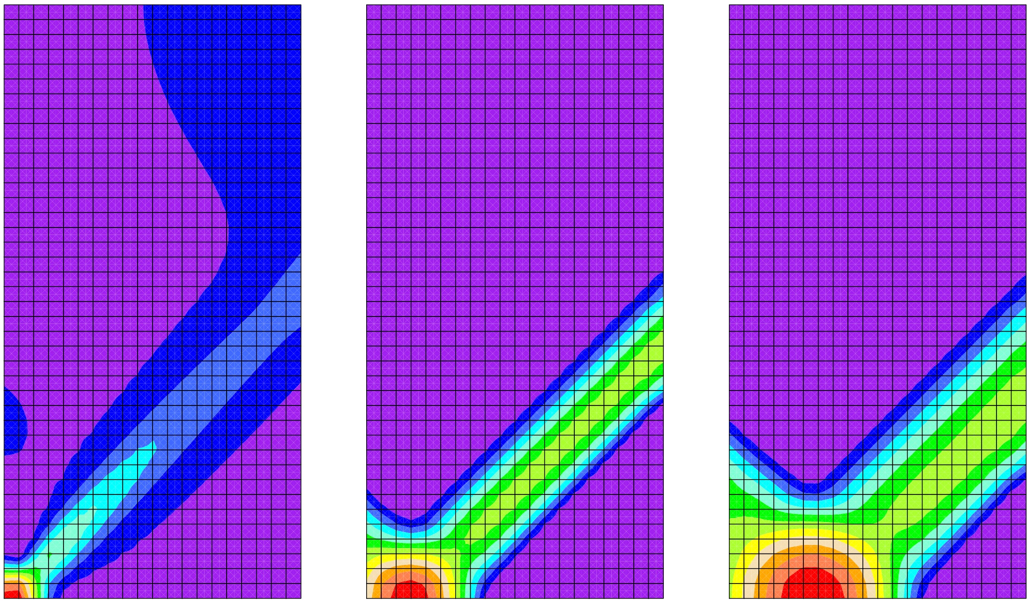

Figure 6.7: Equivalent plastic strain distribution for gradient scaling factor $g = 0.05$ kN^2/m^2

6.6 Influence of imperfections

Unlike in dynamics (cf. [21]), in static simulations of localization phenomena the imperfections merely trigger the process and set the initial position of deformation bands. Here, the analysis is limited to the influence of imperfection location and its intensity on the results. In Fig. 6.8 the locations of the imperfection area are shown. In the presented tests, four or eight elements are assigned a 10% or a 1% smaller value of the initial overconsolidation measure. Now, only one discretization with the medium mesh is considered.

In Figs 6.9- 6.13 the contour plots with the distributions of invariant J_2 of the strain tensor are shown for different loading process stages. In all cases the shear band evolution is observed. First a crossed pattern of bands is formed, then one of them remains active, since this is energetically preferable. Finally, as the critical state is approached, the band width increases. Unlike in gradient plasticity with a constant internal length parameter, standard (e.g. HMH) yield function and linear softening, in Cam-clay gradient plasticity the shear band width grows since softening is nonlinear. A uniaxial approximation of the relation between the gradient scaling coefficient g and the internal length scale l is $g = -hl^2$, where h is the softening modulus, and in this case the derivative of p_c with respect to $\Delta\Lambda$. The width of the shear band is governed by l and for dilatant flow the derivative decreases, hence l apparently grows. To accommodate this the gradient factor g would have to be made a (decreasing) function of a plastic strain measure (which would physically mean a reduction of nonlocality as the critical state is approached).

In the presented simulations the smaller value of the initial preconsolidation pressure is assigned in a small area of the specimen to initiate the shear band formation. However, the initial void ratio can also be used in order to start the localization process.

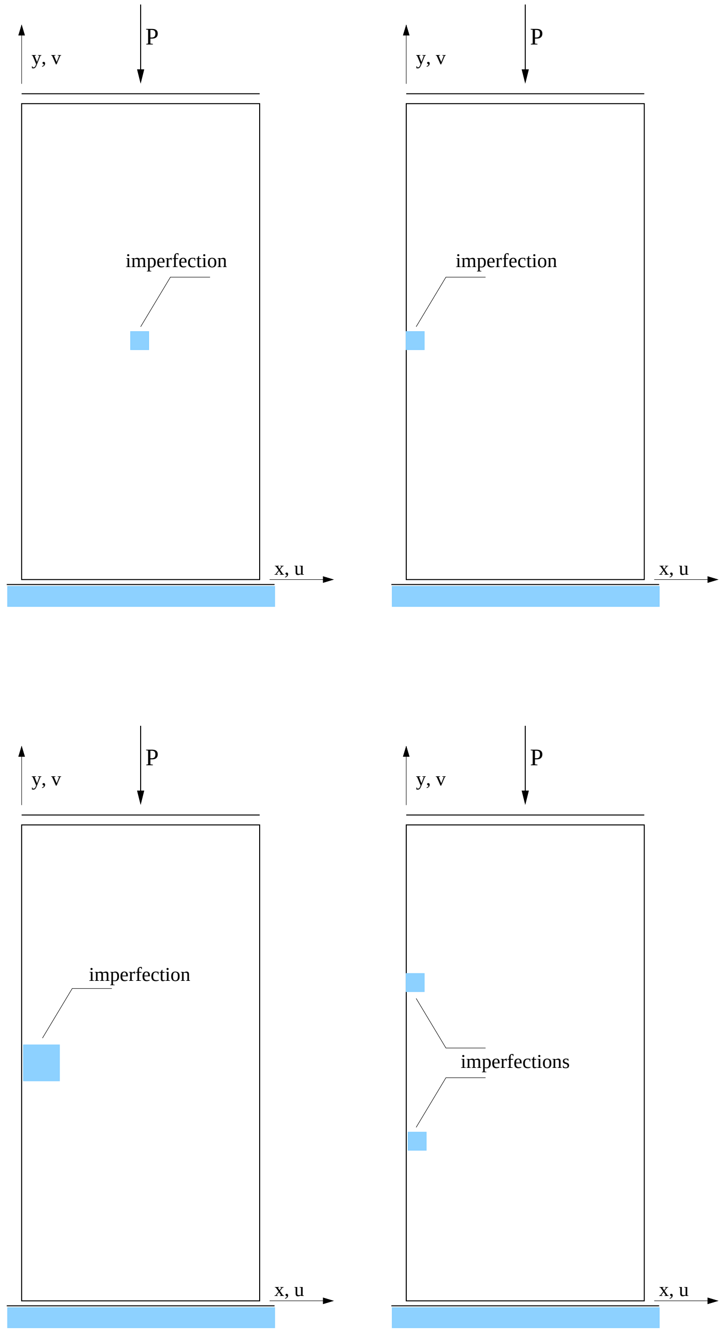

Figure 6.8: Imperfection location

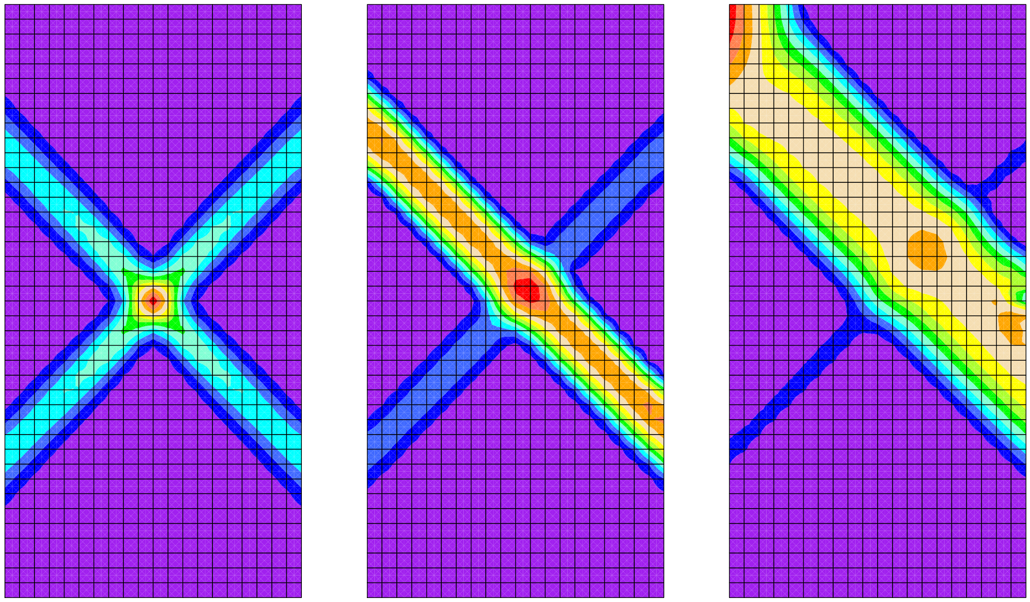

Figure 6.9: Shear band evolution for 10% imperfection located in the middle of the sample

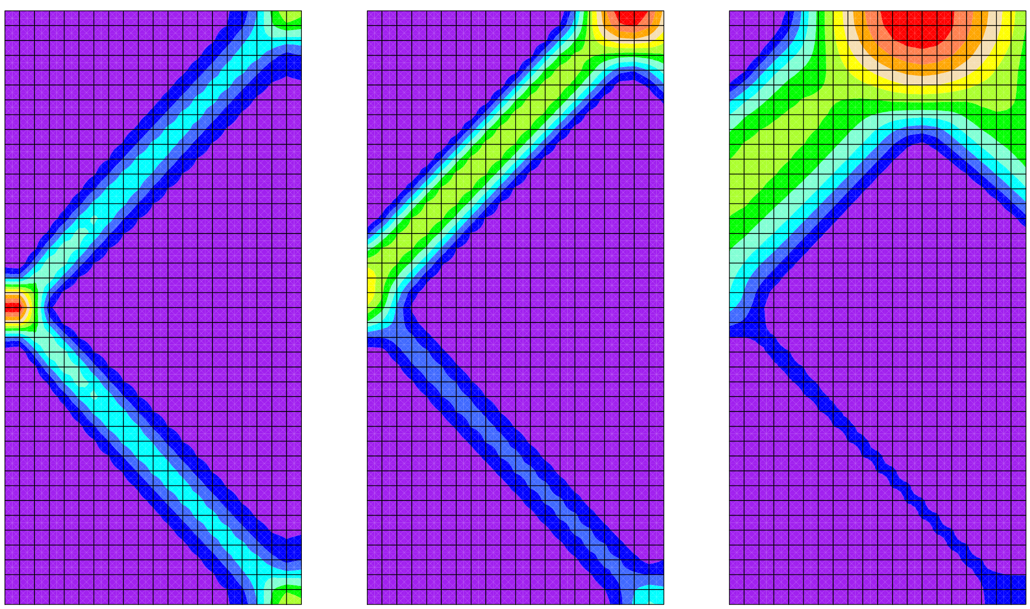

Figure 6.10: Shear band evolution for 10% imperfection located in the middle of the left edge of the sample

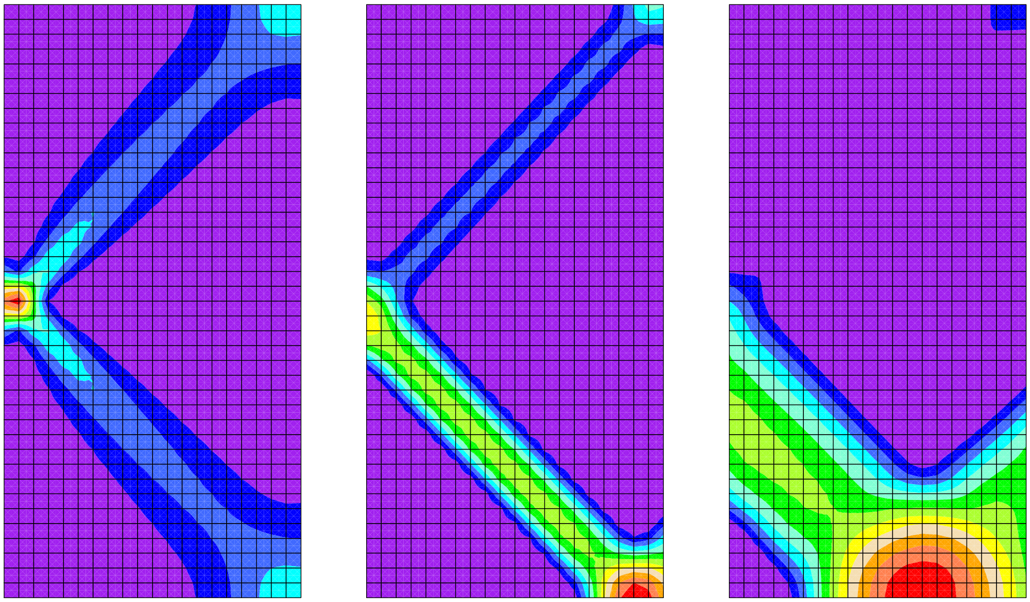

Figure 6.11: Shear band evolution for 1% imperfection located in the middle of the left edge of the sample

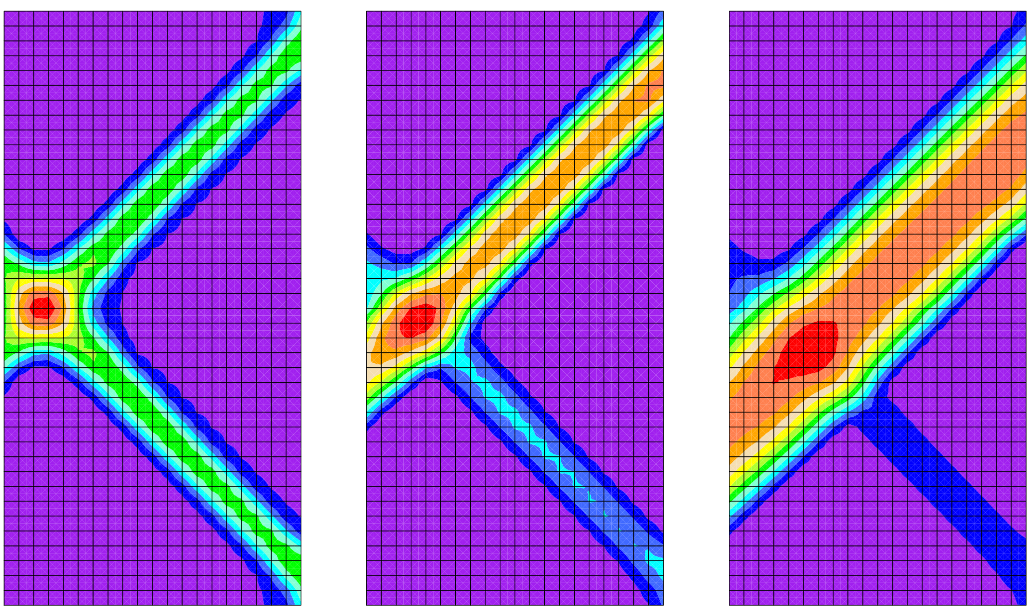

Figure 6.12: Shear band evolution for 10% eight-element imperfection located in the middle of the left edge of the sample

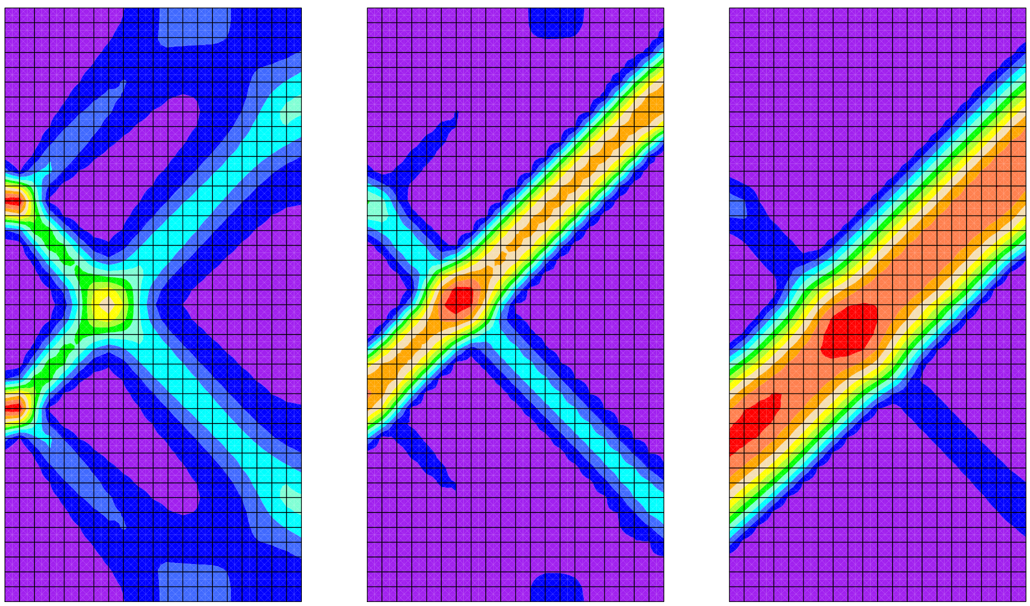

Figure 6.13: Shear band evolution for two 10% imperfections located on the left edge of the sample

Chapter 7

Gradient-dependent Cam-clay model for two-phase medium

The results of numerical simulations presented in Sect. 5.8 do not show a significant stabilizing effect of the fluid phase in strain localization problems. Therefore, a regularization of the softening constitutive model for soil seems to be necessary within a two-phase description. The gradient regularization of the modified Cam-clay model, described in Sect. 6.3, is now applied to two-phase medium.

7.1 Discretization of three-field formulation; u-p-Λ element

To discretize the problem of pore pressure evolution combined with the gradient-enhanced plasticity modelling of the solid skeleton, the weak forms of equations (5.9), (5.10) and (6.19) are required.

The weak form of the momentum balance equation reads:

$$\int_\Omega \boldsymbol{v}^{\mathrm{T}}(\boldsymbol{\nabla}\boldsymbol{\sigma}_t + \hat{\rho}\boldsymbol{g})\,\mathrm{d}\Omega = \boldsymbol{0} \tag{7.1}$$

The weak form of the plastic consistency condition is written as:

$$\int_\Omega v_p\,F(\boldsymbol{\sigma}, \Lambda, \nabla^2\Lambda)\mathrm{d}\Omega = 0 \tag{7.2}$$

The weak form of the mass balance equation is:

$$\int_\Omega w(\boldsymbol{\nabla}\cdot\dot{\boldsymbol{u}} + \boldsymbol{\nabla}\cdot\boldsymbol{v}_d + n\frac{\dot{p}_f}{K_f})\,\mathrm{d}\Omega = 0 \tag{7.3}$$

In eqs (7.1-7.3) $\boldsymbol{v}$, v_p and w are suitable weighting functions.

After the integration of momentum and mass balance equations by parts we obtain:

$$\int_{\Omega} (\boldsymbol{L}\boldsymbol{v})^{\mathrm{T}} \boldsymbol{\sigma}_t \,\mathrm{d}\Omega - \int_{\Omega} \boldsymbol{v}^{\mathrm{T}} \hat{\rho} \boldsymbol{g} \,\mathrm{d}\Omega - \int_{\Gamma_t} \boldsymbol{v}^{\mathrm{T}} \,\bar{\boldsymbol{t}} \,\mathrm{d}\Gamma = \boldsymbol{0}, \tag{7.4}$$

$$\int_{\Omega} w \boldsymbol{\nabla}^{\mathrm{T}} \dot{\boldsymbol{u}} \,\mathrm{d}\Omega - \int_{\Omega} (\boldsymbol{\nabla} w)^{\mathrm{T}} \boldsymbol{v}_d \,\mathrm{d}\Omega + \int_{\Omega} w \frac{n}{K_f} \dot{p}_f \,\mathrm{d}\Omega + \int_{\Gamma_q} w \,\bar{\boldsymbol{q}} \,\mathrm{d}\Gamma_q = 0. \tag{7.5}$$

In eqs (7.4-7.5) natural boundary conditions have been incorporated.

We introduce the following finite element discretization for displacements $\boldsymbol{u}$, plastic multiplier Λ and excess pore pressure p_f:

$$\boldsymbol{u} = \boldsymbol{N} \,\bar{\boldsymbol{u}} \;, \qquad \Lambda = \boldsymbol{h}^{\mathrm{T}} \bar{\boldsymbol{\Lambda}} \;, \qquad p_f = \boldsymbol{N}_p \,\bar{\boldsymbol{p}} \;, \tag{7.6}$$

where $\boldsymbol{N}$, $\boldsymbol{h}$ and $\boldsymbol{N}_p$ contain the respective interpolation polynomials and $\bar{\boldsymbol{u}}$, $\bar{\boldsymbol{\Lambda}}$ and $\bar{\boldsymbol{p}}$ are vectors with the discrete nodal values. The weighting functions are interpolated similarly according to the Galerkin approach. The used interpolation functions are quadratic for the displacements, linear for the pore pressure and cubic (Hermitean) for the plastic multiplier. In Fig. 7.1 it is shown at which nodes which quantities are nodal degrees of freedom.

Due to the assumption of linear kinematic relations we can introduce matrix $\boldsymbol{B} = \boldsymbol{L}\boldsymbol{N}$. With vector $\boldsymbol{s} = \nabla^2 \boldsymbol{h}$ the discretization of strains and of the Laplacian of plastic multiplier can be expressed as in Sect. 6.2:

$$\boldsymbol{\epsilon} = \boldsymbol{B}\bar{\boldsymbol{u}}, \qquad \nabla^2 \Lambda = \boldsymbol{s}^{\mathrm{T}} \bar{\boldsymbol{\Lambda}}. \tag{7.7}$$

After linearization of the governing equations and after time integration of eqs (7.1) and (7.5), (the implicit backward Euler integration scheme is used as in Sect. 5.5.2) introducing the employed interpolation of the problem variables and invoking the usual argument that the weighting functions are arbitrary, the following coupled system of linearized equations in a matrix form is obtained:

$$\begin{bmatrix} \boldsymbol{K}_{uu} & \boldsymbol{K}_{u\Lambda} & -\boldsymbol{K}_{up} \\ \boldsymbol{K}_{\Lambda u} & \boldsymbol{K}_{\Lambda\Lambda} & \boldsymbol{0} \\ \boldsymbol{K}_{up}^{\mathrm{T}} & \boldsymbol{0} & \boldsymbol{K}_{pp} \end{bmatrix} \begin{bmatrix} \Delta\bar{\boldsymbol{u}} \\ \Delta\bar{\boldsymbol{\Lambda}} \\ \Delta\bar{\boldsymbol{p}} \end{bmatrix} = \begin{bmatrix} \boldsymbol{f}_{ext} - \boldsymbol{f}_{int} \\ \boldsymbol{f}_{\Lambda} \\ \boldsymbol{f}_{f} \end{bmatrix}. \tag{7.8}$$

The definitions of the submatrices are as follows:

$$\boldsymbol{K}_{uu} = \int_\Omega \boldsymbol{B}^{\mathrm{T}} \frac{\mathrm{d}\boldsymbol{\sigma}}{\mathrm{d}\boldsymbol{\epsilon}} \boldsymbol{B}\,\mathrm{d}\Omega, \tag{7.9a}$$

$$\boldsymbol{K}_{u\Lambda} = -\int_\Omega \boldsymbol{B}^{\mathrm{T}} \frac{\mathrm{d}\boldsymbol{\sigma}}{\mathrm{d}\Lambda} \boldsymbol{h}^{\mathrm{T}}\,\mathrm{d}\Omega, \tag{7.9b}$$

$$\boldsymbol{K}_{\Lambda u} = -\int_\Omega \boldsymbol{h} \frac{\partial F}{\partial \boldsymbol{\sigma}} \frac{\mathrm{d}\boldsymbol{\sigma}}{\mathrm{d}\boldsymbol{\epsilon}} \boldsymbol{B}\,\mathrm{d}\Omega, \tag{7.9c}$$

$$\boldsymbol{K}_{\Lambda\Lambda} = -\int_\Omega \left[\left(\frac{\partial F}{\partial \boldsymbol{\sigma}} \frac{\mathrm{d}\boldsymbol{\sigma}}{\mathrm{d}\Lambda} + \frac{\partial F}{\partial \Lambda} \right) \boldsymbol{h}\boldsymbol{h}^{\mathrm{T}} + \frac{\partial F}{\partial \nabla^2 \Lambda} \boldsymbol{h}\boldsymbol{s}^{\mathrm{T}} \right] \mathrm{d}\Omega, \tag{7.9d}$$

$$\boldsymbol{K}_{up} = \int_\Omega \boldsymbol{B}^{\mathrm{T}} \boldsymbol{\Pi} \boldsymbol{N}_p\,\mathrm{d}\Omega, \tag{7.9e}$$

$$\boldsymbol{K}_{pp} = \frac{\Delta t}{\gamma_f} \boldsymbol{H} + \boldsymbol{M}, \tag{7.9f}$$

$$\boldsymbol{H} = \int_\Omega (\boldsymbol{\nabla} \boldsymbol{N}_p)^{\mathrm{T}} \boldsymbol{k} \boldsymbol{\nabla} \boldsymbol{N}_p\,\mathrm{d}\Omega, \tag{7.9g}$$

$$\boldsymbol{M} = \int_\Omega \boldsymbol{N}_p^{\mathrm{T}} \frac{n}{K_f} \boldsymbol{N}_p\,\mathrm{d}\Omega, \tag{7.9h}$$

$$\boldsymbol{f}_{\mathrm{e}} = \int_\Omega \boldsymbol{N}^{\mathrm{T}} \hat{\rho} \boldsymbol{g}\,\mathrm{d}\Omega + \int_{\Gamma_t} \boldsymbol{N}^{\mathrm{T}} \bar{\boldsymbol{t}}\,\mathrm{d}\Gamma, \tag{7.9i}$$

$$\boldsymbol{f}_{\mathrm{i}} = \int_\Omega \left(\boldsymbol{B}^{\mathrm{T}} \boldsymbol{\sigma} - \boldsymbol{B}^{\mathrm{T}} \boldsymbol{\Pi} p_f \right) \mathrm{d}\Omega, \tag{7.9j}$$

$$\boldsymbol{f}_{\Lambda} = \int_\Omega \boldsymbol{h} F(\boldsymbol{\sigma}, \Lambda, \nabla^2 \Lambda)\,\mathrm{d}\Omega, \tag{7.9k}$$

$$\boldsymbol{f}_f = \Delta t \left(-\int_{\Gamma_q} \boldsymbol{N}_p^{\mathrm{T}} \bar{\boldsymbol{q}} \mathrm{d}\Gamma - \boldsymbol{K}_{up}^{\mathrm{T}} \dot{\boldsymbol{u}}^h - \frac{1}{\gamma_f} \boldsymbol{H} \boldsymbol{p}^h - \boldsymbol{M} \dot{\boldsymbol{p}}^h \right). \tag{7.9l}$$

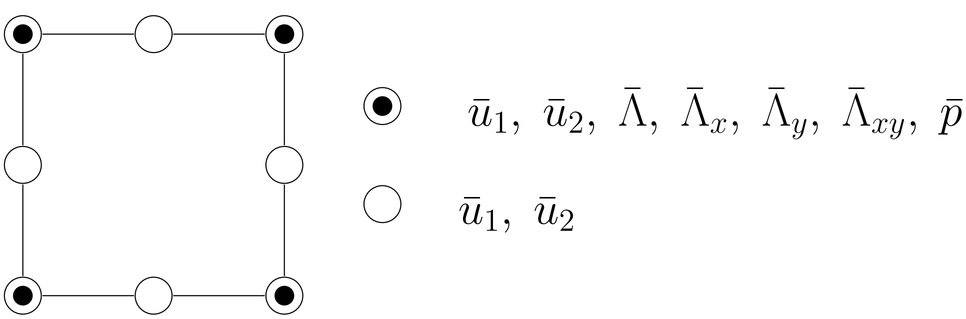

Figure 7.1: Three-field u-p-Λ finite element

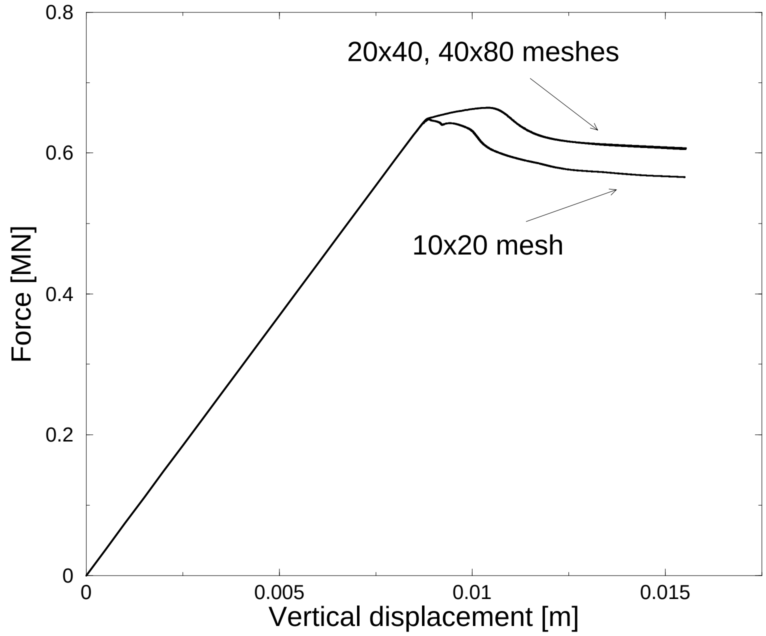

Figure 7.2: Load-deformation curves (regularized Cam-clay model for two-phase medium)

7.2 Localization in biaxial compression for regularized two-phase medium

Again, the biaxial compression test is computed for two-phase medium in which the behaviour of the solid skeleton is described using regularized, gradient-dependent Cam-clay model with $p_{c0} = 2.0$ MPa, g = 0.05 kN^2/m^2 and $k = 1.0$ e-06 m/day. The results for this case are shown in Figs 7.2-7.4. In Fig. 7.2 the results for the coarse mesh are not accurate enough due to standard discretization error. However, the diagrams for the medium and fine mesh almost coincide. The strain and pore pressure distributions in Figs 7.3-7.4 are also mesh independent. This proves that the pathological discretization sensitivity has been removed.

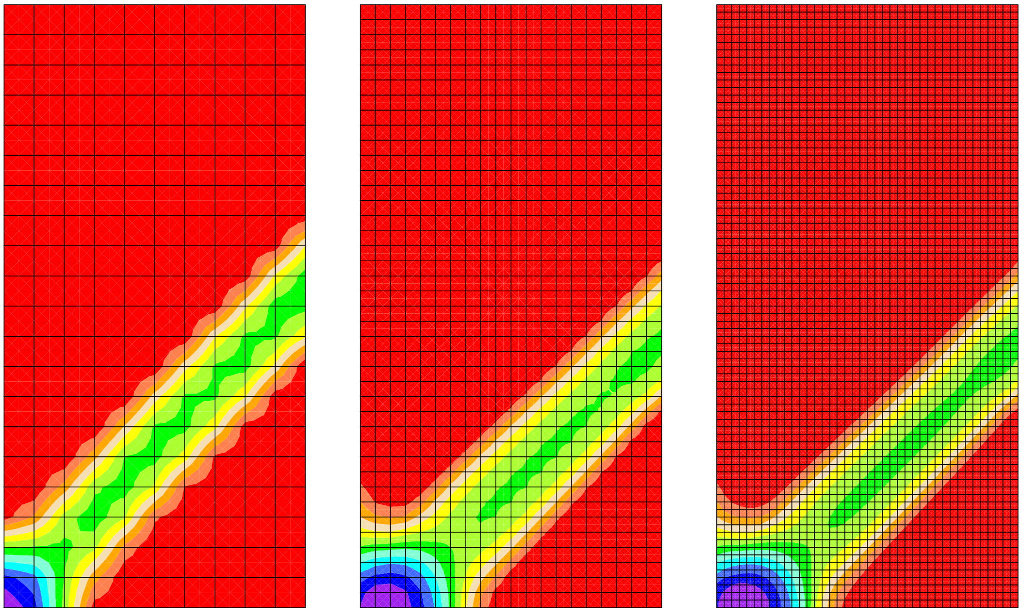

Figure 7.3: Vertical strain distribution (regularized Cam-clay model for two-phase medium)

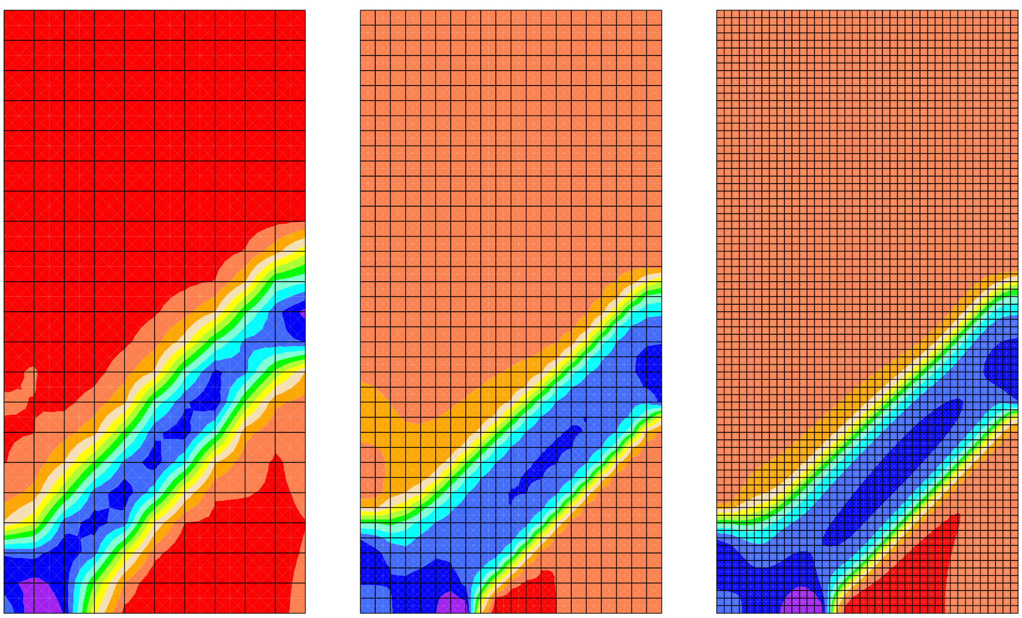

Figure 7.4: Pore pressure distribution (regularized Cam-clay model for two-phase medium)

Chapter 8

Selected applications

The preliminary results of the steep slope stability problem are described in this section. However, it should be emphasized that the application of the implemented material models and finite elements to the numerical simulations of geotechnical benchmarks which involve instabilities and localization is not the main goal of this thesis.

8.1 Steep slope stability - two-phase medium

This numerical test examines a square specimen of soil loaded by a rigid footing. The side length of the configuration is 10m, the rigid footing extends over 7m along the left part of the top surface. The drainage of the pore fluid ($p_f = 0$) is only allowed through the remaining part of the upper surface of the specimen. The geometry, loading and boundary conditions for the displacements and pore pressure are shown in Fig. 8.1. Boundary conditions for the plastic multiplier field constrain the normal and mixed derivatives $\Lambda_{,n}$ and $\Lambda_{,\xi\eta}$ to zero on all the edges. The loading process is performed under displacement control. The vertical displacement of the rigid footing (upper nodes of the sample) is prescribed to load the sample. In fact, since we assume that the footing is infinitely stiff and cannot rotate (but can slide along the top edge), the displacements of the nodes of the sample are prescribed. Three discretizations with 10 $\times$ 10, 20 $\times$ 20 and 40 $\times$ 40 finite elements are considered.

The following material data are adopted: $\nu = 0.2$, $\kappa = 0.013$, $e_0 = 1.0$, $p_c = 640.0$ kPa, $\lambda = 0.032$, $M = 1.1$, $\gamma_f = 10$ kN/m^3, $K_f = 3.0e03$ kPa, $k = 1.0 \times 10^{-4}$ m/day, $g = 1.0e05$ kN^2/m^2.

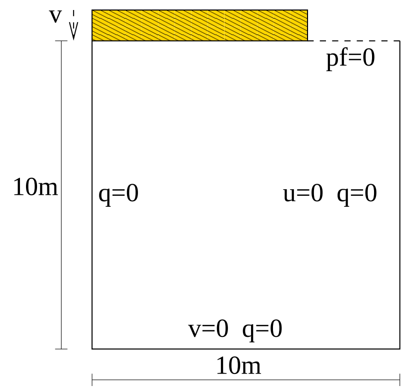

Figure 8.1: Steep slope stability problem: geometry, natural and essential boundary conditions

8.1.1 Steep slope stability (local Cam-clay model)

For a start, the calculations are performed for a two-phase medium and local version of the modified Cam-clay model ($g = 0$). In Figs 8.2-8.5 the results for three meshes are presented. The deformed meshes, strain and pore pressure distribution are plotted at the end of calculations. The lack of the regularization results in the mesh-dependence of the numerical solution. As shown in Figs 8.3 - 8.4 for each mesh strains localize in the narrowest possible area. On the other hand, the pore pressure distributions do not exhibit localization.

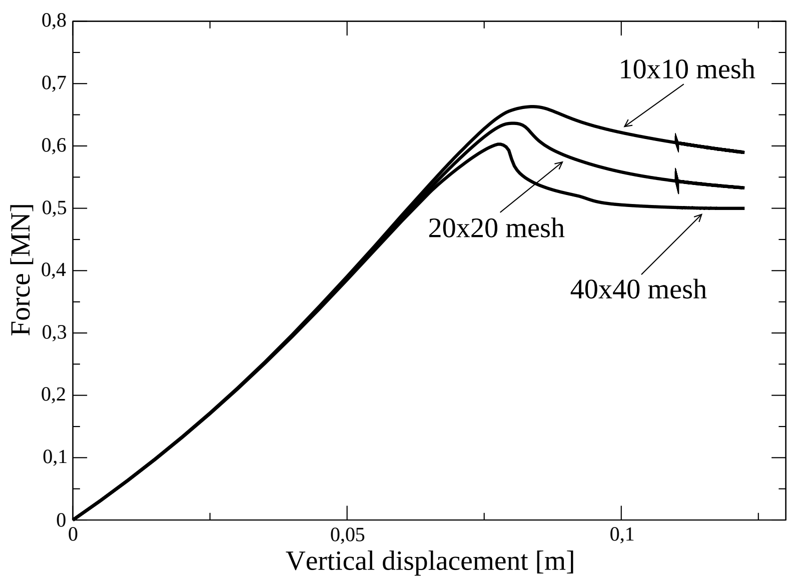

Figure 8.2: Load-deformation curves for local Cam-clay model ($g = 0$)

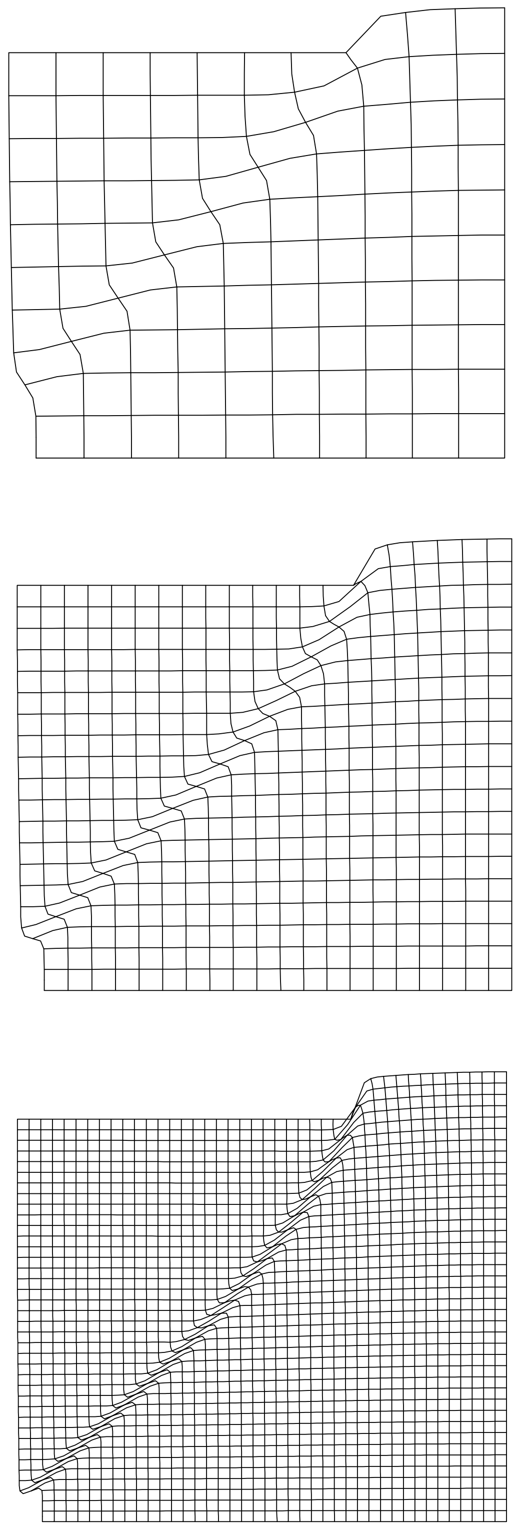

Figure 8.3: Deformed meshes for local model

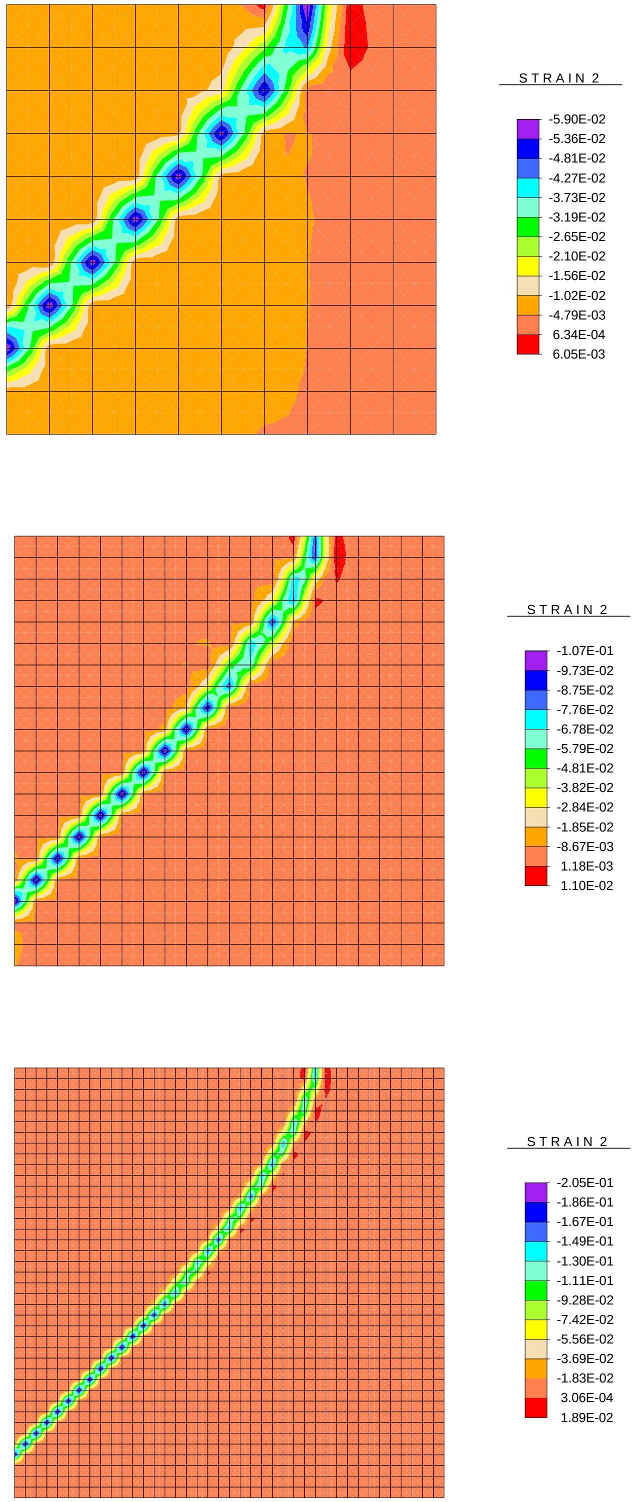

Figure 8.4: Vertical strain distribution for local model

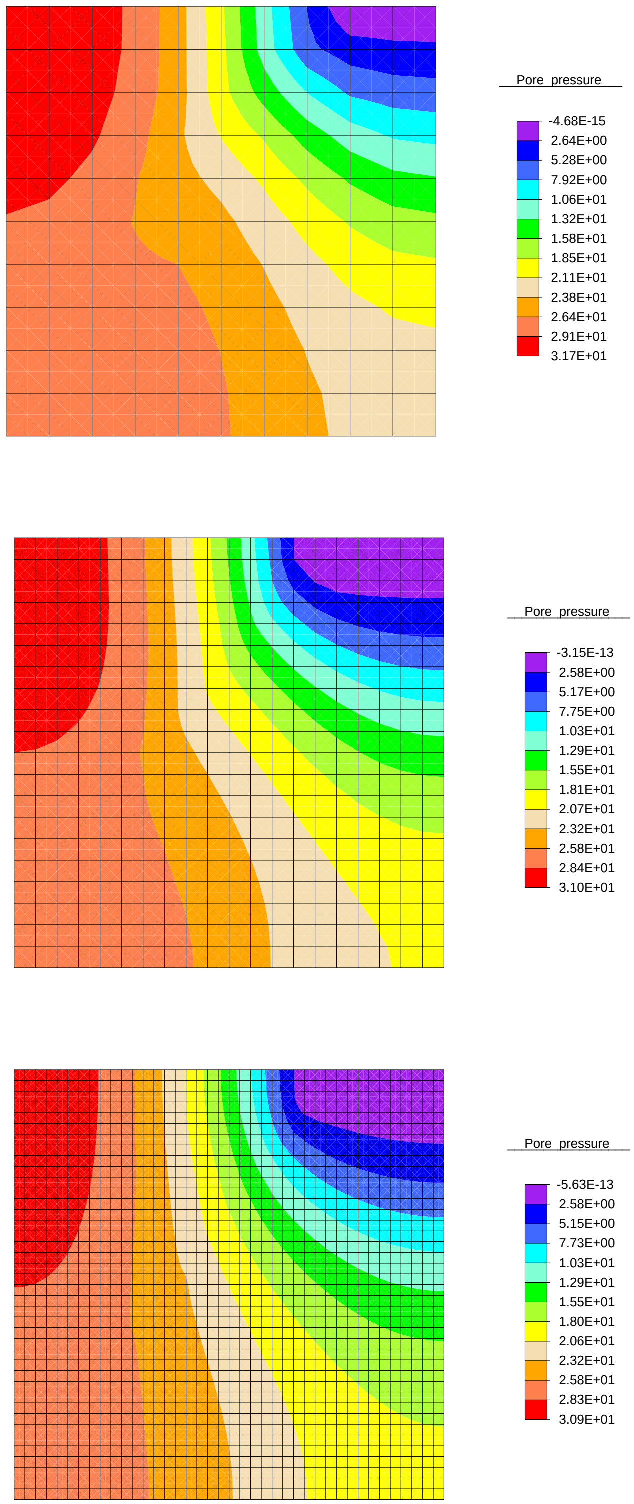

Figure 8.5: Pore pressure distribution for local model

8.1.2 Steep slope stability - regularized two-phase medium

The following results have been obtained for the three-field element. As can be seen in Fig. 8.6 the results for the coarse mesh are not accurate enough due to a standard discretization error. However, the diagrams for the medium and fine mesh almost coincide. In Fig. 8.7 the deformed meshes are shown. Fig. 8.8 and Fig. 8.9 present the strain and pore pressure distribution, respectively. All results are plotted at the end of calculations. The width of the shear band (cf. Fig. 8.7 and Fig. 8.8) is similar for each of the three considered discretizations.

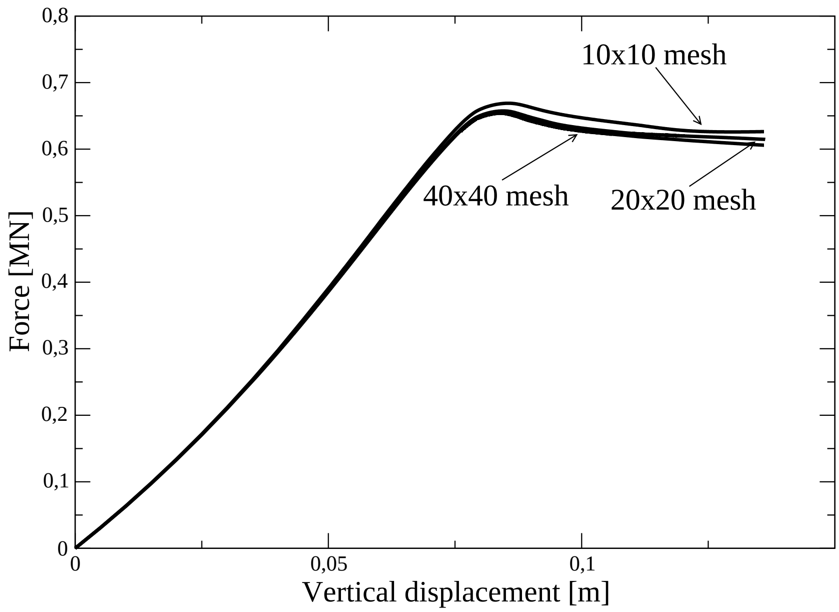

Figure 8.6: Load-deformation curves for gradient-enhanced Cam-clay model $g = 1.0e05$ kN^2/m^2

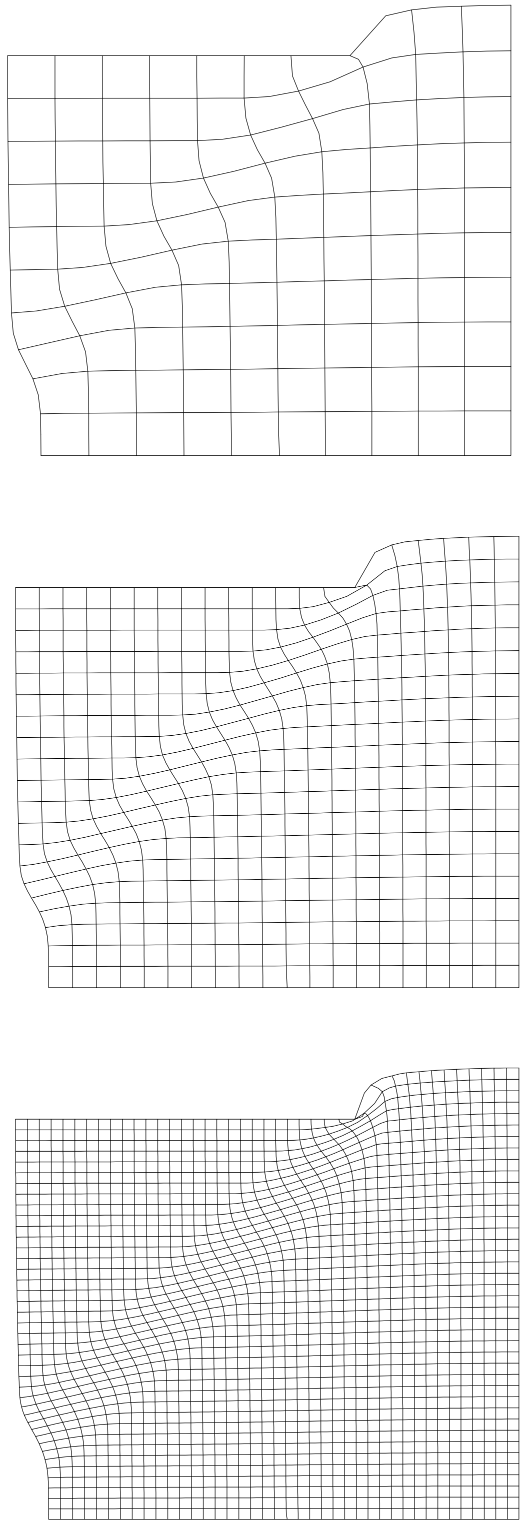

Figure 8.7: Deformed meshes for gradient-enhanced Cam-clay model

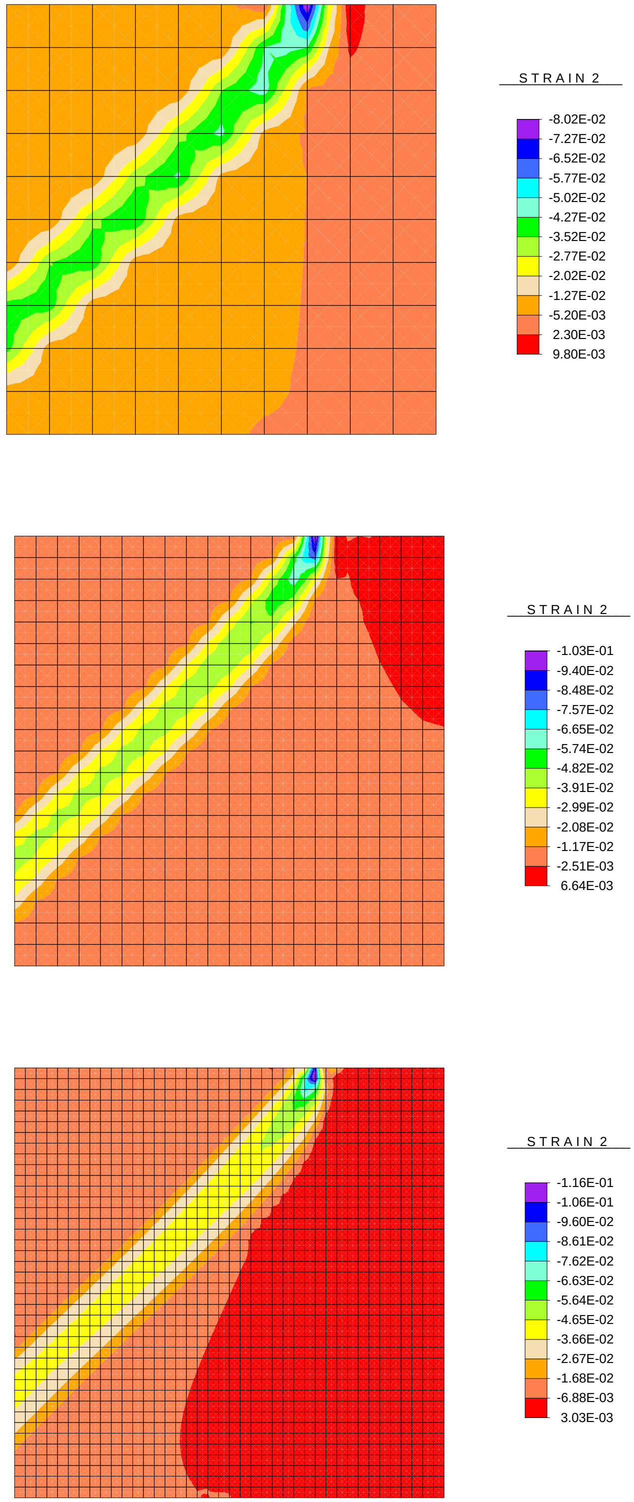

Figure 8.8: Vertical strain distribution for gradient-enhanced Cam-clay model

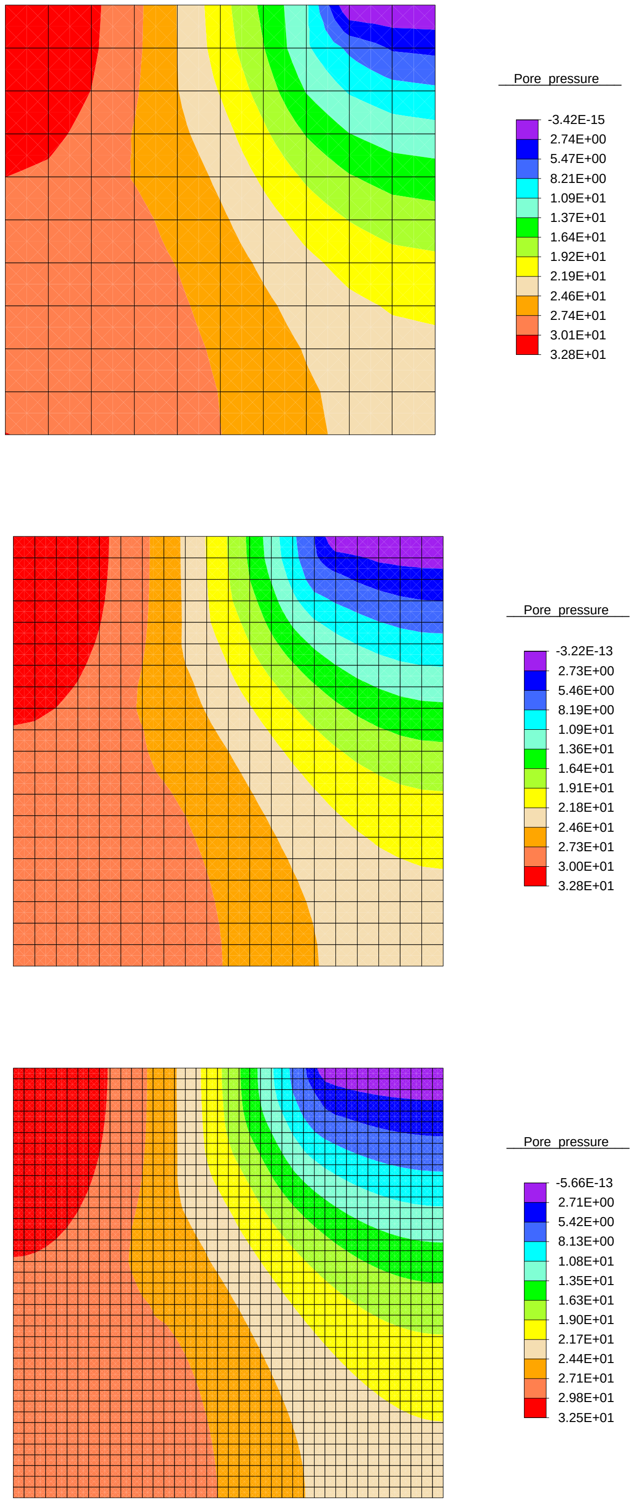

Figure 8.9: Pore pressure distribution for gradient-enhanced Cam-clay model

Chapter 9

Conclusions

In this thesis the numerical analysis of strain and pore pressure localization in one- and two-phase geomaterials has been performed. The modified Cam-clay model and its extensions have been used to describe the behaviour of soil skeleton. First, the response of the model for the limiting cases of undrained soil (approaching incompressible material) and drained soil has been assessed. Then, the general case of two-phase fully saturated medium within a consolidation theory has been analyzed.

For the case of dilatation due to large preconsolidation, strong softening and, in some cases, negative excess pore pressures have been predicted. The analysis of the numerical results leads to the conclusion that, in comparison to a one-phase material the two-phase medium has a lower load-carrying capacity and is in general less stable. Thus, no distinct stabilizing effect of the fluid phase has been observed in the computed examples for the two-phase medium with the soil skeleton described with the local Cam-clay model.

In the biaxial compression test of shear banding, the (inelastic) strain distributions obtained for various values of the permeability coefficient are sensitive to the discretization density. On the other hand, the pore pressure distributions are nearly mesh-independent. However, the pore pressure distribution depends strongly on the value of the permeability coefficient and also on the boundary conditions for the pore pressure field.

The obtained results of numerical simulations do not confirm the statement that the two-phase soil modelling involves a certain regularization by introducing a gradient term present in the Darcy's law. Thus, the necessity of regularization of the constitutive model for a multiphase material has been proved. We conclude that a regularization of the softening and/or nonassociative constitutive model for soil is mandatory also within a two-phase description.

The gradient-enhancement of the modified Cam-clay model has been proposed in the thesis in order to preserve the well-posedness of the governing partial differential equations in the presence of material instabilities. The regularization is based on the incorporation of the Laplacian of the plastic multiplier in the Cam-clay yield function. Consequently, a three field finite element has been proposed for the analysis of instabilities in the consolidation problem of evolving deformations and pore pressures.

The numerical material model and the algorithms have been incorporated into the FEAP finite element package [70]. Although the attention has been focused on the plane strain biaxial compression benchmark, a number of elementary tests and larger scale problems involving unstable (softening) behaviour and localized deformation have also been computed. The performed numerical tests have verified the employed algorithms and their implementation. The ability of the model to simulate a variety of stress states and histories has been demonstrated. Moreover, the results obtained for the gradient-enhanced (regularized) theory and the three-field element do not show the pathological mesh dependence of numerical result due to instabilities and strain localization.

In Sect. 6.1 the alternative concepts of gradient enhancement have been sketched, which should be a subject of further research. The extension of the Cam-clay model to viscoplasticity [8] is also worth implementing since it would enable a further discussion of regularization need and efficiency.

In a future research, the dependence of the yield condition on the Lode angle should be incorporated in the description. The elliptic shape of the yield function could also be distorted like in [23,28] to approximate better the experimental results. In order to extend the possible application of the implemented numerical model, an option of deviatoric hardening should also be introduced in the description.

A numerical analysis of geomaterials is a very strong and practical tool, since general stress states for arbitrary configurations can easily be examined. Extensions of the present implementation to a three-dimensional case or dynamic loading do not seem to pose large difficulties.

Chapter 10

Appendix

Note that in this appendix the preconsolidation pressure p_c is denoted by $2a$.

Derivatives in Newton algorithm for associated Cam-clay plasticity

The Jacobian matrix needed for the Newton-Raphson iteration scheme in eq. (4.26) has the form:

$$\left[\frac{\partial \boldsymbol{r}}{\partial \boldsymbol{s}}\right] = \begin{bmatrix} \frac{\partial r_1}{\partial p} & \frac{\partial r_1}{\partial q} & \frac{\partial r_1}{\partial \bar{G}} & \frac{\partial r_1}{\partial a} & \frac{\partial r_1}{\partial \Delta\Lambda} \\ \frac{\partial r_2}{\partial p} & \frac{\partial r_2}{\partial q} & \frac{\partial r_2}{\partial \bar{G}} & \frac{\partial r_2}{\partial a} & \frac{\partial r_2}{\partial \Delta\Lambda} \\ \frac{\partial r_3}{\partial p} & \frac{\partial r_3}{\partial q} & \frac{\partial r_3}{\partial \bar{G}} & \frac{\partial r_3}{\partial a} & \frac{\partial r_3}{\partial \Delta\Lambda} \\ \frac{\partial r_4}{\partial p} & \frac{\partial r_4}{\partial q} & \frac{\partial r_4}{\partial \bar{G}} & \frac{\partial r_4}{\partial a} & \frac{\partial r_4}{\partial \Delta\Lambda} \\ \frac{\partial r_5}{\partial p} & \frac{\partial r_5}{\partial q} & \frac{\partial r_5}{\partial \bar{G}} & \frac{\partial r_5}{\partial a} & \frac{\partial r_5}{\partial \Delta\Lambda} \end{bmatrix} \tag{10.1}$$

with the following derivatives:

$\frac{\partial r_1}{\partial p} = 1 + 2\frac{1+e_0}{\kappa} M^2 \Delta\Lambda p_0 \exp\left[-\frac{1+e_0}{\kappa}\Delta\theta^{\mathrm{e}}\right]$
$\frac{\partial r_1}{\partial q} = 0$
$\frac{\partial r_1}{\partial \bar{G}} = 0$
$\frac{\partial r_1}{\partial a} = -\frac{\partial r_1}{\partial p} + 1$
$\frac{\partial r_1}{\partial \Delta\Lambda} = 2\frac{1+e_0}{\kappa} M^2 (p-a) p_0 \exp\left[-\frac{1+e_0}{\kappa}\Delta\theta^{\mathrm{e}}\right]$

$\frac{\partial r_2}{\partial p} = 0$
$\frac{\partial r_2}{\partial q} = 1$
$\frac{\partial r_2}{\partial \bar{G}} = -\frac{3\boldsymbol{\xi}^T_{trial}\Delta\boldsymbol{\gamma}}{q_{trial}(1+6\bar{G}\Delta\Lambda)} + \frac{6\Delta\Lambda q_{trial}}{(1+6\bar{G}\Delta\Lambda)^2}$
$\frac{\partial r_2}{\partial a} = 0$

$\frac{\partial r_2}{\partial \Delta\Lambda} = \frac{6\bar{G}q_{trial}}{(1+6\bar{G}\Delta\Lambda)^2}$

$\frac{\partial r_3}{\partial p} = -\frac{2\frac{3}{2}\frac{1-2\nu}{1+\nu}\frac{1+e_0}{\kappa}M^2\Delta\Lambda p_0 \exp\left[-\frac{1+e_0}{\kappa}\Delta\theta^{\mathrm{e}}\right]}{\Delta\theta^{\mathrm{e}}} + \frac{2\frac{3}{2}\frac{1-2\nu}{1+\nu}M^2\Delta\Lambda p_0(1-\exp\left[-\frac{1+e_0}{\kappa}\Delta\theta^{\mathrm{e}}\right])}{\Delta\theta^{\mathrm{e}2}}$
$\frac{\partial r_3}{\partial q} = 0$
$\frac{\partial r_3}{\partial \bar{G}} = 1$
$\frac{\partial r_3}{\partial a} = -\frac{\partial r_3}{\partial p}$
$\frac{\partial r_3}{\partial \Delta\Lambda} = -\frac{2\frac{3}{2}\frac{1-2\nu}{1+\nu}\frac{1+e_0}{\kappa}M^2(p-a)p_0 \exp\left[-\frac{1+e_0}{\kappa}\Delta\theta^{\mathrm{e}}\right]}{\Delta\theta^{\mathrm{e}}} + \frac{2\frac{3}{2}\frac{1-2\nu}{1+\nu}M^2(p-a)p_0(1-\exp\left[-\frac{1+e_0}{\kappa}\Delta\theta^{\mathrm{e}}\right])}{\Delta\theta^{\mathrm{e}2}}$

A special case must be considered for $\Delta\theta^{\mathrm{e}} \to 0$:

$\frac{\partial r_3}{\partial p} = \frac{3}{2}\frac{1-2\nu}{1+\nu}\left(\frac{1+e_0}{\kappa}\right)^2 M^2\Delta\Lambda p_0$
$\frac{\partial r_3}{\partial a} = -\frac{\partial r_3}{\partial p}$
$\frac{\partial r_3}{\partial \Delta\Lambda} = \frac{3}{2}\frac{1-2\nu}{1+\nu}\left(\frac{1+e_0}{\kappa}\right)^2 M^2(p-a)p_0$

$\frac{\partial r_4}{\partial p} = -2\frac{1+e_0}{\lambda-\kappa}M^2\Delta\Lambda a_0 \exp\left[-\frac{1+e_0}{\lambda-\kappa}\Delta\theta^{\mathrm{p}}\right]$
$\frac{\partial r_4}{\partial q} = 0$
$\frac{\partial r_4}{\partial \bar{G}} = 0$
$\frac{\partial r_4}{\partial a} = -\frac{\partial r_4}{\partial p} + 1$
$\frac{\partial r_4}{\partial \Delta\Lambda} = -2\frac{1+e_0}{\lambda-\kappa}M^2(p-a)a_0 \exp\left[-\frac{1+e_0}{\lambda-\kappa}\Delta\theta^{\mathrm{p}}\right]$

$\frac{\partial r_5}{\partial p} = 2M^2(p-a)$
$\frac{\partial r_5}{\partial q} = 2q$
$\frac{\partial r_5}{\partial \bar{G}} = 0$
$\frac{\partial r_5}{\partial a} = -2M^2 p$
$\frac{\partial r_5}{\partial \Delta\Lambda} = 0$

In order to calculate the consistent tangent operator the following matrices are required:

- the derivative of deviatoric stress $\boldsymbol{\xi}$ with respect to strain $\boldsymbol{\epsilon}$

$$\left[\frac{\partial \boldsymbol{\xi}}{\partial \boldsymbol{\epsilon}}\right] == \frac{2\bar{G}}{1+6\bar{G}\Delta\Lambda}\boldsymbol{R}^{-1}\boldsymbol{Q} \tag{10.2}$$

- the derivative of function f_p describing the change of hydrostatic pressure: $p = f_p(p) = p_0 \exp\left[-\frac{1+e_0}{\kappa}\Delta\theta^{\mathrm{e}}(p)\right]$ with respect to strain $\boldsymbol{\epsilon}$

$$\left[\frac{\partial f_p}{\partial \boldsymbol{\epsilon}}\right] = \left[\begin{array}{cccccc} \frac{\partial f_p}{\partial \epsilon_1} & \frac{\partial f_p}{\partial \epsilon_2} & \frac{\partial f_p}{\partial \epsilon_3} & \frac{\partial f_p}{\partial \epsilon_4} & \frac{\partial f_p}{\partial \epsilon_5} & \frac{\partial f_p}{\partial \epsilon_6} \end{array}\right] = \left[\begin{array}{cccccc} -K_t & -K_t & -K_t & 0 & 0 & 0 \end{array}\right] \quad (10.3)$$

- the derivative of deviatoric stress $\boldsymbol{\xi}$ with respect to vector of primary unknowns $\boldsymbol{s}$ – 6 $\times$ 5 matrix with columns defined as

$$\left[\frac{\partial \boldsymbol{\xi}}{\partial \boldsymbol{s}}\right] = \left[\begin{array}{ccccc} \frac{\partial \boldsymbol{\xi}}{\partial p} & \frac{\partial \boldsymbol{\xi}}{\partial q} & \frac{\partial \boldsymbol{\xi}}{\partial \bar{G}} & \frac{\partial \boldsymbol{\xi}}{\partial a} & \frac{\partial \boldsymbol{\xi}}{\partial \Delta\Lambda} \end{array}\right] \quad (10.4)$$

$\frac{\partial \boldsymbol{\xi}}{\partial p} = \mathbf{0}$
$\frac{\partial \boldsymbol{\xi}}{\partial q} = \mathbf{0}$
$\frac{\partial \boldsymbol{\xi}}{\partial \bar{G}} = \frac{2\boldsymbol{R}^{-1}\Delta\boldsymbol{\gamma}}{1+6\bar{G}\Delta\Lambda} - \frac{6\Delta\Lambda\boldsymbol{\xi}_{trial}}{(1+6\bar{G}\Delta\Lambda)^2}$
$\frac{\partial \boldsymbol{\xi}}{\partial a} = \mathbf{0}$
$\frac{\partial \boldsymbol{\xi}}{\partial \Delta\Lambda} = -\frac{6\bar{G}\boldsymbol{\xi}_{trial}}{(1+6\bar{G}\Delta\Lambda)^2}$

- the derivative of function f_p with respect to vector of primary unknowns $\boldsymbol{s}$

$$\left[\frac{\partial f_p}{\partial \boldsymbol{s}}\right] = \left[\begin{array}{ccccc} \frac{\partial f_p}{\partial p} & \frac{\partial f_p}{\partial q} & \frac{\partial f_p}{\partial \bar{G}} & \frac{\partial f_p}{\partial a} & \frac{\partial f_p}{\partial \Delta\Lambda} \end{array}\right] \quad (10.5)$$

$\frac{\partial f_p}{\partial p} = -2\frac{1+e_0}{\kappa}M^2\Delta\Lambda p_0 \exp\left[-\frac{1+e_0}{\kappa}\Delta\theta^{\mathrm{e}}\right] = -2\frac{1+e_0}{\kappa}M^2\Delta\Lambda p$
$\frac{\partial f_p}{\partial q} = 0$
$\frac{\partial f_p}{\partial \bar{G}} = 0$
$\frac{\partial f_p}{\partial a} = -\frac{\partial p}{\partial p}$
$\frac{\partial f_p}{\partial \Delta\Lambda} = -2\frac{1+e_0}{\kappa}M^2(p-a)p_0 \exp\left[-\frac{1+e_0}{\kappa}\Delta\theta^{\mathrm{e}}\right] = -2\frac{1+e_0}{\kappa}M^2(p-a)p$

- the derivative of vector of residuals $\boldsymbol{r}$ with respect to strain $\boldsymbol{\epsilon}$ – 5 $\times$ 6 matrix with rows defined as

$$\left[\frac{\partial \boldsymbol{r}}{\partial \boldsymbol{\epsilon}}\right] = \left[\begin{array}{ccccc} \frac{\partial r_1}{\partial \boldsymbol{\epsilon}} & \frac{\partial r_2}{\partial \boldsymbol{\epsilon}} & \frac{\partial r_3}{\partial \boldsymbol{\epsilon}} & \frac{\partial r_4}{\partial \boldsymbol{\epsilon}} & \frac{\partial r_5}{\partial \boldsymbol{\epsilon}} \end{array}\right]^{\mathrm{T}} \quad (10.6)$$

$\frac{\partial r_1}{\partial \boldsymbol{\epsilon}} = K_t\mathbf{\Pi}^T$
$\frac{\partial r_2}{\partial \boldsymbol{\epsilon}} = -\frac{3\boldsymbol{\xi}_{trial}^T\bar{G}}{q_{trial}(1+6\bar{G}\Delta\Lambda)}\boldsymbol{Q}$
$\frac{\partial r_3}{\partial \boldsymbol{\epsilon}} = -\frac{3}{2}\frac{1-2\nu}{1+\nu}\left(\frac{K_t}{\Delta\theta^{\mathrm{e}}} + \frac{p-p_0}{\Delta\theta^{\mathrm{e}2}}\right)\mathbf{\Pi}^T$

for $\Delta\theta^{\mathrm{e}} \rightarrow 0$

$\frac{\partial r_3}{\partial \boldsymbol{\epsilon}} = \frac{3}{4}\frac{1-2\nu}{1+\nu}\left(\frac{1+e_0}{\kappa}\right)^2 p_0\mathbf{\Pi}^T$
$\frac{\partial r_4}{\partial \boldsymbol{\epsilon}} = \mathbf{0}$
$\frac{\partial r_5}{\partial \boldsymbol{\epsilon}} = \mathbf{0}$

Derivatives in Newton algorithm for non-associated Cam-clay plasticity

The derivatives in the Jacobian matrix:

$$\frac{\partial r_1}{\partial p} = 1 + \frac{1+e_0}{\kappa}(M^2 - \bar{M}^2)\Delta\Lambda p_0 \exp\left[-\frac{1+e_0}{\kappa}\Delta\theta^{\mathrm{e}}\right]$$

$$\frac{\partial r_1}{\partial a} = -2\frac{1+e_0}{\kappa}M^2\Delta\Lambda p_0 \exp\left[-\frac{1+e_0}{\kappa}\Delta\theta^{\mathrm{e}}\right]$$

$$\frac{\partial r_1}{\partial \Delta\Lambda} = \frac{1+e_0}{\kappa}(M^2(p-2a) + \bar{M}^2 p)p_0 \exp\left[-\frac{1+e_0}{\kappa}\Delta\theta^{\mathrm{e}}\right]$$

$$\frac{\partial r_3}{\partial p} = -\frac{\frac{3}{2}\frac{1-2\nu}{1+\nu}\frac{1+e_0}{\kappa}(M^2+\bar{M}^2)\Delta\Lambda p_0 \exp\left[-\frac{1+e_0}{\kappa}\Delta\theta^{\mathrm{e}}\right]}{\Delta\theta^{\mathrm{e}}} + \frac{\frac{3}{2}\frac{1-2\nu}{1+\nu}(M^2+\bar{M}^2)\Delta\Lambda p_0(1-\exp\left[-\frac{1+e_0}{\kappa}\Delta\theta^{\mathrm{e}}\right])}{\Delta\theta^{\mathrm{e}2}}$$

$$\frac{\partial r_3}{\partial a} = \frac{2\frac{3}{2}\frac{1-2\nu}{1+\nu}\frac{1+e_0}{\kappa}M^2\Delta\Lambda p_0 \exp\left[-\frac{1+e_0}{\kappa}\Delta\theta^{\mathrm{e}}\right]}{\Delta\theta^{\mathrm{e}}} - \frac{2\frac{3}{2}\frac{1-2\nu}{1+\nu}M^2\Delta\Lambda p_0(1-\exp\left[-\frac{1+e_0}{\kappa}\Delta\theta^{\mathrm{e}}\right])}{\Delta\theta^{\mathrm{e}2}}$$

$$\frac{\partial r_3}{\partial \Delta\Lambda} = -\frac{\frac{3}{2}\frac{1-2\nu}{1+\nu}\frac{1+e_0}{\kappa}(M^2(p-2a)+\bar{M}^2 p)p_0 \exp\left[-\frac{1+e_0}{\kappa}\Delta\theta^{\mathrm{e}}\right]}{\Delta\theta^{\mathrm{e}}} + \frac{\frac{3}{2}\frac{1-2\nu}{1+\nu}(M^2(p-2a)+\bar{M}^2 p)p_0(1-\exp\left[-\frac{1+e_0}{\kappa}\Delta\theta^{\mathrm{e}}\right])}{\Delta\theta^{\mathrm{e}2}}$$

A special case must be considered for $\Delta\theta^{\mathrm{e}} \to 0$:

$$\frac{\partial r_3}{\partial p} = \frac{1}{2}\frac{3}{2}\frac{1-2\nu}{1+\nu}\left(\frac{1+e_0}{\kappa}\right)^2(M^2 + \bar{M}^2)\Delta\Lambda p_0$$

$$\frac{\partial r_3}{\partial a} = -\frac{3}{2}\frac{1-2\nu}{1+\nu}\left(\frac{1+e_0}{\kappa}\right)^2 M^2\Delta\Lambda p_0$$

$$\frac{\partial r_3}{\partial \Delta\Lambda} = \frac{1}{2}\frac{3}{2}\frac{1-2\nu}{1+\nu}\left(\frac{1+e_0}{\kappa}\right)^2(M^2(p-2a) + \bar{M}^2)p_0$$

$$\frac{\partial r_4}{\partial p} = -2\frac{1+e_0}{\lambda-\kappa}(M^2 + \bar{M}^2)\Delta\Lambda a_0 \exp\left[-\frac{1+e_0}{\lambda-\kappa}\Delta\theta^{\mathrm{p}}\right]$$

$$\frac{\partial r_4}{\partial a} = 1 + 2\frac{1+e_0}{\lambda-\kappa}M^2\Delta\Lambda a_0 \exp\left[-\frac{1+e_0}{\lambda-\kappa}\Delta\theta^{\mathrm{p}}\right]$$

$$\frac{\partial r_4}{\partial \Delta\Lambda} = -\frac{1+e_0}{\lambda-\kappa}(M^2(p-2a) + \bar{M}^2 p)a_0 \exp\left[-\frac{1+e_0}{\lambda-\kappa}\Delta\theta^{\mathrm{p}}\right]$$

The derivatives of function f_p with respect to the components of vector of primary unknowns $\boldsymbol{s}$:

$$\frac{\partial f_p}{\partial p} = -\frac{1+e_0}{\kappa}(M^2 + \bar{M}^2)\Delta\Lambda p_0 \exp\left[-\frac{1+e_0}{\kappa}\Delta\theta^{\mathrm{e}}\right] = -\frac{1+e_0}{\kappa}(M^2 + \bar{M}^2)\Delta\Lambda p$$

$$\frac{\partial f_p}{\partial a} = 2\frac{1+e_0}{\kappa}M^2\Delta\Lambda p_0 \exp\left[-\frac{1+e_0}{\kappa}\Delta\theta^{\mathrm{e}}\right] = 2\frac{1+e_0}{\kappa}M^2\Delta\Lambda p$$

$$\frac{\partial f_p}{\partial \Delta\Lambda} = -\frac{1+e_0}{\kappa}(M^2(p-2a) + \bar{M}^2 p)p_0 \exp\left[-\frac{1+e_0}{\kappa}\Delta\theta^{\mathrm{e}}\right] = -\frac{1+e_0}{\kappa}(M^2(p-2a) + \bar{M}^2 p)p$$

The derivatives have been computed analytically using Maple 7.0, and verified with the finite difference method.

Bibliography

[1] E.C. Aifantis. Gradient deformation models at nano, micro, and macro scales. *ASME J. Eng. Mat. Tech.*, 121:189–202, 1999.

[2] H. Askes, A.S.J. Suiker, and L.J. Sluys. A classification of higher-order strain-gradient models - linear analysis. *Archive of Applied Mechanics*, 72(2-3):171–188, 2002.

[3] J.P. Bardet and A. Shiv. Plane-strain instability of saturated porous media. *ASCE J. Eng. Mech.*, 121(6):717–724, 1995.

[4] Z.P. Bažant and G. Pijaudier-Cabot. Nonlocal continuum damage, localization instability and convergence. *ASME J. Appl. Mech.*, 55:287–293, 1988.

[5] A. Benallal and C. Comi. On numerical analyses in the presence of unstable saturated porous materials. *Int. J. Numer. Methods Engng*, 56(6):883–910, 2003.

[6] R. Borja. Cam-Clay plasticity. Part II: Implicit integration of constitutive equations based on a nonlinear elastic stress predictor. *Comput. Meth. Appl. Mech. Eng.*, 88:225–240, 1991.

[7] R. Borja. Cam-Clay plasticity. Part V: A mathematical framework for three-phase deformation and strain localization analyses of partially saturated porous media. *Comput. Meth. Appl. Mech. Eng.*, 193:5301–5338, 2004.

[8] V.D. da Silva. Viscoplastic regularization of a Cam-Clay FE-implementation. In Wunderlich [85], pages 250–251, paper no. 422.

[9] R.O. Davis and A.P.S. Selvadurai. *Plasticity and Geomechanics*. Cambridge University Press, Cambridge, 2002.

[10] R. de Borst. Integration of plasticity equations for singular yield functions. *Comput. Struct.*, 26:823–829, 1987.

[11] R. de Borst and M.-A. Abellan. Dispersion and internal length scales in strain-softenig two-phase media. In G. Meschke et al., editors, *Proc. EURO-C 2006 Int. Conf. Computational Modelling of Concrete Structures*, pages 549–556, London/Leiden, 2006. Taylor & Francis.

[12] R. de Borst and H.-B. Mühlhaus. Gradient-dependent plasticity: Formulation and algorithmic aspects. *Int. J. Numer. Methods Engng*, 35:521–539, 1992.

[13] R. de Borst and J. Pamin. Some novel developments in finite element procedures for gradient-dependent plasticity. *Int. J. Numer. Methods Engng*, 39:2477–2505, 1996.

[14] R. de Borst, J. Pamin, R.H.J. Peerlings, and L.J. Sluys. On gradient-enhanced damage and plasticity models for failure in quasi-brittle and frictional materials. *Computational Mechanics*, 17:130–141, 1995.

[15] R. de Borst, L.J. Sluys, H.-B. Mühlhaus, and J. Pamin. Fundamental issues in finite element analyses of localization of deformation. *Eng. Comput.*, 10:99–121, 1993.

[16] R. de Borst and E. van der Giessen, editors. *Material Instabilities in Solids*, Chichester, 1998. IUTAM, John Wiley & Sons.

[17] W. Ehlers and W. Volk. On theoretical and numerical methods in the theory of porous media based on polar and non-polar elasto-plastic solid materials. *Int. J. Solids Struct.*, 35(34-35):4597–4617, 1998.

[18] R.A.B. Engelen, M.G.D. Geers, and F.P.T. Baaijens. Gradient-enhanced plasticity formulations based on the dependency of the yield stress on a nonlocal field variable. In Wunderlich [85], pages 854–855, paper no. 256.

[19] R.A.B. Engelen, M.G.D. Geers, and F.P.T. Baaijens. Nonlocal implicit gradient-enhanced elasto-plasticity for the modelling of softening behaviour. *Int. J. Plast.*, 19(4):403–433, 2003.

[20] A. Gens and D.M. Potts. Critical state models in computational geomechanics. *Eng. Comput.*, 5:178–197, 1988.

[21] A. Glema and T. Łodygowski. On importance of imperfections in plastic strain localization problems in materials under impact loading. *Arch. Mech.*, 54(5-6):411–423, 2002.

[22] A. Groen. *Three-dimensional elasto-plastic analysis of soils*. Ph.D. dissertation, Delft University of Technology, Delft, 1997.

[23] A.E. Groen, R. de Borst, and S.J.M. van Eekelen. An elastoplastic model for clay: Formulation and algorithmic aspects. In G.N. Pande and S. Pietruszczak, editors, *Numerical models in geomechanics*, pages 121–126, Rotterdam/Brookfield, 1995. Proc. NUMOG V, A.A. Balkema.

[24] M. Gryczmański. Introduction to elasto-plastic soil models (in polish). Technical report, IFTR, PAS, Warsaw, 1995.

[25] O.M. Heeres. *Modern strategies for the numerical modelling of the cyclic and transient behaviour of soils*. Ph.D. dissertation, Delft University of Technology, Delft, 2001.

[26] R. Hill. A general theory of uniqueness and stability in elastic-plastic solids. *J. Mech. Phys. Solids*, 6:236–249, 1958.

[27] T.J.R. Hughes. *The Finite Element Method. Linear Static and Dynamic Analysis*. Prentice-Hall, New Jersey, 1987.

[28] L. Jacobsson and K. Runesson. Integration and calibration of a plasticity model for granular materials. *Int. J. Num. Anal. Meth. Geomech.*, 26:259–272, 2002.

[29] S. Krenk. Family of invariant stress surfaces. *ASCE J. Eng. Mech.*, 122(3):201–208, 1996.

[30] M. Lambrecht and C. Miehe. A note on formulas for localized failure of frictional materials in compression and biaxial loading modes. *Int. J. Num. Anal. Meth. Geomech.*, 25:955–971, 2001.

[31] J. Larsson. *On the modeling of porous media with emphasis on localization*. Ph.D. dissertation, Chalmers University of Technology, Gothenburg, 1999.

[32] R. Larsson and K. Runesson. Element-embedded localization band based on regularized displacement discontinuity. *ASCE J. Eng. Mech.*, 122(5):402–411, 1996.

[33] R.W. Lewis and B.A. Schrefler. *The Finite Element Method in the Static and Dynamic Deformation and Consolidation of Porous Media*. J. Wiley & Sons, second edition, 1998.

[34] Scarpas A. Liu, X. and Blaauwendraad J. Numerical modelling of nonlinear response of soil. part 2: Strain localization investigation on sand. *Int. J. Solids Struct.*, 42:1883–1907, 2005.

[35] B. Loret and O. Harireche. Acceleration waves, flutter instabilities and stationary discontinuities in inelastic porous media. *J. Mech. Phys. Solids*, 39(5):569–606, 1991.

[36] B. Loret and J.H. Prevost. Dynamic strain localization in fluid-saturated porous materials. *ASCE J. Eng. Mech.*, 11:907–922, 1991.

[37] G. Maier and T. Hueckel. Nonassociated and coupled flow rules of elastoplasticity for rock-like materials. *Int. J. Rock Mech. Min. Sci. & Geomech. Abstr.*, 16:77–92, 1979.

[38] Z. Mróz. On forms of constitutive laws for elastic-plastic solids. *Arch. Mech.*, 18:3–34, 1966.

[39] H.-B. Mühlhaus and E.C. Aifantis. A variational principle for gradient plasticity. *Int. J. Solids Struct.*, 28:845–857, 1991.

[40] H.-B. Mühlhaus and I. Vardoulakis. The thickness of shear bands in granular materials. *Geotechnique*, 37:271–283, 1987.

[41] M.K. Neilsen and H.L. Schreyer. Bifurcations in elastic-plastic materials. *Int. J. Solids Struct.*, 30:521–544, 1993.

[42] F. Oka, Y. Higo, and S. Kimoto. Effect of dilatancy on the strain localization of water-saturated elasto-viscoplastic soil. *Int. J. Solids Struct.*, (39):3625–3647, 2002.

[43] M. Ortiz, Y. Leroy, and A. Needleman. A finite element method for localized failure analysis. *Comput. Meth. Appl. Mech. Eng.*, 61:189–214, 1987.

[44] M. Ortiz and A. Pandolfi. A variational Cam-clay theory of plasticity. *Comput. Meth. Appl. Mech. Eng.*, 193:2645–2666, 2004.

[45] N.S. Ottosen and K. Runesson. Properties of discontinuous bifurcation solutions in elasto-plasticity. *Int. J. Solids Struct.*, 27(4):401–421, 1991.

[46] J. Pamin. *Gradient-dependent plasticity in numerical simulation of localization phenomena*. Ph.D. dissertation, Delft University of Technology, Delft, 1994.

[47] J. Pamin. Gradient-enhanced continuum models: formulation, discretization and applications. Technical Report Series Civil Engineering, Monograph 301, Cracow University of Technology, Cracow, 2004.

[48] J. Pamin. Numerical models of localized deformations (in Polish). In Biliński W. and Piszczek K., editors, *Proc. XVII Conf. Computer Methods in Design and Analysis of Hydrostructures*, pages 77–86, Cracow, 2005. Cracow University of Technology, Drukarnia „GS”.

[49] J. Pamin, H. Askes, and R. de Borst. An element-free Galerkin method for gradient plasticity. In Wunderlich [85], pages 854–855, paper no. 345.

[50] J. Pamin, H. Askes, and R. de Borst. Two gradient plasticity theories discretized with the element-free Galerkin method. *Comput. Meth. Appl. Mech. Eng.*, 192:2377–2403, 2003.

[51] A. Pérez-Foguet, A. Rodriguez-Ferran, and A. Huerta. Numerical differentiation for local and global tangent operators in computational plasticity. *Comput. Meth. Appl. Mech. Eng.*, 189(1):277–296, 2000.

[52] A. Pérez-Foguet, A. Rodriguez-Ferran, and A. Huerta. Numerical differentiation for non-trivial consistent tangent matrices: an application to the MRS-Lade model. *Int. J. Numer. Methods Engng*, 48(2):159–184, 2000.

[53] P. Perzyna, editor. *Localization and fracture phenomena in inelastic solids*, Wien - New York, 1998. CISM Course Lecture Notes No. 386, Springer-Verlag.

[54] H. Petryk, editor. *Material instabilities in elastic and plastic solids*, Wien - New York, 2000. CISM Course Lecture Notes No. 414, Springer-Verlag.

[55] P.M. Pinsky. A finite element formulation for elastoplasticity based on three-field variational equation. *Comput. Meth. Appl. Mech. Eng.*, 61:41–60, 1987.

[56] S. Ramaswamy and N. Aravas. Finite element implementation of gradient plasticity models. Part I: Gradient-dependent yield functions, Part II: Gradient-dependent evolution equations. *Comput. Meth. Appl. Mech. Eng.*, 163:11–32,33–53, 1998.

[57] H.E. Read and G.A. Hegemier. Strain softening of rock, soil and concrete - a review article. *Mech. Mater.*, 3:271–294, 1984.

[58] K.H. Roscoe and J.B. Burland. On the generalized behaviour of 'wet' clay. In *Engineering plasticity*, volume 48, pages 535–609, Cambridge, 1968. Cambridge University Press.

[59] J.W. Rudnicki. Diffusive instabilities in dilating and compacting geomaterials. *Multiscale Deformation and Fracture in Materials and Structures*, pages 159–182, 2000.

[60] J.W. Rudnicki and J.R. Rice. Conditions for the localization of deformation in pressure-sensitive dilatant materials. *J. Mech. Phys. Solids*, 23:371–394, 1975.

[61] B.A. Schrefler, C.E. Majorana, and L. Sanavia. Shear band localization in saturated porous media. *Arch. Mech.*, 47:577–599, 1995.

[62] B.A. Schrefler, L. Sanavia, and C.E. Majorana. A multiphase medium model for localisation and postlocalisation simulation in geomechanics. *Mech. Cohes.-frict. Mater.*, 1:95–114, 1996.

[63] B.A. Schrefler, H.W. Zhang, M. Pastor, and O.C. Zienkiewicz. Strain localisation modelling and pore pressure in saturated sand samples. *Computational Mechanics*, 22:266–280, 1998.

[64] M.S.A. Siddiquee. *FEM simulations of deformation and failure of stiff geomaterials based on element test results*. Ph.D. dissertation, University of Tokyo, Tokyo, 1994.

[65] L.J. Sluys. *Wave propagation, localization and dispersion in softening solids*. Ph.D. dissertation, Delft University of Technology, Delft, 1992.

[66] A. Stankiewicz and J. Pamin. Simulation of instabilities in non-softening Drucker-Prager plasticity. *Computer Assisted Mechanics and Engineering Sciences*, 8:183–204, 2001.

[67] A. Stankiewicz and J. Pamin. A gradient-dependent modified Cam-Clay model. In H.A. Mang, F.G. Rammerstorfer, and J. Eberhardsteiner, editors, *Proc. Fifth World Congress on Computational Mechanics WCCM V*, Vienna, 2002. Published on the web: wccm.tuwien.ac.at. http://wccm.tuwien.ac.at/publications/Papers/fp80510.pdf.

[68] A. Stankiewicz and J. Pamin. Finite element analysis of fluid influence on instabilities in two-phase cam-clay plasticity model. *Computer Assisted Mechanics and Engineering Sciences*, 13(4):669–682, 2006.

[69] T. Svedberg and K. Runesson. A thermodynamically consistent theory of gradient-regularized plasticity coupled to damage. *Int. J. Plast.*, 13(6-7):669–696, 1997.

[70] R.L. Taylor. FEAP - A Finite Element Analysis Program, Version 7.4, User manual. Technical report, University of California at Berkeley, Berkeley, 2001.

[71] J. Tejchman. Influence of a characteristic length on shear zone formation in hypoplasticity with different enhancements. *Computers and Geotechnics*, 31:595–611, 2004.

[72] A. Truty. *The nonlinear soil model for the analysis of stress state and deformation in embankments subjected to seismic loads (in Polish)*. Ph.D. dissertation, Cracow University of Technology, Cracow, 1995.

[73] A. Truty. On certain class of mixed and stabilized mixed finite element formulations for single and two-phase geomaterials. Technical Report Monograph 48, Cracow University of Technology, Cracow, 2002.

[74] A. Truty. Efektywny schemat całkowania równań przyrostowych dla modelu modified Cam–Clay. In *Proc. XV Conf. Computer Methods in Design and Analysis of Hydrostructures*, Cracow, 2003. Cracow University of Technology.

[75] A. Truty. Private communication. 2004.

[76] I. Vardoulakis. Dynamic stability analysis of undrained simple shear on water-saturated granular soils. *Int. J. Num. Anal. Meth. Geomech.*, 10:177–190, 1986.

[77] I. Vardoulakis and E.C Aifantis. Gradient dependent dilatancy and its implications in shear banding and liquefaction. *Ing.-Arch.*, 59:197–208, 1989.

[78] I. Vardoulakis and E.C. Aifantis. A gradient flow theory of plasticity for granular materials. *Acta Mech.*, 87:197–217, 1991.

[79] I. Vardoulakis and J. Sulem. *Bifurcation Analysis in Geomechanics*. Blackie Academic & Professional, London, 1995.

[80] K. Willam and M. Iordache. Fundamental aspects of failure modes in brittle solids. In Z.P. Bažant et al., editors, *Fracture and Damage in Quasibrittle Structures*, pages 53–66, London, 1994. E&FN Spon.

[81] K.J. Willam and A. Dietsche. Fundamental aspects of strain-softening descriptions. In Z.P. Bažant, editor, *Fracture Mechanics of Concrete Structures*, pages 227–238, London and New York, 1992. FRAMCOS, Elsevier Applied Science.

[82] K.J. Willam and G. Etse. Failure assessment of the extended Leon model for plain concrete. In N. Bićanić et al., editors, *Proc. Second Int. Conf. Computer Aided Analysis and Design of Concrete Structures*, pages 851–870, Swansea, 1990. Pineridge Press.

[83] K.J. Willam, T. Münz, G. Etse, and Ph. Menétrey. Failure conditions and localization in concrete. In H.A. Mang et al., editors, *Proc. EURO-C 1994 Int. Conf. Computer Modelling of Concrete Structures*, pages 263–282, Swansea, 1994. Pineridge Press.

[84] B. Wrana and A. Borowiec. Saturated soil layers under dynamic load - results review. In W. Biliński and K. Piszczek, editors, *Proc. XVII Conf. Computer Methods in Design and Analysis of Hydrostructures*, pages 173–185, Cracow, 2005. Cracow University of Technology.

[85] W. Wunderlich, editor. *Proc. European Conf. on Computational Mechanics ECCM'99*, Munich, 1999. Technical University of Munich.

[86] Z-SOIL.PC 2003 - Soil, Rock and Structural Mechanics in dry or partially saturated media, User manual. Technical report, Zace Services Ltd, Software Engineering, Lausanne, Switzerland, www.zace.com, 2003.

[87] H.W. Zhang, L. Sanavia, and B.A. Schrefler. An internal length scale in dynamic strain localization of multiphase porous media. *Mech. Cohes.-frict. Mater.*, 4:443–460, 1999.

[88] H.W. Zhang and B.A. Schrefler. Gradient-dependent plasticity model and dynamic strain localisation analysis of saturated and partially saturated porous media: one dimensional model. *Eur. J. Mech. A-Solids*, 19(3):503–524, 2000.

[89] H.W. Zhang and B.A. Schrefler. Particular aspects of internal length scales in strain localisation analysis of multiphase porous materials. *Comput. Meth. Appl. Mech. Eng.*, 193:2867–2884, 2004.

[90] O.C. Zienkiewicz, A.H.C. Chan, M. Pastor, B.A. Schrefler, and T. Shiomi. *Computational Geomechanics*. John Wiley & Sons, Chichester, 2000.

[91] M. Życzkowski. Discontinuous bifurcations in the case of the Burzyński-Torre yield condition. *Acta Mech.*, 132:19–35, 1999.

Numerical analysis of strain localization

in one- and two-phase geomaterials

Summary

In the thesis the problem of instability as well as strain and pore pressure localization in granular materials is approached. In the analysis the modified Cam-clay plasticity model is used in its local (without an internal length parameter) and enhanced version (with a gradient term) for a one-phase medium (including the limiting cases of drained and undrained conditions) and a two-phase medium. The plastic model is combined with nonlinear elasticity. The gradient-enhancement of the model is proposed in order to avoid the spurious discretization sensitivity of finite element solutions. The classical and gradient-dependent versions of the theory for one- and two-phase soil and their numerical implementation are summarized. Calculations are performed using the development version of the FEAP finite element package. The numerical material model and the algorithms are incorporated into the FEAP in the following steps:

- local version of Cam-clay model for one-phase medium
- two-field finite element with discretization of displacements and excess pore pressure (local Cam-clay model for two-phase medium)
- two-field finite element with discretization of displacements and plastic multiplier (gradient-enhanced Cam-clay model for one-phase medium)
- three-field finite element with discretization of displacements, excess pore pressure and plastic multiplier (gradient-dependent Cam-clay model for two-phase medium)

Basic one-element tests and a typical shear banding benchmark of biaxially compressed soil specimen are discussed. In the analysis the attention is focused on the influence of fluid phase on soil instabilities.

Numeryczna analiza zjawisk lokalizacji odkształceń
w jednofazowym i dwufazowym ośrodku geotechnicznym

Streszczenie

W pracy został przeanalizowany problem niestateczności i lokalizacji odkształceń oraz ciśnień porowych w materiałach ziarnistych. Do analizy w zakresie plastycznym użyto modelu Cam-clay w wersji lokalnej (bez wewnętrznej skali długości) oraz zregularyzowanej (człon gradientowy) dla ośrodka jednofazowego (stan zatrzymanego i swobodnego drenażu) i dwufazowego. Uwzględniono nieliniowe zachowanie materiału w zakresie sprężystym. Gradientową wersję modelu zaproponowano dla uniknięcia pasożytniczej zależności rozwiązań uzyskanych metodą elementów skończonych od dyskretyzacji. Przedstawiono opis klasycznej i gradientowej wersji teorii dla ośrodka jedno- i dwufazowego oraz ich numeryczną implementację. Obliczenia prowadzono w rozwijanej wersji pakietu FEAP po wcześniejszym zaimplementowaniu własnych procedur. Oprogramowany został model materiału Cam-clay oraz trzy elementy skończone. Były to: element dwupolowy z aproksymacją pola przemieszczeń i (nadwyżki) ciśnień porowych (lokalny model Cam-clay dla ośrodka dwufazowego), element dwupolowy z aproksymacją pól przemieszczeń i mnożnika plastycznego (zregularyzowany model Cam-clay dla ośrodka jednofazowego) i ostatecznie element trójpolowy z dyskretyzacja wszystkich trzech wymienionych wcześniej pól (gradientowy model Cam-clay dla ośrodka dwufazowego). Przedyskutowano wyniki podstawowych testów jednoelementowych oraz typowego zagadnienia powstawania pasm ścinania w dwuosiowo ściskanej próbce gruntu. W obliczeniach szczególną uwagę zwrócono na wpływ fazy ciekłej na rozwiązania zagadnień niestateczności materiału.